DESIGN AND APPLICATION OF PEPTIDE NANOFIBERS FOR MODULATING ANGIOGENESIS

A DISSERTATION SUBMITTED TO

THE GRADUATE SCHOOL OF ENGINEERING AND SCIENCE

OF BILKENT UNIVERSITY

IN PARTIAL FULFILLMENT OF THE REQUIREMENTS FOR

THE DEGREE OF

DOCTOR OF PHILOSOPHY

IN

MATERIALS SCIENCE AND NANOTECHNOLOGY

By

BERNA ŞENTÜRK

June 2016

DESIGN AND APPLICATION OF PEPTIDE NANOFIBERS FOR MODULATING ANGIOGENESIS

By Berna Şentürk

June 2016

We certify that we have read this dissertation and that in our opinion it is fully adequate, in scope and in quality, as a thesis for the degree of Doctor of Philosophy.

Ayşe Begüm Tekinay (Advisor)

Mustafa Özgür Güler (Co-Advisor)

Bahri Aydın

Aykutlu Dana

Çağlar Elbüken

Çağdaş Son

Approved for the Graduate School of Engineering and Science:

Levent Onural
Director of the Graduate School

ABSTRACT

DESIGN AND APPLICATION OF PEPTIDE NANOFIBERS FOR MODULATING ANGIOGENESIS

Berna Şentürk

PhD in Materials Science and Nanotechnology

Supervisor: Ayşe Begüm Tekinay

Co-Supervisor: Mustafa Özgür Güler

June 2016

Angiogenesis is important in many diseases, such as diabetic wound healing, cancer and corneal neovascularization. Angiogenesis can be induced or inhibited by complex biological systems. Mimicking the complexity in natural systems requires smart supramolecular architectures with predictable properties and functions.

Peptides are particularly attractive as molecular building blocks in the bottom-up fabrication of supramolecular structures based on self-assembly and have potential in many important applications in the fields of tissue engineering and regenerative medicine. Peptide-based biomaterials for angiogenesis are currently an intensely investigated topic in pathology and pharmacology related studies. Peptide-based biomaterials can be utilized for the treatment of angiogenesis-deficient complications by mimicking natural glycosaminoglycans. Diabetic ulcerations are largely caused by the lack of vascularization during the wound healing process, and angiogenesis-promoting peptide nanofibers are highly promising for the treatment of these injuries.

In addition to the induction of angiogenesis, peptide-based systems can also be used to prevent it in locations where it is detrimental to health. In particular, peptide amphiphiles with anti-angiogenic properties may enable the treatment severe eye diseases, including corneal neovascularization.

This thesis describes nature-inspired combinatorial methods for designing peptide nanostructures that display angiogenic and anti-angiogenic functional moieties. The importance of multivalent peptide-constructs for high affinity binding and efficiency will be highlighted. Furthermore, in vitro and in vivo efficiency of angiogenesis related therapeutic agents is reported. Another type of products that will be discussed is black silicon surface that inspired also from nature, utilized for anti-bacterial and unique topographical characteristic.

Keywords: Peptide Nanofibers, Functional Self-Assembly, Biomaterials, Angiogenesis, Diabetic Wound Healing, Corneal Neovascularization

ÖZET

ANJİYOGENEZ MODÜLASYONU İÇİN PEPTİT NANOFİBERLERİN TASARIMI VE UYGULANMASI

Berna Şentürk

Malzeme Bilimi ve Nanoteknoloji, Doktora

Tez Danışmanı: Ayşe Begüm Tekinay

Eş Danışman: Mustafa Özgür Güler

Haziran 2016

Anjiyogenez birçok hastalıkta önem taşımaktadır, bunlardan bazıları diyabetik yara iyileşmesi, kanser ve kornea neovaskularizasyonudur. Anjiyogenez karmaşık biyolojik sistemler tarafından uyarılabilir veya baskılanabilirler. Doğal sistemlerin karmaşıklığını taklit etmek, öngörülebilir özellikleri ve fonksiyonları olan akıllı çok moleküllü mimariler gerektirir.

Peptitler özellikle moleküler yapı taşları olarak yer aldıkları çok moleküllü kendiliğinden kuruluma dayalı aşağıdan yukarıya üretimde çekicidirler ve doku mühendisliği ve yenileyici tıp gibi birçok önemli alanda uygulama potansiyeline sahiptirler. Anjiyogenezde peptit-bazlı biyomalzemeler patoloji ve farmakoloji ile ilgili çalışmalarda günümüzde yoğun olarak araştırılan bir konudur. Pepetit-bazlı biyomalzemelerden anjiogenezin eksik olduğu komplikasyonların tedavisinde doğal glikosaminoglikanları taklit ederek yaralanılabilinir. Diyabetik yaralara, yara iyileşmesi sırasında damarlanmanın eksikliği sebep olmaktadır ve anjiyogenezi uyaran peptit nanofiberler bu yaraların tedavisinde umut vaat etmektedir.

Anjiyogenezin uyarılmasına ek olarak, peptite dayanan sistemler anjiyogenezin sağlığa zararlı olduğu yerlerde baskılanmasında kullanılabilir. Bilhassa, anti-anjiyogenez özellikli peptit amfifiller ciddi göz hastalıklarından kornea damarlanmasının iyileştirilmesini mümkün kılar.

Bu tez anjiyogenik ve anti-anjiyogenik özellikte pay sergileyen peptit nanoyapı tasarımının doğadan esinlenilmiş birleşimsel metotlarını tanımlar. Yüksek bağlanma çekimi için peptit kurgusunun çoklu yönünün önemi ve etkisinin altı çizilmektedir. Ayrıca, *in vitro* ve *in vivo* deneylerdeki anjiyogenezle ilgili tedavi edici ajanların etkisi rapor edilmiştir. Diğer bir tartışılan ürün ise yine doğadan esinlenilen, anti-bakteriyel ve benzersiz topografik karakteri olan siyah silikon yüzeydir.

Anahtar kelimeler: Peptit Nanofiberler, İşlevsel Süpramoleküler Nanoyapılar, Biyomalzemeler, Anjiyogenez, Diyabetik Yara İyileşmesi, Kornea Damarlanması

Acknowledgements

I would like to express my gratitude to my advisors, Prof. Tekinay and Prof. Güler for their guidance and support to my research. Their encouragement helped me develop a trans-disciplinary understanding, which I can carry with me throughout my research career.

I would like to acknowledge the PhD scholarship and funding from TÜBİTAK (The Scientific and Research Council of Turkey) BIDEB 2211-C, 111S495, 11M710, 214Z214 and 114S912. I would also like to thank for international conference supports of TÜBİTAK (in the form of 2224-A).

I would like to express my most sincere thanks to Elif Arslan, Dr. Gülcihan Gülseren and Gülistan Tansık for their companionship in this long marathon. Their support has always kept me motivated. Their friendship deserves all compliments. I would like to express my special thanks to Ruslan Garifullin, Dr. Adem Yıldırım, Burak Demircan, Alper Devrim Özkan, Öncay Yaşa for their fruitful collaboration. I would also like to thank all NBT and BML group members and especially Öncay Yaşa, Ceren Garipoğlu, Didem Mumcuoğlu, Yasin Tümtaş, Hakan Ceylan, Nuray Gündüz, Dr. Büşra Mammadov, Dr. Rashad Mammadov, Meryem Hatip, M. Aref Khalily, Dr. Seher Üstün Yaylacı, Melike Sever, Gökhan Günay, Egemen Deniz Eren, Seren Hamsici, Zeynep Orhan, İslam Oğuz Tuncay, Merve Şen, Çağla Eren, İdil Uyan, İbrahim Çelik, Canelif Yılmaz, Melis Şardan, Göksu Çınar for creating such a warm working environment. My special thanks to Zeynep Erdoğan and Mustafa Güler for their immense technical help.

Bilkent University has been my home with all the unforgettable memories for the past ten years, including my undergraduate education. Prof. Doğramacı's endless pursuit of reaching perfection opened wide avenues in my endeavors. Finally, I would like to express my most sincere gratitude

to my family especially my sister Berrrin Şentürk who always encourage me. We work together for day and night for 5 years.

Contents

List of Figures

List of Tables

Abbreviations

BSA	: Bovine serum albumin
CD	: Circular dichroism
Col-I	: Collagen type I
Col-III	: Collagen type III
DCM	: Dichloromethane
DMF	: N, N-Dimethylformamide
DMEM	: Dulbecco’s modified Eagle’s medium
ECM	: The extracellular matrix
EDTA	: Ethylenediaminetetraacetic acid
FBS	: Fetal bovine serum
FDA	: U.S. Food and Drug Administration
GAG	: Glycosaminoglycan
HUVEC	: Human umbilical vein endothelial cell
HPLC	: High performance liquid chromatography
LC-MS	: Liquid chromatography-mass spectrometry
IHC	: Immunohistochemistry

PA : Peptide amphiphiles

PBS : Phosphate-buffered saline

Q-TOF : Quadrupole time of flight

SDS : Sodium dodecyl sulfate

SEM (M) : Scanning electron microscope

SEM (S) : Standard error of the mean

STEM : Scanning transmission electron microscope

TIS : Triisopropylsilane

TCP : Tissue culture plate

TEM : Transmission electron microscope

TFA : Trifluoroacetic acid

WHO : World Health Organization

Chapter 1

Introduction: Inducing Angiogenesis with Biomaterial-Based Systems

Angiogenesis is the formation of new blood vessels from pre-existing networks, orchestrated by a complex biological signaling system composed of various factors. These factors include vascular endothelial growth factor (VEGF), transforming growth factor β (TGF-β), and fibroblast growth factor (FGF). Angiogenesis is tightly regulated through the activation of endothelial cells, local degradation of the extracellular matrix and vascular basement membranes, and stabilization of newly formed vessels through the proliferation and migration of the native cell population.

Angiogenesis occurs in 4 stages; (1) stimulation of endothelial cells by angiogenic factors, (2) degradation of the capillary basal lamina by activated endothelial cells, (3) capillary sprout formation and (4) migration of endothelial cells and vessel maturation. In the early steps of angiogenesis, vasodilatation occurs through the induction of transcription of VEGF by endothelial cells. Vascular permeability factor (VPF) can increase vessel permeability and induce vascular leakage, allowing plasma proteins (such as fibrin/fibrinogen, and plasma-clotting proteins) to extravasate and form a fibrin gel that serves as a temporary matrix for endothelial cell migration. To prevent the excessive loss of plasma proteins, the organism has to provide mechanisms to regulate vascular permeability. Angiopoietin-1 (Ang1), a ligand for the endothelial receptor Tie-2, protects existing vessels from leakage. Ang1 and VEGF work together during vascular development.

The second stage is a prerequisite for the migration of endothelial cells and involves the degradation of ECM components and basement membranes through proteolytic enzymes,

principal among which are matrix metalloproteinases (MMPs). MMP2 (gelatinase A) and MMP9 (gelatinase B) are especially important for the degradation of collagen in the vascular basement membrane. The proteolytic activity of MMPs is controlled and can be inhibited by tissue inhibitors of metalloproteinases (TIMPs). Moreover, MMPs have important roles in degrading ECM components and are also involved in different pro- and anti-angiogenic processes.

After the degradation of the basal lamina, endothelial cells proliferate and migrate to the chemotactic stimuli resulting from this process. Several factors, such as VEGF, basic fibroblast growth factor (bFGF), angiopoietins, and chemokines (including monocyte chemotactic protein-1 (MCP-1)) are involved in this process. Endothelial cells that migrate to the ECM subsequently assemble as tubular structures. Furthermore, endothelial cells can fuse with other existing vessels to form new ones and develop numerous cell-cell junctions.

At the final stage of vessel maturation, a vascular basement membrane is deposited and periendothelial cells are recruited to stabilize the vessels by inhibiting endothelial cell proliferation and migration. The main role of pericytes is to provide intact pericyte-endothelial associations in order to prevent vessel regression and aberrant remodeling. In addition to that, pericytes inhibit the further proliferation of endothelial cells and stabilize the new vessels.

Angiogenesis is controlled by a number of growth factors and inhibitors. Well-known angiogenic (stimulatory) growth factors include chemokines, fibroblast growth factor (FGF), hepatocyte growth factor (HGF), hypoxia-inducible factor (HIF), platelet growth factor (PDGF) and vascular endothelial growth factor (VEGF). Angiogenic inhibitors include angiopoietin, angiostatin, chemokines, endostatin, interferon, pigment epithelium-derived factor (PEDF) and thrombospondin. Increases in pro-angiogenic factors promote angiogenesis, while increases in

anti-angiogenic factors lead to the inhibition of angiogenesis. When this balance is disturbed, the result is either too much or too little angiogenesis. This effect may result in abnormal blood vessel growth and insufficient vessel formation, and both phenomena are associated with many diseases.

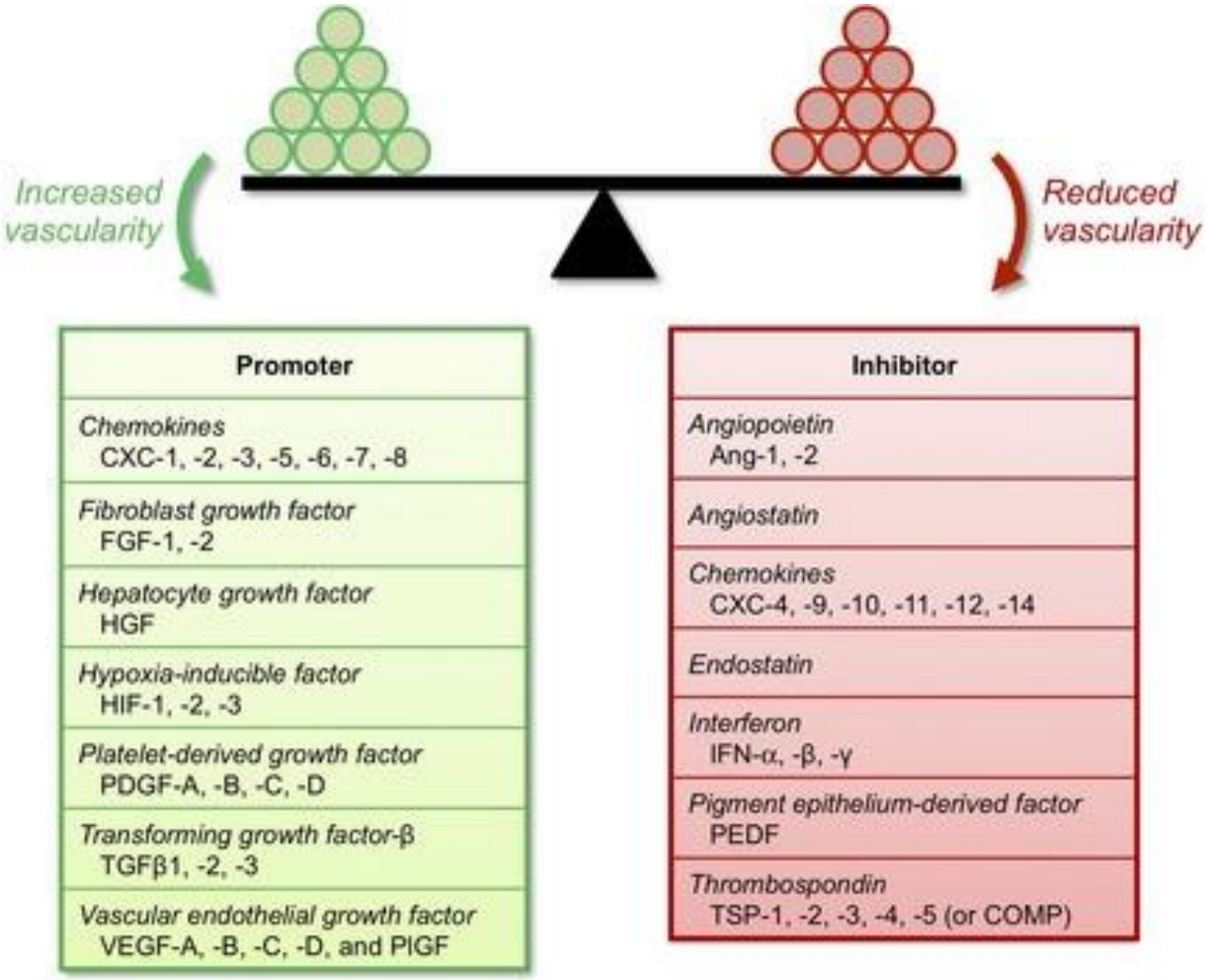

Figure 1.1 Angiogenesis is regulated through balancing pro-angiogenic factors and anti-angiogenic factors. Increase in pro-angiogenic factors stimulates angiogenesis, while increase in anti-angiogenic factors leads to inhibition of angiogenesis (Reproduced from Ref. 1 with permission from Journal of Cellular and Molecular Medicine [1]).

Diseases Related to Angiogenesis

Angiogenesis is the physiological process of growing new blood vessels from preexisting vessels, and its malfunction has been implicated in a wide range of diseases. The loss of control of angiogenesis can lead to insufficient angiogenesis or excessive angiogenesis. Most common diseases related to insufficient angiogenesis are Alzheimer's disease, diabetes, atherosclerosis, coronary artery disease, diabetic ulcers and chronic wounds.

The role of angiogenesis in neurodegenerative disorders is still unknown, but vascular insufficiency may play a strong role in the pathology of degenerative disease such as Alzheimer's disease. More than 30% of patients with Alzheimer's disease have microvascular lesions together with the focal swelling, atrophy and necrotic degeneration of blood vessels. Vascular dysfunction might also affect pericytes and smooth muscle cells found in β-amyloids, which are well-recognized as a main cause of Alzheimer's disease. Increased VEGF expression related to immune reactivity is found in reactive astrocytes and intraparenchymal vessels of patients with Alzheimer's disease. VEGF also has a possible role in stroke, as its expression is upregulated in the brain during this event. Studies on animal experiments showed that VEGF levels markedly increase on ischemic neurons. In addition to VEGF expression, receptors such as VEGFR-1 and VEGFR-2 are also vital factors in the pathophysiology of stroke [2].

Angiogenesis may play a central role in the development of atherosclerosis through the destabilization of plaques. The formation of plaques leads to ruptures, which may progress to cause intra-arterial occlusion. In coronary arteries, the sudden restriction of the blood supply to the heart causes an acute coronary syndrome, potentially resulting in a loss of cardiac function and death. Angiogenic factors such as growth factors and cytokines can promote atherosclerosis

in some animal models and facilitate the destabilization of coronary plaques by promoting intralesion angiogenesis [3]. Therefore, angiogenesis represents an excellent therapeutic target for the treatment of atherosclerosis and cardiovascular disease. Some efforts have been made to treat atherosclerosis through the use of angiogenic growth factors, VEGF and FGF-2, to promote neovascularization in animal models of ischemic cardiovascular disease. However, clinical studies remain inconclusive and some authorities suggest that the reckless usage of angiogenic growth factors might itself cause the destabilization of coronary plaques and intralesion angiogenesis [4]. Pro-angiogenic therapy for ischemic heart disease might be more appropriate, but detailed clinical studies are required to support it.

Angiogenesis is required for healthy wound repair, since newly formed blood vessels are critical for the formation of granulation tissue and provide nutrition and oxygen to growing tissues. Induction of angiogenesis in response to tissue injury is a dynamic process that is highly regulated by certain cells (i.e. macrophage, monocytes), cytokines and extracellular matrix (ECM) components. Vascular endothelial growth factor, angiopoietin, fibroblast growth factor, and transforming growth factor beta have critical roles in wound angiogenesis. Due to a complex network of numerous mediators controlling angiogenesis, a high functional redundancy is assumed in this process.

The development of modern biotechnology has allowed the potential use of growth factors to elicit angiogenesis in a therapeutic context. Two main strategies, usage of recombinant growth factor proteins and gene therapy, are widely studied on animals and pre-clinical models. So far only recombinant human PDGF-BB is approved for the therapy of non-healing diabetic foot ulcers (Regranex®). Additionally, some studies showed possible side effects of angiogenesis therapy and emphasized the urgent need for further research to better understand specific

functions of angiogenic mediators and the means to develop these mediators in order to eliminate their side effects.

Imbalance of Angiogenesis in Diabetic Complications

Diabetes is associated with many complications, including impaired wound healing, neuropathy, peripheral vascular disease, coronary heart disease, retinopathy and nephropathy. It is well documented that complications of diabetes are not only related to hyperglycemia but also caused by abnormalities of angiogenesis. Vascular abnormalities in different tissues, including retina and kidney, can play a role in the pathogenesis of micro-vascular complications of diabetes; while vascular impairment also contributes to macrovascular complications such as diabetic neuropathy and impaired formation of coronary collaterals.

One of the main reasons of late diagnosis of foot ulcers is diabetic neuropathy. The impairment of peripheral nervous system causes a loss of sensation and decreased awareness of injuries in extremities and especially the feet. Pathology of diabetic neuropathy includes decreased angiogenic and neurotrophic growth factors, increased production of ROS elements and impaired blood circulation [5]. The prevalence of diabetic neuropathy is 7% within 1 year of diagnosis and 50% for patients at 25 years after diabetic diagnosis [2].

Angiogenesis plays crucial roles in the pathophysiology of diabetic retinopathy, which can eventually cause vision loss [5]. Complications resulting from vitreous hemorrhage and abnormal vessel growth on the optic disk or retina may cause diabetic retinopathy [6]. Almost half of the people with diabetic retinopathy are under risk of developing diabetic macular edemas, which are characterized by the swelling of macular area and retinal thickening [7].

Hyperglycemia-induced glycosylated hemoglobin is a principal factor behind the impairment of renal function in diabetes. Nephropathy is accepted as the most common end stage of renal diseases in both type 1 and type 2 diabetic patients. The initial evidence of the relationship between abnormal angiogenesis and diabetic nephropathy was the formation of blood vessels in the glomeruli of diabetic patients, which was first reported in 1987 [8]. Abnormal vessels are also found in the Bowman's capsule and the glomerular vascular pole. During early steps of nephropathy, the secretion of angiogenic growth factors such as VEGF and PDGF are increased, resulting in the degeneration of kidneys [9].

A diabetic patient might develop chronic non-healing wounds in response to otherwise minor injuries. Deficiencies in growth factor expression, non-functional ECM and insufficient inflammatory responses are main factors responsible for chronic wounds in diabetic patients. In addition to those functional abnormalities, secondary complications of diabetes also contribute to the uncoordinated healing response at the cellular and molecular levels. As mentioned above, vascular disease is enhanced in patients with diabetes, and diabetic blood vessels suffer from physical and functional abnormalities including reductions in capillary sizes, thickening of basement membranes, and hyalinosis of arterioles.

Biomaterial-Based Therapeutics

A decade of clinical testing, utilizing both protein and peptide-based therapies designed to stimulate or inhibit angiogenesis, has resulted in the clinical approval of only a few therapeutic agents. Animal studies with biomaterial-based systems offer a great promise for the transition of angiogenesis therapy from animals to humans and might be a new platform for the treatment of diseases that are typically regarded as unamenable to treatment.

The development of peptide-base drugs and therapeutic reagents has progressed considerably with advanced synthesis methods. The discovery of solid-phase peptide synthesis has facilitated the development of synthetic peptides for a wide range of applications, including biotechnology and medicine. Peptide amphiphiles can be used to develop materials with advanced multi-functional properties through simple chemical modifications. Two main types of synthesis methods are available: the solid-phase peptide synthesis method supports chemical synthesis on a solid mesh and eliminates the necessity of elaborate purification steps, while liquid-phase peptide synthesis is suitable for large scale synthesis efforts.

Solid-phase peptide synthesis is based on the sequential addition of protected amino acids onto an insoluble support such as resin. The addition of amino acids proceeds from the carboxy-terminus to the amino-terminus, and the first amino acid is attached to a solid support by a linker. Protecting groups are bound to the side-chains of amino acids to prevent them from reacting throughout chain assembly. During each coupling step, amino acids are protected and deprotected until the amino acid chain is complete. At the final step, the peptide is cleaved from the solid support and lyophilized. The peptide can be evaluated by reverse-phase high-performance liquid chromatography and mass spectrometry, and its purification can be performed with certain tools [10].

10 to 20 amino acid long peptides are optimal as antigens, while short peptides of less than approximately 7 residues are probably insufficient to function as epitopes. Larger peptides may be problematic since they adopt their own specific conformation and are difficult to be uptake by cells. The chemical difficulties of synthesizing certain amino acid sequences can complicate the synthesis. In general, hydrophilic sequences are more soluble and easier to synthesize. The synthesis of peptides can be performed manually, but such an approach is labor-intensive and

requires significant knowledge of peptide chemistry. They can be also purchased from companies, but doing so increases their costs. A labor intensive peptide synthesis is more favorable than custom synthesis, because it allows much greater flexibility in the design, modification and production of peptides.

Peptides have several advantages over antibodies in terms of their size, cost, solubility and ease of modification and manufacturing [11]. Peptides have been tested in the treatment of angiogenesis-related diseases due to their biocompatibility and high specificity. Angiogenesis is a dynamic process that includes multiple targets at each step. Proliferation, migration, tube formation, homing of endothelial progenitor cells and vessel maturation are controlled by several regulators. Peptide-based strategies can be developed to target those regulators and used for the induction and inhibition of angiogenesis.

Many new angiogenic modulators have been developed in the past few years, especially targeting two molecular systems, integrin and VEGF (or its receptors). PR39, a proline-rich, 39 amino acid-long peptide, was found to induce angiogenesis by upregulating the expression of HIF-1α protein. PR39 (RRRPRPPYLPRPRPPPFFPPRLPPRIPPGFPPRFPPRFP) achieved this effect by protecting HIF-1α from ubiquitin–mediated degradation in proteasomes [12]. Another peptide-based angiogenic stimulator sequence; SVVYGLR, is actually an osteopontin-derived peptide that exhibits angiogenic activity [13]. Many ligands involved in cell adhesion contain the arginine-glycine-aspartic acid (RGD) sequence, which functions as a primary recognition site between ligands and receptors. The first therapeutic application of RGD was for the delivery of doxorubicin to endothelial cells. This drug is efficient for the inhibition of tumour growth and metastases in mice [14].

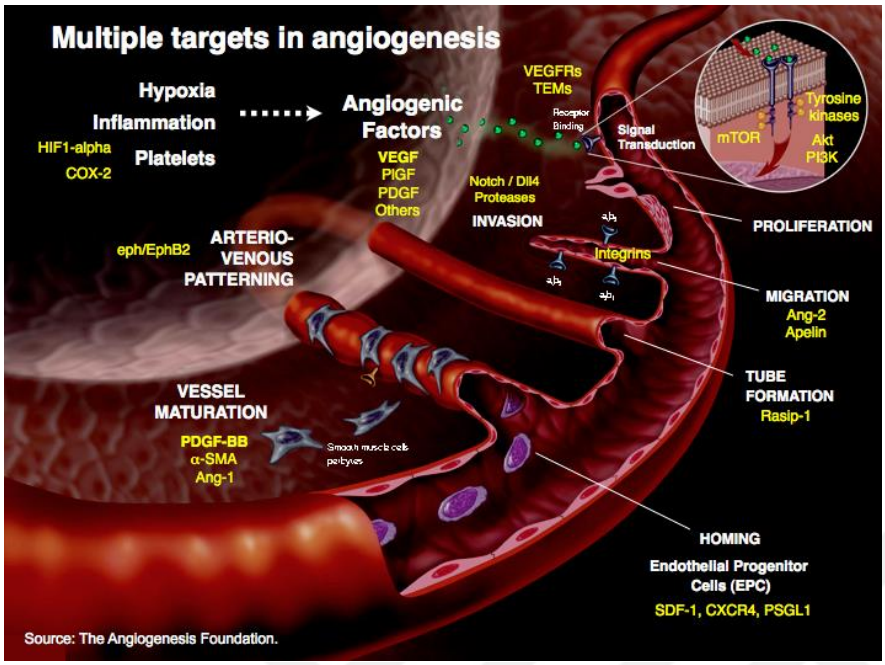

Figure 1.2 Schematic representation of steps and possible targets of angiogenesis.

Anti-angiogenic Peptides

Chemically synthesized anti-angiogenic peptides typically inhibit angiogenesis by blocking angiogenic factors or their receptors. Identification of those peptides are performed with a myriad of approaches, including isolation and identification of endogenous inhibitors, antibody therapies against pro-angiogenic molecules and their receptors, anti-sense approaches using growth factor receptors as antagonists, and interference-based methods incorporating growth factor signaling pathways into peptide design. Computational screening through docking is also a viable method of peptide discovery. Chemical synthesis of amino acids has seen great advances and improved pharmacokinetic parameters have contributed to the relative ease of transition for those products from discovery to the clinic. Anti-angiogenic therapeutic peptides can be classified as peptides derived from the extracellular matrix, growth factors and receptors, coagulation cascades, chemokines, and anti-angiogenic proteins (i.e. thrombospontin).

Extracellular matrix components are important for all steps of angiogenesis, and especially for cell proliferation and migration. The cilengitide peptide sequence (c-[Arg-Gly-Asp-DPhe-(NMeVal)]) is derived from a well-studied integrin-binding RGD, which targets the laminin-binding integrins $\alpha_v\beta_3$ and $\alpha_V\beta_5$, and has been used for cancer treatment [15]. Similarly, ATN-161 (Ac-PHSCN-NH2) peptide inhibits microvascular density and neovascularization via integrin mediated signaling [16]. Another ECM-derived anti-angiogenic peptide, tumstatin (TLPFAYCNIHQV CHYAQRNDRSYWL), is modified from the non-collagenous domain of type IV collagen; and effective in the treatment of Lewis lung carcinoma via inhibiting tumor growth, cell proliferation and migration of endothelial cells [17]. Additionally, a shorter fragment of the tumstatin sequence, YSNSG, exhibits anti-angiogenic activity by reducing the adhesion and migration of endothelial and carcinoma cells [18].

Vascular endothelial growth factor (VEGF) is one of the most important modulators of angiogenesis. The sequences of ATWLPPR and CPQPRPLC peptides were first identified by a phage display screening approach for a sequence targeting the VEGF receptor neuropilin-1 [19, 20]. The effects of the ATWLPPR sequence were initially tested on the proliferation of vascular endothelial cells, and 2.1 x 10^{-4} M of synthetic peptide treatment was shown to result in 60% of inhibition of cell proliferation after 24 h. The importance of the C-terminal arginine was determined by deletion of each amino acid, and the subsequent quantification of inhibitory effect of each substitute on the binding of $VEGF_{165}$ to NRP-1. The inhibitory effect of peptides was quantified by radioactive measurement of [$_{125}$I]-$VEGF_{165}$. The substitution of positively charged arginine and lysine residues resulted in an important loss of activity. Deletion of arginine and replacement with alanine (ATWLPPA) results in 17% inhibition efficiency compared to the unaltered peptide, demonstrating the critical role of the arginine amino acid. In contrast, the

LPPR peptide sequence is responsible for 75 ±7.9% $VEGF_{165}$ inhibition compared to the intact peptide sequence. The anti-angiogenic activity of peptide was further demonstrated through its ability to inhibit the tube formation of HUVECs *in vitro*. *In vivo* studies of the ATWLPPR peptide also support *in vitro* results and suggest that the peptide sequence is able to markedly inhibit corneal angiogenesis in the rabbit model [21]. The LPPR sequence is identified as the shortest sequence required for anti-angiogenic activity. Moreover, the retro-inverted $_D$(LPR) sequence was designed and tested in the mouse mammary cancer model to investigate its efficiency [22], and the D-form of the LPR sequence was found to more stable than L-form due to its resistance to enzymatic degradation, while exhibiting anti-angiogenic activity comparable to the L-peptide. Fibroblast growth factor (FGF)-2 is as important as VEGF for anti-angiogenic therapies. The Ac-ARPCA sequence is derived from long-pentraxin-3, the antagonist of FGF-2, and was found to be capable of inhibiting the proliferation and adhesion of endothelial cells, facilitating the ceasement of angiogenesis in a chick embryo chorioallantoic membrane assay (CAM) [23]. The P144 peptide (TSLDASIIWAMMQN), derived from TGF-β type III receptor, has a high binding affinity for TGF-β and this binding inhibits the pro-angiogenic activity of this growth factor [24].

Peptides derived from proteins involved in the coagulation cascade represent another strategy for the treatment of angiogenesis. Histidine-proline-rich glycoprotein (HPRG) acts as an inhibitor of angiogenesis for pancreatic carcinoma. This peptide is able to target focal adhesion points in endothelial cells and prevent angiogenesis by interfering with cytoskeletal reorganization. The angiotensin derived A-779 peptide (ARCTIH-DA) is able to inhibit endothelial cell tube formation and results in microvascular density reduction in treated lung xenografts. The KV11 peptide (YTMNPRKLFDY) is inspired from kringles protein domains, which are important in

the blood coagulation cascade. It has been shown that KV11 inhibits angiogenesis by disturbing cell migration and tube formation. Moreover, the fibrinogen-derived ARPAKAAATQK KVERKAPDA sequence inhibits the adhesion of endothelial cells to collagen IV and disrupts vessel formation [25].

Platelet growth factor 4 (PF4) belongs to CXC chemokine family and plays an important role in blood coagulation and angiogenesis. The NGRKISLDLRAPLYKKIIKKLLES peptide sequence is derived from PF4 and targets VEGF and FGF-2, which are pro-angiogenic growth factors. Its treatment leads to the inhibition of angiogenesis and tumor growth in carcinoma and orthotopic glioma models [26]. Anginex, a β–sheet forming peptide (β pep-25), inhibits angiogenesis by blocking the proliferation of endothelial cells and inducing apoptosis. It is suggested as a potential anti-angiogenic agent for therapeutic use against various pathological disorders, such as diabetic retinopathy [27]. Thrombospondin (TSP) family contains multifunctional proteins that have important roles in angiogenesis. TSP-1 has direct and indirect effects on inhibition of angiogenesis: It is able to directly inhibit endothelial cell function by blocking migration and survival and indirectly disturbs growth factor mobilization. Other inhibitory peptides include CD36 binding sequences such as properdistatin **(**GPWEPCSVTCSKGTRTRRR). Four known TSP1-derived peptide sequences are under pre-clinical trial and tested for their potential anti-angiogenic effects on cancer [25].

Serpins (serine proteinase inhibitors) are the largest superfamily of protease inhibitors and also play a role in the inhibition of angiogenesis. Several serpins (kallistatin, protein C inhibitor, angiotensinogen, maspin, antithrombin, nexin-1, pigment epithelial-derived factor) exhibit anti-angiogenic activity by inhibiting endothelial cell proliferation and migration. Kallistatin (SerpinA4) inhibited VEGF and bFGF induced endothelial cell proliferation, migration, adhesion

and microvessel formation in the Matrigel implants in mice [28]. Abnormal angiogenesis in rat corneas could be blocked using Protein C inhibitor (PCI), another member of serpins (SerpinA5). Peptide amphiphiles mimicking the structure of maspin (SerpinB5), another member of serpin family, also show anti-angiogenicactivity by disturbing endothelial cell motility and inhibiting angiogenesis in the embryonic chicken chorioallantois [29].

The most promising anti-angiogenic peptides are those that act directly on endothelial cells. This approach is also important for the inhibition of tumor angiogenesis, and can be used in the treatment of drug-resistant tumors. The compositional and structural similarity between these anti-angiogenic peptides may be used, possibly via combinatorial approaches, to design additional therapeutic anti-angiogenic agents. Although numerous proteins are known to be anti-angiogenic, most of them are found to be unsuitable for clinical use in human studies. As such, while anti-angiogenic peptides have various advantages over proteins and antibodies, they must also be designed with a comprehensive knowledge of angiogenic pathways to exhibit optimal activity and reflect the efficiency found in their natural counterparts.

Chapter 2

Angiogenic peptide nanofibers improve wound healing in STZ-induced diabetic rats

This work is partially described in the following publication:

Berna Senturk, Sercan Mercan, Tuncay Delibasi, Mustafa O.Guler, and Ayse B. Tekinay, Angiogenic Peptide Nanofibers Improve Wound Healing in STZ-Induced Diabetic Rats, ACS Biomaterials Science and Engineering.

2.1. Objective

Low expressions of angiogenic growth factors delay the healing of diabetic wounds by interfering with the process of blood vessel formation. Heparin mimetic peptide nanofibers can bind to and enhance the production and activity of major angiogenic growth factors, including VEGF. In this study, we hypothesized that heparin mimetic peptide nanofibers can serve as angiogenic scaffolds that allow the slow release of growth factors and protect them from degradation, providing a new therapeutic way to accelerate the healing of diabetic wounds. To test this hypothesis, we treated wounds in STZ-induced diabetic rats with heparin mimetic peptide nanofibers and studied the repair of full-thickness diabetic skin wounds. Wound recovery was quantified by analyses of re-epithelialization, granulation tissue formation and blood vessel density, as well as VEGF and inflammatory response measurements. Wound closure and granulation tissue formation were found to be significantly accelerated in heparin mimetic gel treated groups. In addition, blood vessel counts and the expressions of alpha smooth muscle actin and VEGF were significantly higher in bioactive gel treated animals. These results strongly

suggest that angiogenic heparin mimetic nanofiber therapy may be used to support the impaired healing process in diabetic wounds.

2.2. Introduction

2.2.1. Diabetes Mellitus

Diabetes mellitus is a disease that causes high glucose levels in the blood due to defects in insulin secretion or function. The World Health Organization (WHO) classifies diabetes into two main types; insulin dependent or non-insulin dependent. Type 1 diabetes, also known as insulin-dependent diabetes, is a chronic condition in which insulin is not sufficiently produced, mostly due to destruction of beta–cells in pancreatic islets. It can occur at any age. Type 2 diabetes mellitus is characterized by hyperglycemia resulting from insulin resistance and partially from the lack of insulin secretion [1]. The prevalence and incidence of type 1 diabetes is higher in children and adolescents. Type 2 diabetes is more frequently seen in adults compared to children and has become the most common health problem in the world [2].

The long–term effects of diabetes mellitus include cardiovascular disease, nerve damage (neuropathy), kidney damage (nephropathy), retinopathy and amputation [30]. Severe damage caused by those long term effects might cause heart and kidney failure, blindness and even death. In addition, patients with diabetes mellitus are more likely to die after an acute myocardial infarction than patients without diabetes [31].

Wound healing is a complex and dynamic process that can be classified under four distinct but overlapping phases: hemostasis, inflammation, proliferation and tissue remodeling. The first phase of wound healing occurs immediately after wounding and coagulation is formed by a fibrin clot. Formation of the fibrin clot is achieved through the action of fibrin, which is derived

from fibrinogen by fibronectin, vitronectin, and thrombospondin. The fibrin clot contains platelet cells, which lead to the release of pro-inflammatory cytokines and growth factors such as transforming growth factor-beta (TGF-β), platelet-derived growth factor (PDGF), fibroblast growth factor (FGF), and epidermal growth factor (EGF).

During the inflammation phase; neutrophils, monocytes and macrophages clear the wound area from contamination by bacteria and other debridements. Macrophages play a critical role in the early wound since they recruit and activate leukocytes to the wound site. Macrophages are also responsible for the clearance of apoptotic cells, including neutrophils, to facilitate the subsequent proliferation of keratinocytes, fibroblasts and endothelial cells. Functions of neutrophils and macrophages are severely impaired in diabetes and this impairment is associated with the prolongation or failure of the inflammatory phase in chronic wounds. Macrophages go into phenotypic transition (M1 to M2) during the wound healing process. During the early inflammatory phase, the expression of interferon-gamma (IFN-γ) and tumor necrosis factor-alpha (TNF-α) produces proinflammatory M1 macrophages [3]. M2 macrophages have anti-inflammatory/profibrotic activities, which are required for the resolution of inflammatory cells. Activated M2 cells are necessary for tissue remodeling and angiogenesis. Therefore, the transition of M1 macrophages to M2 macrophages is a potent driving force for the progression between inflammatory and tissue remodeling phases [4].

After the injury, the wound typically becomes hypoxic due to damage on blood vessels. Hypoxic conditions induce keratinocyte migration and the expression of growth factor and cytokines, including vascular endothelial growth factor (VEGF), PDGF, and TGF-β. In the normal wound healing process, the injury site is cleaned in the inflammatory phase, fibroblast and endothelial cells construct an early granulation tissue, and wound contraction begins afterwards [5].

Keratinocytes, fibroblasts, endothelial cells, extracellular matrix (ECM) proteins and angiogenesis are the main players of the proliferation phase. Fibroblasts produce collagen as well as glycosaminoglycans (GAG) and proteoglycans, and are required for the re-epithelialization and restoration of epidermal integrity. Angiogenesis, the formation of new blood vessels from existing ones, provides oxygen and nutrients to the wound area, where dermal and epidermal cells migrate and proliferate. The induction and sustainability of angiogenesis is crucial for the proliferation phase. In addition to the expression of proangiogenic factors and growth factors, endothelial progenitor cells (EPC) direct endothelial cells to the wound site and contribute to the re-vascularization process. During the transition between proliferation and remodeling phases, the wound undergoes physical contraction, which is mediated by myofibroblasts. Myofibroblasts are modified from fibroblasts in granulation tissue and express alpha-smooth muscle actins. In normal wound healing, myofibroblasts eventually disappear by apoptosis and a scar tissue is ultimately formed [6].

Tissue remodeling is characterized by the replacement of collagen type III with type I, this process is also called as collagen deposition. The proportion and balance between collagen type III and I differs between normal and chronic wounds. Collagen is a keystone of skin formation and repair, and its expression and degradation is essential for skin tensility and elasticity. Matrix metalloproteins (MMPs) and other enzymes are main players that facilitate cell movement and the eventual remodeling of ECM. At the final phase of wound healing, the number of vessels also decreases and the ECM architecture closely resembles the normal tissue.

Wound healing is a complex biological process that consists of the four above-described phases and involves the action of large numbers of cells including neutrophils, macrophages, lymphocytes, keratinocytes, fibroblasts, and endothelial cells. Multiple factors can cause

impaired wound healing by affecting one or more phases of the process. Patients with diabetes, obesity, chemotherapy, infection, radiation, diabetes mellitus and arterial or venous insufficiency are more likely to have impaired chronic wounds [32].

2.2.2. Role of Angiogenesis in Wound Healing

Oxygen and nutrient requirements are dramatically increased in the wound tissue due to damage to blood vessels. Restoring blood flow to the site of injury is therefore critical for the maintenance of cytokines and cellular proliferation at the wound site [7]. It is well established that angiogenesis is severely impaired in diabetic wounds [33]. Failure of angiogenesis also effects macrophage function, collagen accumulation, granulation tissue formation, keratinocyte migration and proliferation, and the functions of ECM components [33].

Angiogenesis contains multiple steps, including vasodilation, basement membrane degradation, endothelial cell migration, and endothelial cell proliferation [32]. Angiogenesis of wound healing is partially different than angiogenesis in wound neovascularization. When tissue damage occurs, clot formation is initially maintained by thrombin, which upregulates expression of VEGF. Platelet cells also contribute to the activation of angiogenic growth factors such as TGF-α and TGF-β, VEGF, PDGF, and angiopoietin-1 (Ang-1). Therefore, thrombin and platelets are the main players for the initiation of angiogenesis. In the second step, angiogenesis amplification, monocytes and macrophages release growth factors and pro-inflammatory cytokines which are able to vascularize tissues. The hypoxic condition of wound promotes the expression of HIF-1α and triggers VEGF production. The vascular proliferation step is characterized by the improvement of angiogenesis in the wound area and greater blood flow at the site of injury. Vascular stabilization is managed by Ang-1, alpha-smooth muscle actin (α-SMA) and pericytes.

Pericytes wrap around the capillaries and are able to guide both the sprouting process and maturation of vessels. PDGF is responsible for the recruitment of pericytes to newly formed vessels [34]. The final stages of angiogenesis in wound healing are suppression of angiogenesis. A decrease in growth factor expression and the expression of endogenous angiogenesis inhibitors, which demonstrate that angiogenesis is complete.

2.2.3. Applications of nanomaterials for the enhancement of the wound healing process

The development of biodegradable and non-toxic materials for the enhancement of the wound healing process is an active area of research, and advances in nanotechnology have contributed greatly to the design efficiency of such materials. Nanobiomaterials allow the design of wound dressings that not only create a suitable biomolecular environment for the regeneration process to occur, but also protect against infections at the wound site and facilitate the controlled release of biomolecules such as growth factors.

Natural and synthetic polymers, such as polysaccharides (*e.g.* alginates, chitin, chitosan, heparin, chondroitin), proteoglycans and proteins (*e.g.* collagen, gelatin, fibrin, keratin, silk fibroin, eggshell membrane) are commonly used in wound management, as those materials display low toxicity and can be naturally degraded over time in the body. The large surface-to-volume ratios inherent to nanoscale materials is another major advantage, and allows a small volume of material to contain large amounts of therapeutic cargo. Advances in the design of soft materials, such as hydrogels and bio-scaffolds, have revolutionized the field of wound management research, as these materials can be engineered to provide both the biophysical environment and biochemical signals necessary for the wound regeneration process.

Wound dressings protect the damaged tissue against pathogens and assist the recovery of dermal and epidermal tissues. The choice of dressing material depends on the cause and type of the wound, and both natural and artificial dressings can be used.

2.2.3.1 Artificial Skin

An "artificial skin" that can adequately replace damaged skin tissue is the ideal type of wound dressing, and considerable effort has been expended on developing such a material. Natural skin transplantation is the first choice for clinicians and surgeons to replace damaged skin in severe burn injuries; though only large and deep wounds warrant this procedure (skin grafting is generally not necessary for first and second degree burns, which heal with little to no scarring). On the other hand, the wound bed in third degree burns must be covered as quickly as possible with artificial or natural grafts [35]. Donor areas for natural skin transplantation include the chest, thigh, buttock, abdomen, or behind the ear. However, as the donor region must contain healthy skin, the procedure is not recommended for elderly patients with pressure sores and people with diabetic or other chronic ulcers. The treatment of these patients therefore necessitates the development of tissue engineering techniques for the artificial replacement of skin.

Artificial tissues generally incorporate three main elements: a cell type, a differentiation-inducing substance, and a matrix. Skin substitutes might be biological (*e.g.* xenografts, allografts, autografts and amnionic substitutes) or synthetic [36]. Xenografts are skin substitutes harvested from animals, and serve as a temporary, insulating layer during early stages of wound healing in humans. Allotransplantation, which refers to the transplant of substitute skin from the same species, allows a potential means of rapid intervention in burn wound management. Cadaveric skin allografts are one of the most common biological substitutes worldwide. There are two main

strategies to preserve cadaveric skin allografts; cryopreservation and glycerol preservation. Glycerol has antibacterial and antiviral effects and is more cost-efficient for long-term storage and long-distance transport compared to cryopreserved skin. Amniotic substitutes derived from placentae of selected and screened donors are rich in collagen and various growth factors that support the healing process, thus improving wound closure rates and reducing scar formation [36].

Although these naturally-derived skin substitutes are widely used in clinics, they cannot facilitate the complete regeneration of skin due to limited donor sites, risk of infection, slow healing rates and, in the case of autografts, the requirement to create new wounds to acquire the required skin tissue. As such, there is a substantial need for tissue-engineered skin constructs that support the complete regeneration of wound injuries. The development of artificial skin tissue may also enhance the scope of regenerative medicine, and techniques used in artificial skin production may be expanded for the generation of more complex structures, such as artificial organs. Additionally, advances in the design of therapeutic agents will also lead to a greater understanding of the pathophysiology of the wound healing process.

2.2.3.2. Natural Nanomaterials in Wound Healing

Natural materials are required to exhibit certain characteristics to be considered suitable for use as wound dressings. Foremost among these criteria is the ability to serve as an adequate matrix scaffold for the cell types involved in the wound healing process (including stem cells, macrophages, fibroblasts and/or epithelial cells). Also important is the ability to incorporate essential molecular signaling elements such as growth factors and signaling molecules. These functions allow the nanomaterial dressing to reduce inflammation, scar formation and infection; they may also play a role in various other processes. A large number of natural materials, such as

collagen, gelatin, laminin and chitin/chitosan have been used as electrospun scaffolds for tissue engineering.

2.2.3.3. Collagen

Collagen is the major protein of the extracellular matrix (ECM) and acts as a structural scaffold in various tissues [37]. Types I and III are the main types of collagen found in skin tissue. Collagen subunits pack together to form long, thin fibrils, which typically assume a triple-helical structure. Triple-helices of type I collagen consist of two α1(I) chains and one α2(I) chain, while these of type III collagen are composed of three α1 chains. Collagen fibers in skin are mainly synthesized by fibroblasts and myofibroblasts. Collagen deposition occurs at the wound site following the third day post-injury, and involves the replacement of type III collagen with type I. The replacement process gradually increases the stiffness and tensile strength of the regenerating tissue, as the tensile strength of type I collagen is greater than that of type III collagen.

It is known that collagen not only serves as a structural support, but also contributes to matrix deposition and cellular differentiation and migration during the wound healing process. A number of collagen dressings have been reported in the literature, often incorporating additional materials such as alginate (to control material efflux from the scaffold) and silver particles (to provide antimicrobial effects). Some of these designs are commercially available and see frequent use in surgical or clinical procedures [38].

Apligraf (Graftskin) (Organogenesis/Novartis, Canton, MA) is a wound dressing product that contains allogeneic neonatal foreskin fibroblasts and keratinocytes in bovine collagen gel; it is used in the treatment of chronic foot ulcers and venous leg ulcers. *Cellular-allogeneic* OrCel (Ortec International, New York, NY) contains both fibroblasts and keratinocytes from neonatal

foreskin, cultured in a type I collagen sponge. It is used for treatment of split-thickness donor sites in patients with burn and surgical wounds in epidermolysis bullosa [39]. Cultured skin substitutes, composed of collagen-glycosaminoglycan substrates containing autologous fibroblasts and keratinocytes, facilitate permanent wound closure in burn injuries and congenital nevus and chronic wounds [40].

The porous structure, high permeability, hydrophilicity, stability and cell-supporting nature of collagen make this material a popular choice for wound dressings. In addition, the development of new material combinations of collagens and engineered skin substitutes may further enhance the utility and versatility of wound dressings in clinical use.

2.2.3.4. Laminin

Laminin is a widely expressed protein that contributes to the formation of the extracellular matrix, particularly the basement membrane. Laminins comprise a family of at least 15 large trimeric basement membrane proteins, each of which is composed of one α, one β and one γ chain and may display a distinct, tissue-specific biological role [41]. Laminin is critical for the cell-material interactions that occur during the wound healing process and promote cell proliferation and attachment. Defects on laminin expression have been correlated with delayed or impaired wound closure. Junctional epidermolysis bullosa (JEB) is an inherited disease affecting laminin and collagen expression and characterized by fragility of the skin and mucous membranes. Laminin 5 is highly expressed in migrating keratinocytes in the wound bed [42]. Due to its role of promotion of cell proliferation and attachment, laminin derived peptides are also used as wound dressing [43, 44]. In the peptide based approach, topical application of laminin derived peptides with angiogenic properties and binding affinity to integrin αvβ3 and α5β1, was shown to increase re-epithelization and granulation tissue formation in the early stages

after wounding in rats [43]. Similarly application of peptide conjugated scaffolds to the wound area for example PPFLMLLKGSTR peptide derived from LG3 domain of a3 laminin, increased rates of skin re-epithelialization [45].

2.2.3.5. Chitin and Chitosan

Chitin and chitosan are natural polysaccharides that display suitable biological and physicochemical characteristics for use as wound dressings. Their main advantages are oxygen permeability, biodegradablity and biocompatibility and they are easily processed into hydrogels, fibers, membranes, scaffolds and sponges. Chitin is an inexpensive product obtained from invertebrate exoskeleton. Chitosan is composed of randomly distributed β-(1-4)-linked D-glucosamine and N-acetyl-D-glucosamine units. After depolymerization N-acetyl-D-glucosamine units induce fibroblast proliferation, are critical for collagen deposition and stimulate natural hyaluronic acid synthesis leading to faster wound healing and scar prevention.

Chitin-nanosilver composite scaffolds were found to possess excellent antibacterial activity against bacterial infection during the wound healing process [46]. Chitin and chitosan can also be used as slow-release drug-delivery vehicles for growth factors to further accelerate the wound healing process [47].

2.2.3.6. Alginate based nanomaterials

Alginates are unbranched polysaccharides extracted from brown algae. Alginate-based wound dressings display hemostatic properties and are commonly used in bleeding wounds and burns. Materials such as calcium alginate, calcium sodium alginate, collagen alginate and gelatin alginate are highly absorbent natural fiber dressings, and can be obtained at minimal cost from processed algae. The high absorption capability of alginate facilitates the creation of a moist

environment that promotes the formation of granulation tissue during the wound healing process [48]. The high water absorption capacity of alginate also helps to reduce blood loss from wounds. Chemical modifications with calcium and zinc can also be performed to improve the efficiency of alginate over conventional cotton wound dressings.

2.2.3.7. Synthetic nanomaterials in wound healing

Synthetic materials allow greater control over properties such as porosity, controlled release capacity, biodegradability and structural versatility, in addition to avoiding issues inherent to natural materials such as batch-to-batch variance and viral or bacterial contamination. As such, they have been commonly used in the design of novel regenerative scaffolds that aim to provide optimum conditions for regeneration with high reproducibility. Increased control over material structure and composition is a major advantage for synthetic skin substitutes, the ultimate goal of which is to produce an ideal skin substitute that provides effective and scar-free wound healing.

2.2.3.8. Carbon nanotubes

Carbon nanotubes (CNTs) are currently under consideration for clinical applications regarding wound healing, although there are serious concerns over the toxicity of these materials. Carbon nanotube-based antiseptic bandages were produced by combining povidone-iodine with single wall carbon nanotubes (SWNTs) [49], and it has been shown that the presence of the multiwalled carbon nanotubes (MWCNTs) positively affects the wound healing process by decreasing the expression of genes that interfere with the function of the cytoskeleton, such as actin stress fibers [50].

2.2.3.9. Hydrogels

Hydrogels promote granulation, epithelialization and autolytic debridement at the wound site by providing a moist environment that is conductive to the regeneration process. Commercially available hydrogel dressings are generally found in the form of membranes and sheets. Studies involving the *in situ* formation of hydrogel wound dressings based on gelatin, oxidized alginate and borax suggest that the application of hydrogels enhance the wound healing process in the rat model [51].

Full-thickness wounds dressed with a combination of chemically-crosslinked glycosaminoglycan (GAG) hydrogels and the commercial wound dressing Tegaderm™ displayed a significant increase in re-epithelialization at days 5 and 7 compared to wounds treated with Tegaderm™ alone, suggesting that modified hydrogels can improve the efficiency of treatments based on conventional wound healing agents [52]. Hydrogels can also be improved through the incorporation of drugs or growth factors.

2.2.3.10. Antimicrobial nano-based dressings

The antimicrobial properties of silver have been known and utilized for centuries, and the material has lately been used in wound dressings for the same purpose. Silver nanoparticles with diameters below 100 nm display increased antimicrobial activity due to their larger combined surface areas. Several methods exist for the incorporation of AgNPs into wound dressings. On the other hand, safety of using silver nanoparticles, their fate within the body or the environment particularly on open wounds, should be further addressed.

2.2.3.11. Wound dressings containing growth factors

Growth factors are soluble secreted proteins capable of affecting a variety of cellular processes involved in tissue regeneration. However, their clinical applications are limited due to the absence of robust delivery systems and biomaterial carriers. Nonetheless, growth factors have been found to speed the healing of acute and chronic wounds in humans, and some are approved for clinical use by the FDA. The platelet-derived growth factor (PDGF) analogue Regranex™, for example, is currently used for the treatment of leg and foot ulcers in diabetic patients [53]. Endothelial growth factor (EGF) is another major factor in wound regeneration and has been reported to play a role in keratinocyte migration, fibroblast proliferation and differentiation, and granulation tissue formation [54]. In addition to its rapid breakdown within the wound environment, EGF has a mitogenic effect upon cells [54].

From VEGF family composed of VEGF-A, VEGF-B, VEGF-C, VEGF-D, and placenta growth factor, VEGF-A is highly expressed in the acute wound and promotes angiogenesis. The main initiator of expression of VEGF is hypoxic environment and VEGF-A improves reepithelialization of diabetic wounds via enhancement of vessel formation [55].

Basic fibroblast growth factor (bFGF) is another growth factor responsible for induction of angiogenesis, most critical step during wound repair. Treatment of rabbit ear with exogenous bFGF accelerated wound healing comparing to non treated control, however no increase was observed in capillary density [56].

Although the topical application of growth factors is used for the treatment of chronic wounds, these materials are released in a non-controlled manner if not encapsulated within a controlled delivery matrix. Slow release is required for the effective delivery of these polypeptides to the

wound, and matrix-encapsulated growth factors will better enhance the wound regeneration process.

2.2.3.12. Biomimetic materials

Recent advances in material sciences and polymer chemistry have resulted in the development of biomimetic peptide fibers, an entire class of new nanomaterials that can be used to assist in wound regeneration. The extracellular matrix (ECM) is an enormously complex network of peptides, proteoglycans, growth factors and soluble proteins, and its components play critical roles at each and every step of the wound healing process. The dysfunction of any of these components may result in greatly delayed wound healing, as is observed in the chronic wounds of hyperglycemic patients. The development of biomimetic scaffolds that restore or replace the roles of ECM components may therefore allow the treatment of slow-healing dermal injuries that are currently difficult to treat using conventional approaches.

A bioengineered fibronectin matrix mimetic substrate was shown to induce cell migration and stimulate high rates of cell proliferation [57]. Similarly, collagen mimetic peptides that form a nanofibrous triple-helix formation were effectively used to enhance the thrombosis process [58]. Mesenchymal stem cells (MSCs) seeded on biomimetic collagen hydrogels significantly enhanced angiogenesis compared to MSC injection alone [59].

The main fabrication techniques to engineer such materials mimicking the nano-fibrous ECM proteins are electrospinning, self-assembly and phase separation. Development of those techniques allows the design and fabrication of biomimetic scaffolds that offer tremendous potential applications in wound healing of skin. The development of novel biomimetic scaffolds capable of promoting and directing new vascular network growth would eliminate a critical issue

in tissue engineering, serving as an efficient solution to the problems associated with chronic wound healing. Future research is expected to yield more information on the unique properties of biomimetic scaffolds.

2.2.3.13. Current challenges in the design of nanomaterials for chronic wound management

The World Health Organization (WHO) reports that 347 million people suffer from diabetes worldwide, and expects the disease to be the seventh leading cause of death in 2030. The incidence of diabetes has been on the rise, and may soon become one of the foremost public health challenges that the world will face in the decades ahead. Factors such as age, obesity, malnutrition, and vascular disease may contribute to wound infection and delayed wound healing in diabetic patients. The metabolic effects of diabetes, combined with reduced blood flow and neuropathies (nerve damage) associated with the disease, increase the chance of foot ulcers and the severity of wound infections, potentially leading to limb amputation and even death. The design of smart scaffolds is therefore necessary to increase the quality of life in patients suffering from diabetic ulcers and similar chronic wounds.

Due to the variations between the pathophysiologies of wound and burn injuries, it is difficult to develop an artificial dressing material that can facilitate optimal healing of all types of skin damage. The initial assessment of chronic wounds is therefore essential for the decision of wound dressing choice, which should be made by taking a full account of the wound and dressing characteristics. The choice of dressing should be based on wound size, depth, severity of infection, and location. Patients with severe infection should use an appropriate antibiotic therapy; additionally, the wound can be treated with silver and iodine products [60].

Chronic wounds can be classified into two main types; diabetic and vascular wounds, which are caused by diabetes mellitus and peripheral arterial disease, respectively.

Product Name	Type	Usage	References
AQUACEL®	Hydrofiber	Chronic wounds	[61]
AQUACEL® Ag	Hydrofiber containing silver	Leg ulcers, superficial pressure ulcers, partial-thickness burns	[62]
REGRANEX® (FDA Approved)	Gel containing platelet derived growth factor (PDGF)	Chronic and traumatic wound	[53]
OASIS®	Derived from porcine small intestinal submucosa (SIS)	Partial and full thickness wounds, pressure ulcers, venous ulcers, chronic vascular ulcers, diabetic ulcers, trauma wound	[63]
SANTYL® (FDA Approved)	Ointment, biological enzymatic debriding agent	Chronic dermal ulcers, severe burns	[64]
IODOFLEX®	Cadexomer containing silver	Chronic wounds	[65]

Table 2.1 Commercially available wound dressings and their recommended regions of application.

Table 1.1 summarizes commonly used biologically active dressings commercially available for different purposes. AQUACEL dressings incorporating (w/w) silver require daily changes. OASIS contains ECM product derived from the small intestinal submucosa of pigs. REGRANEX and SANTYL are FDA approved wound dressings that are used in treatment of chronic ulcers.

2.2.3.14. Nanomaterials used in the treatment of diabetic wounds

Increases in the number of patients with delayed diabetic wound healing has made it an urgent necessity to develop appropriate wound dressings for diabetic wounds. Decreased reepithelization and growth factor expression, a dysfunctional extracellular matrix, and impaired angiogenesis are the main major problems that interfere with the recovery of diabetic wounds.

Studies involving the local application of growth factors such as human EGF (hEGF) have showed that treatment with high concentrations of hEGF is effective in promoting wound healing in diabetic foot injuries [66]. It has been shown that recombinant human epidermal growth factor (EGF) immobilized in a copolymer of poly(ε-caprolactone) (PCL) and poly(ethyleneglycol) (PEG) may increase the proliferation and phenotypic expression of keratinocytes [67]. Although materials such as collagen and hydrogels have been used to facilitate the healing of diabetic wounds, dressings that can encapsulate growth factors or other materials that induce angiogenesis are more favorable for this purpose. The encapsulation of growth factors in a polymer matrix not only protects the growth factor against enzymatic degradation in the body, but also allows its release into a localized area at a controllable rate. As such, current strategies for the treatment of diabetic wounds mainly involve the administration of materials that provide

the controlled release of growth factors. Since decreased angiogenesis is thought to contribute to impaired tissue repair, vascular endothelial growth factor (VEGF) is also commonly incorporated into scaffolds intended for use in the treatment of diabetic wounds [55]. In addition to delivery of growth factors, bioengineered mimetic materials such as heparin sulfate have shown an enhanced wound healing prowess compared to unloaded scaffolds [68].

2.2.3.15. Nanomaterials used in the treatment peripheral arterial disease

Peripheral arterial disease (PAD) is an atherosclerotic disease that is commonly seen in the elderly population. Diabetic PAD patients experience a gradual reduction in the delivery of oxygen- and nutrient-rich blood to the legs, which results in severe infections, osteomyelitis and a higher risk of lower leg amputations [69, 70]. PAD patients who also present with foot ulcerations tend to display other characteristics, such as neuropathic ulcers [71]. These ulcers are commonly located at the pressure points on the foot, mostly at the tips of the toes.

The lack of suitable natural materials and limitations of synthetic materials for treatment of PAD patients necessitate new route for effective clinical therapy. Combinations of proper dressings with endothelial progenitor cells (EPC) are important and exciting advances in the field of tissue engineering.

2.2.4. Peptide nanofiber gels for wound healing

Numerous materials for wound healing were mentioned in previous sections. Salient features of these materials are designed in an attempt to provide desired niches for a robust wound healing process. The fibrous structures of these materials allow them to serve as scaffolds for incoming cells. Growth factors or other bioactive molecules can be encapsulated or conjugated into the material to provide incoming cells with necessary biological signals. Cell adhesion epitopes can

be included in the material to facilitate cell attachment at the damaged site. Mechanical properties of the materials should be cognate to the tissue they will function in. In addition, these materials should be biodegradable and biocompatible. However, to gather all these properties in desired quality in one material is a formidable task. Obstacles here include the synthesis of the fibrous materials with fibers of nanoscale size, conjugation of the bioactive elements onto them and controlling the stiffness of the final product. On the other hand, nanofibrous materials formed by self-assembly of peptide amphiphile molecules have necessary features with remarkable consistency. Nanofibers with diameters varying from a few nanometers to a few microns can be obtained easily by this way. Their peptide part allows versatility in peptide epitopes and also provides an easy way for the addition of other chemical functional groups. Their structures are also comprised of biodegradable and biocompatible elements.

2.2.5. STZ induced Diabetic Model

Chemically induced diabetic models lead to the destruction of beta cells through injection of substances such as streptozotocin, alloxan, vacor, dithizone and 8-hydroxyquinolone [8]. STZ [2-deoxy-2-(3-(methyl-3-nitrosoureido)-d-glucopyranose] is the most common chemical used for the induction of type I diabetes and synthesized by *Streptomycetes achromogenes* [9]. It kills beta cells that are responsible for insulin secretion, and is readily taken inside these cells via Glu-2 transporters [9]. The main disadvantage of toxin-mediated diabetic models is the fact that chemicals disturb not only the pancreas, but also other organs of the animal. STZ induced type I diabetes can be created via high-dose injection or low-dose repeated injections. In single high dose injections, the concentration of STZ ranges from 100 to 200 mg kg^{-1}, while in multiple low-doses, the administered amount is 20 to 40 mg kg^{-1}. High-dose injection of STZ might cause the death of animals. Low-dose of injection of STZ for more than 5 days causes severe reductions in

insulin secretion capacity and finally leads to the formation of type-I diabetes. STZ induced diabetes is widely used in wound healing studies since it is the simplest model of induction for hyperglycaemia [10, 11].

2.3. Results

2.3.1. Synthesis of PAs

Peptide amphiphiles (PA) used in the formation of bioactive GAG-PA/K-PA and non-bioactive E-PA/K-PA gels were synthesized by solid phase peptide synthesis method. Lauryl-VVAGEGDK(pbs)S-Am (GAG-PA) was previously designed to mimic sulfated GAGs by presenting sulfonate, hydroxyl and carboxylate groups, while Lauryl-VVAGE-Am (E-PA) was used as the non-bioactive control peptide (Figure 2.1). Positively charged Lauryl-VVAGK-Am (K-PA) was used to induce nanofiber formation through electrostatic interaction with negatively charged GAG-PA or E-PA. Peptide amphiphiles were characterized by LC-MS and purified with preparative HPLC (Figure 2.2).

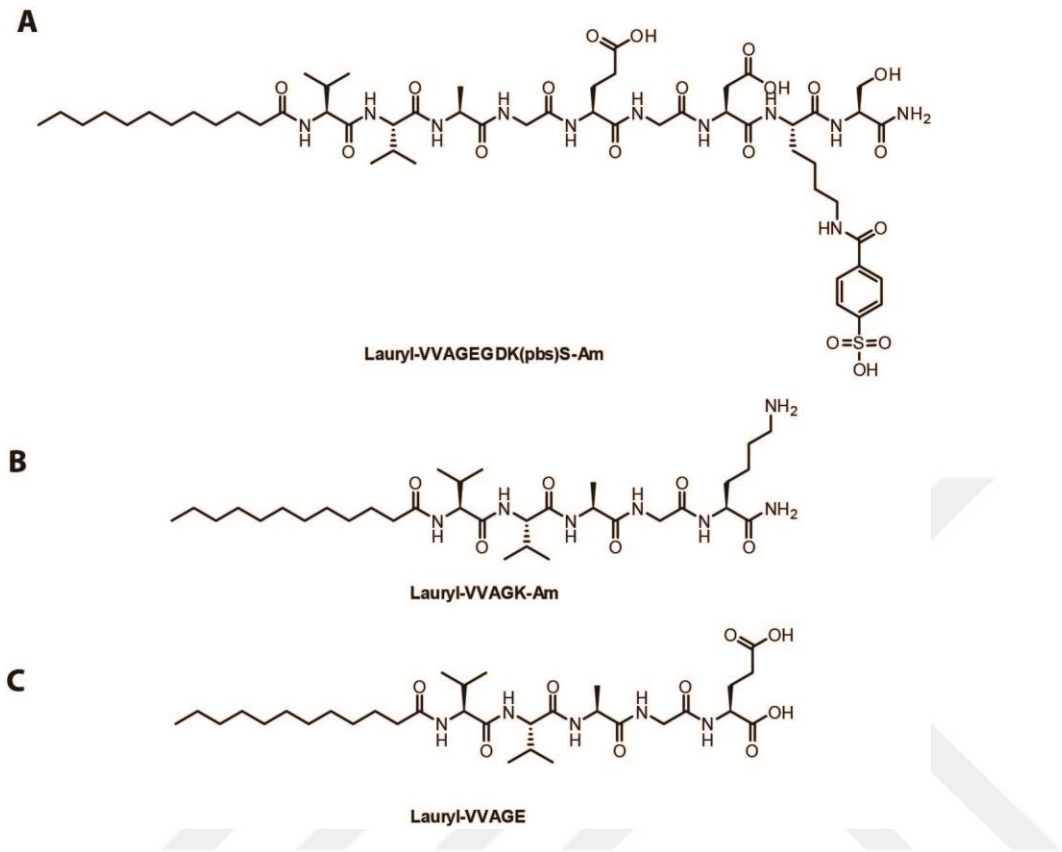

Figure 2.1 **Self-assembled peptide amphiphile (PA) nanofibers.** Chemical structures of GAG-PA (A), K-PA (B) and E-PA (C) are shown.

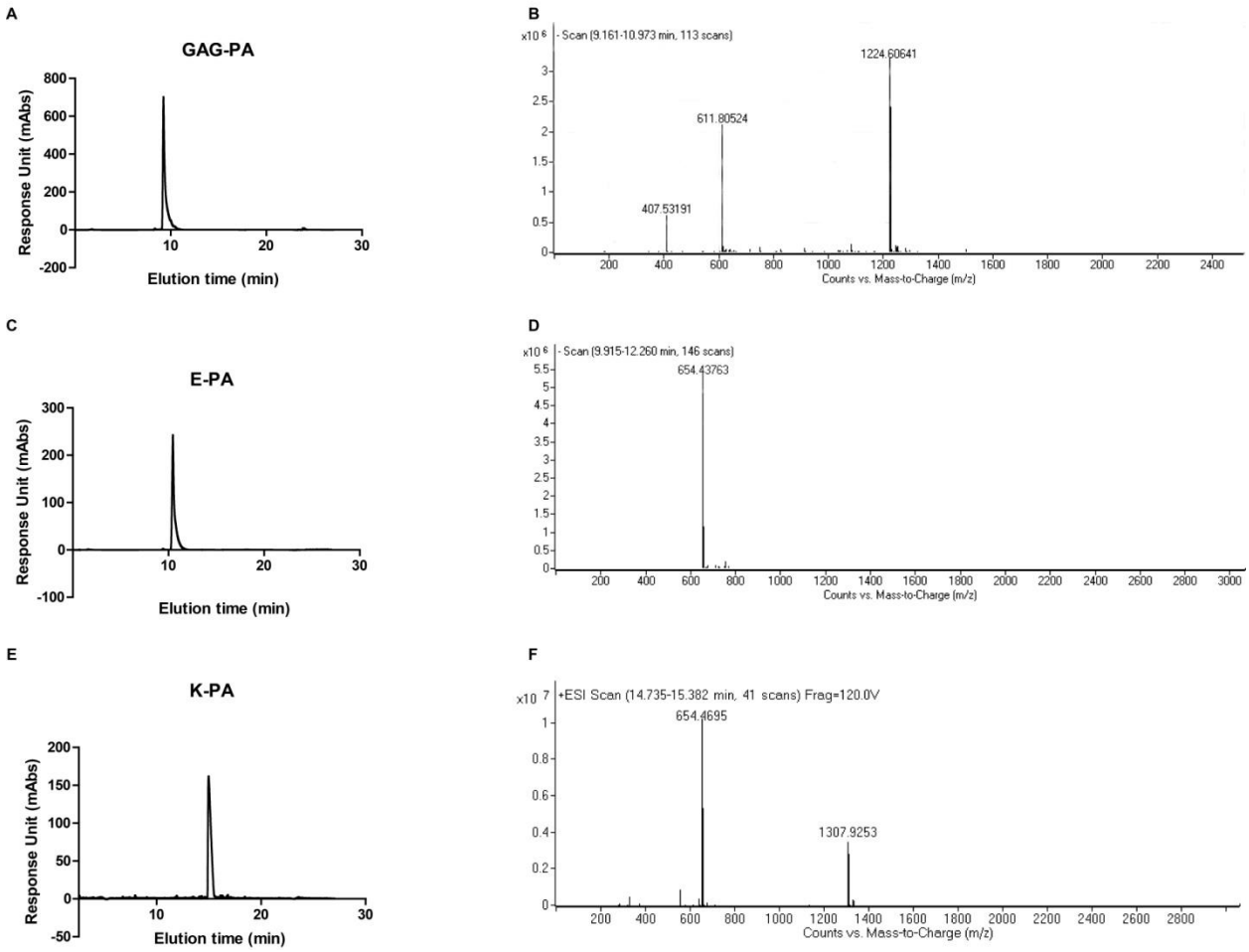

Figure 2.2 Liquid chromatography and mass spectroscopy of PA molecules. HPLC chromatogram of purified GAG-PA (A), E-PA (C), K-PA (E) molecule at 220 nm. Mass spectra of peptides; for GAG-PA $[M-H]^-$ (calculated) = 1224.80, $[M-H]^-$ (observed) = 1224.60, $[M/2-H]^-$ (calculated) = 611.80, $[M/2-H]^-$ (observed) = 611.80, $[M/3-H]^-$ (calculated) = 407.53, $[M/3-H]^-$ (observed) = 407.53 (B), for E-PA $[M-H]^-$ (calculated) = 655,82 $[M-H]^-$ (observed) = 654.43 (D), for K-PA $[M+H]^+$ (calculated) = 653.89, $[M+H]^+$ (observed) = 654.46, $[2M+H]^+$ (calculated) = 1308.76, $[2M+H]^+$ (observed) = 1307.92 (F).

2.3.2. SEM analysis

SEM images revealed that the peptide nanofibers formed by the PA molecules exhibited a nanofibrous network that showed similar morphology to natural ECM (Figure 2.3).

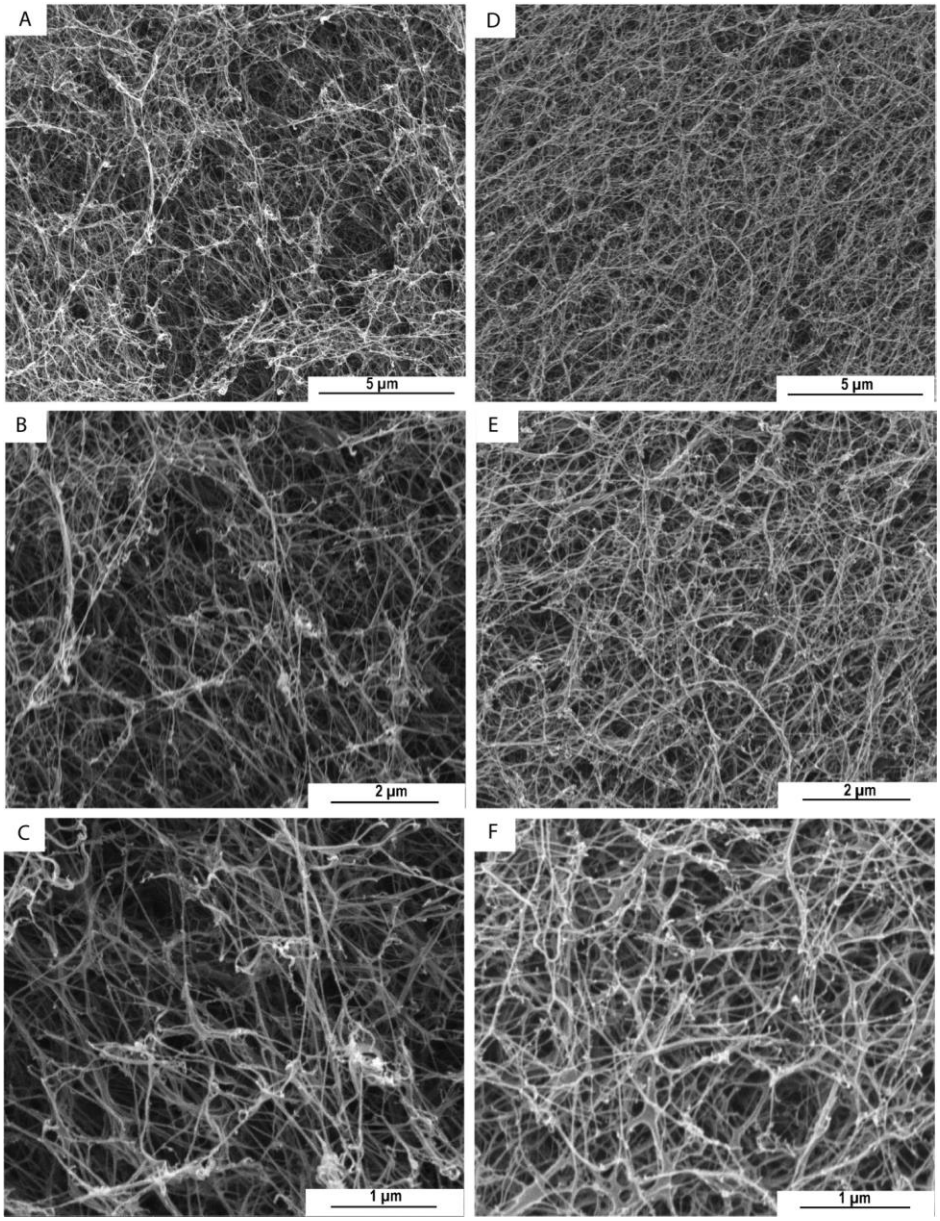

Figure 2.3 SEM images of peptide amphiphile nanofiber matrices. GAG-PA/K-PA (A,B,C) and E-PA/K-PA (D,E,F).

2.3.3. Circular dichroism analysis

To analyze secondary structure of nanofiber formation of peptide amphiphiles and their mixtures, circular dichroism (CD) spectroscopy was employed. CD results showed that the nanofibrous structures formed by the PA molecules contained β sheet structures as evidenced by absorbance maximum at around 200 nm and minimum at around 220 nm (Figure 2.4).

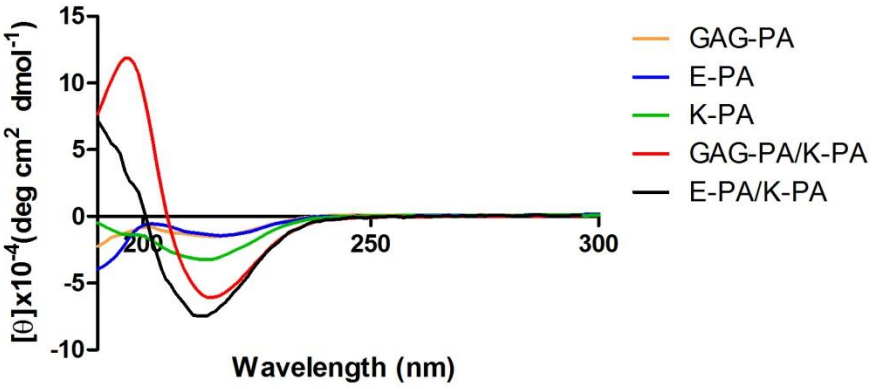

Figure 2.4 Characterization of secondary structure of peptide amphiphiles by circular dichroism. GAG-PA/K-PA and E-PA/K-PA showed nanofiber networks contain β-sheet secondary structure.

2.3.4. Oscillatory Rheology Analysis

Oscillatory rheology was performed to investigate the mechanical properties of peptide amphiphile gels (Figure 2.6). The concentrations of the gels were identical to these used in *in vivo* experiments. Storage (G′) and loss (G″) moduli were scanned from 100 to 0.1 rad/s of angular frequency and with 0.5% shear strain. Rheology results indicated that both bioactive and non-bioactive PA molecules formed gels as storage moduli were higher than loss moduli. The visual observation of PA mixtures also supported the gel formation (Figure 2.6). Additionally,

measurements showed that GAG-PA/K-PA and E-PA/K-PA gels had similar mechanical properties with stiffness values within a range of 3-8 kPa.

Figure 2.5 Photograph of the angiogenic gel formed by GAG-PA and K-PA peptide solutions.

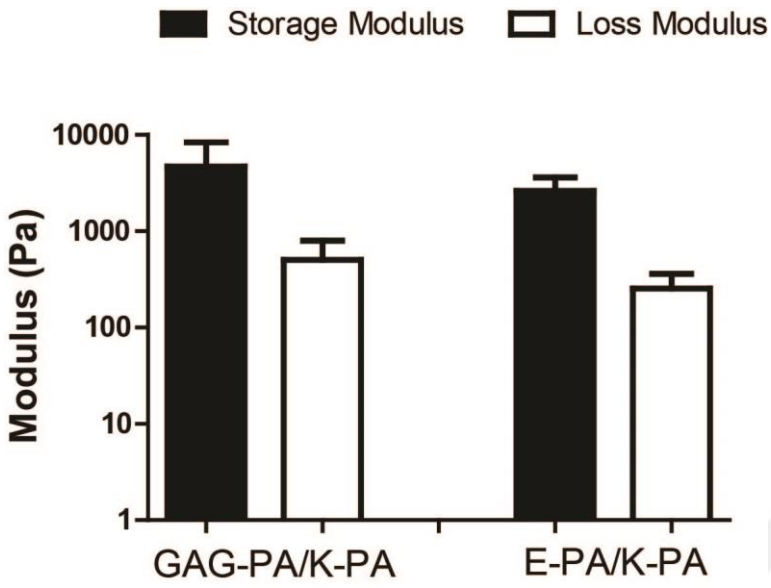

Figure 2.6 Self-assembled peptide amphiphile (PA) nanofibers. Storage and loss moduli of PA gels were measured at 0.5% of shear strain and scanned from 100 to 0.1 rad/s of angular frequency. Rheology results showed gelation as a result of nanofibrous network formation by GAG-PA/K-PA and E-PA/K-PA at pH 7.4.

2.3.5. STZ induced diabetic rat wound model

Type 1 diabetic rat model was created with STZ injection (45 mg/kg). Rats consistently became hyperglycemic after three weeks. Animals with blood glucose levels above 20 mmol/L were used in wound healing experiments. The body masses and blood glucose levels of the animals showed no statistically significant difference until the end of the experimental periods ($p > 0.05$) (Figure 2.7).

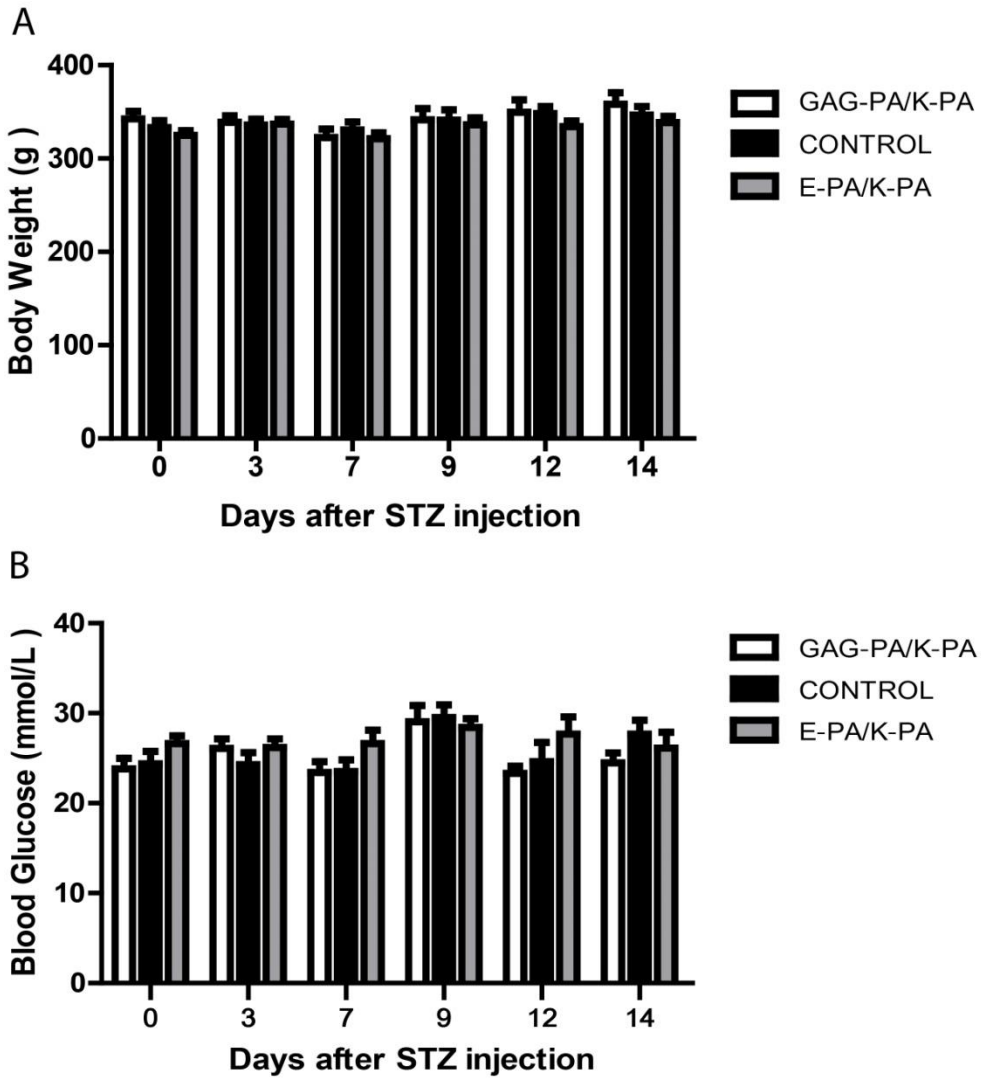

Figure 2.7 Body weights and blood glucose levels of animals. Changes in body weights (A) and blood glucose levels (B) of diabetic rats after cutaneous full-thickness excision wound creation (day 0). No significant difference was observed between groups at different time points ($p < 0.05$).

The STZ induced diabetics rats were sterilized before the wound creation. As seen in a schematic representation of rat, 3 wounds are created at the dorsal part of the animal and each animal has one type of treatment; bioactive gel, non-bioactive gel or PBS controls (Figure 2.8).

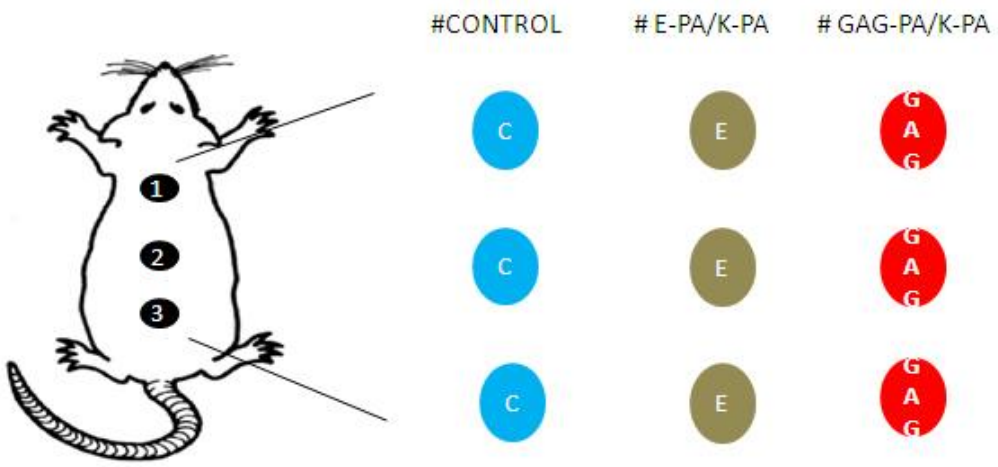

Figure 2.8 Schematic representation of wound locations and treatments. C-PBS control; E-nonbioactive gel; GAG- glycosaminoglycan mimetic gel, each animal received a single treatment type across all three wounds.

2.3.6. Wound closure was accelerated in bioactive gel treated wounds

Wound closure rates (%) were calculated for each group to investigate whether GAG-PA/K-PA gel treatment accelerates wound closure in diabetic rats. Following excision of full-thickness *skin* lesions, no significant difference was observed in wound closure between the three groups by day 3. At days 7, 9 and 14, wound closure was significantly accelerated in GAG-PA/K-PA treated groups compared to E-PA/K-PA and PBS treated controls (Figure 2.9, Figure 2.10). Bioactive gel treated rats exhibited rapid wound closure after day 3 and approached nearly 80% of closure by day 14 post-injury. In contrast, E-PA/K-PA and PBS treated diabetic control rats exhibited impaired closure.

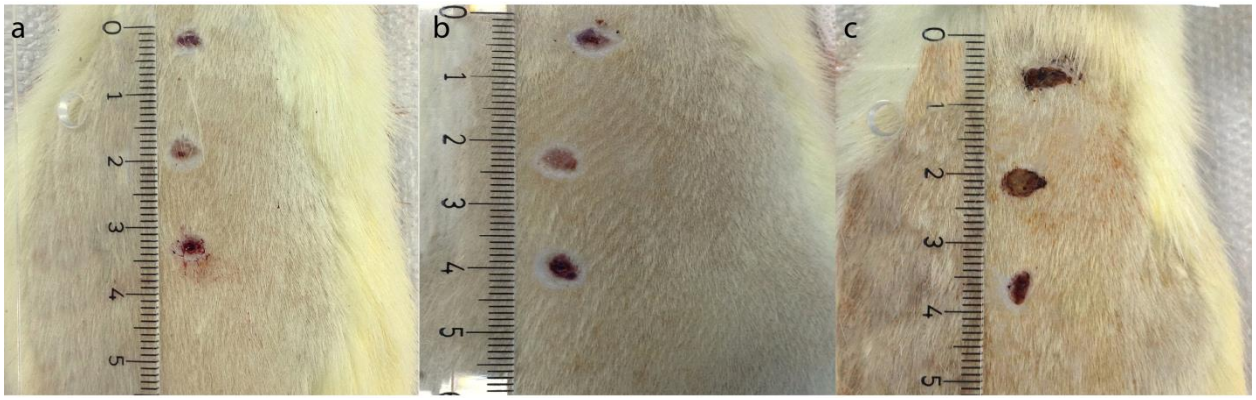

Figure 2.9 Wound closure was accelerated in GAG-PA/K-PA treated wounds compared to controls. Photos of wounds (day 9) treated with GAG-PA/K-PA (a), PBS–control (b), and E-PA/K-PA (c).

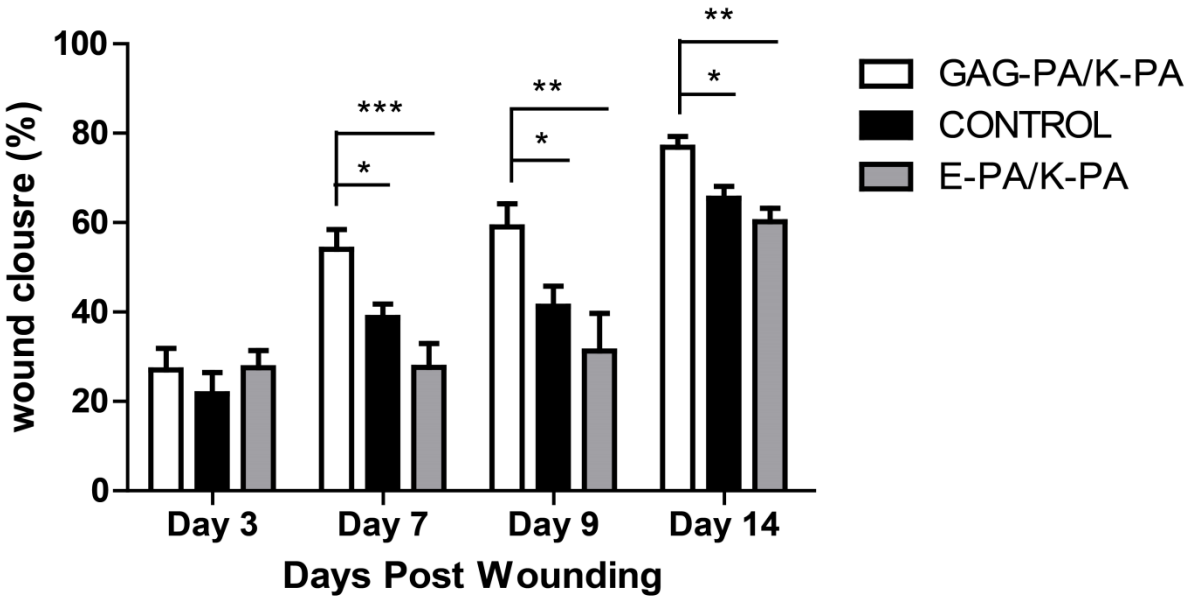

Figure 2.10 Percentages of wound closure areas in STZ-induced diabetic rats. One-way ANOVA analysis was performed. Statistical differences are indicated as: * $p < 0.05$, ** $p < 0.01$, and *** $p < 0.001$, $n = 15$.

2.3.7. Bioactive gel treatment accelerates re-epithelialization in wound tissues

Keratinocyte proliferation and migration are critical for optimal wound healing, not only because of their role in the proliferation phase but also for their importance in the remodeling of skin tissue. Re-epithelialization scoring, epithelial thickness measurement and granulation tissue area calculation were performed to analyze the healing rate of wounds in diabetic rats (Figure 2.12, Figure 2.13). Although progressions of re-epithelialization were similar between the groups on day 7, GAG-PA/K-PA treated wounds exhibited nearly complete re-epithelialization compared to moderate epithelialization of controls on day 9 (Figure 2.12). In E-PA/K-PA treated rats, the dermal closure rate was similar to that in PBS treated rats. In the later stages of wound healing, however, re-epithelialization was complete for all groups (day 14). The distance between epithelial tips was calculated from each group (Figure 2.13). While not statistically significant, distance between epithelial tips was reduced in GAG-PA/K-PA treated groups at day 7 and 9. The epidermal thickness of regenerated skin was also measured for all groups to further investigate the effect of bioactive gel treatment on re-epithelialization. The thickness of bioactive PA treated epidermis was significantly greater than control groups on days 7 and 9 (Figure 2.12).

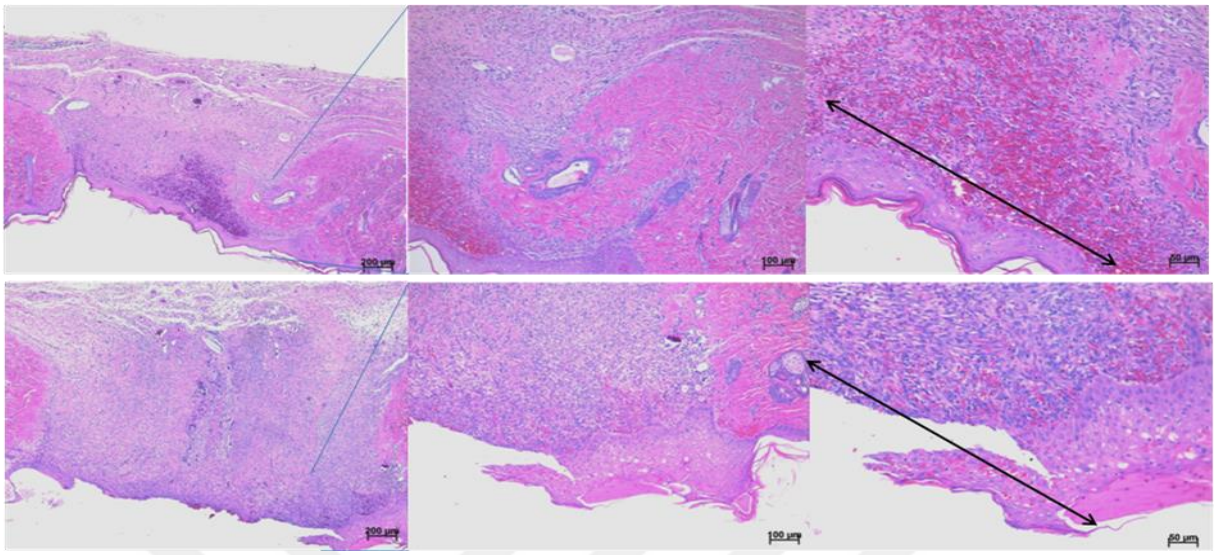

Figure 2.11 H&E staining of GAG-PA/K-PA and control tissue sections from day 7. Formation of granulation tissue area and re-epithelialization were faster on bioactive gel treated group (above).

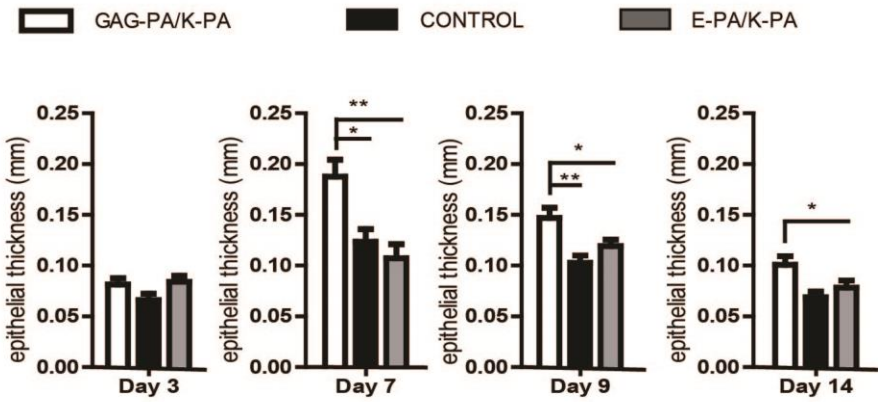

Figure 2.12 Epithelial thickness (mm) of wound tissue sections is correlated with healing rate.

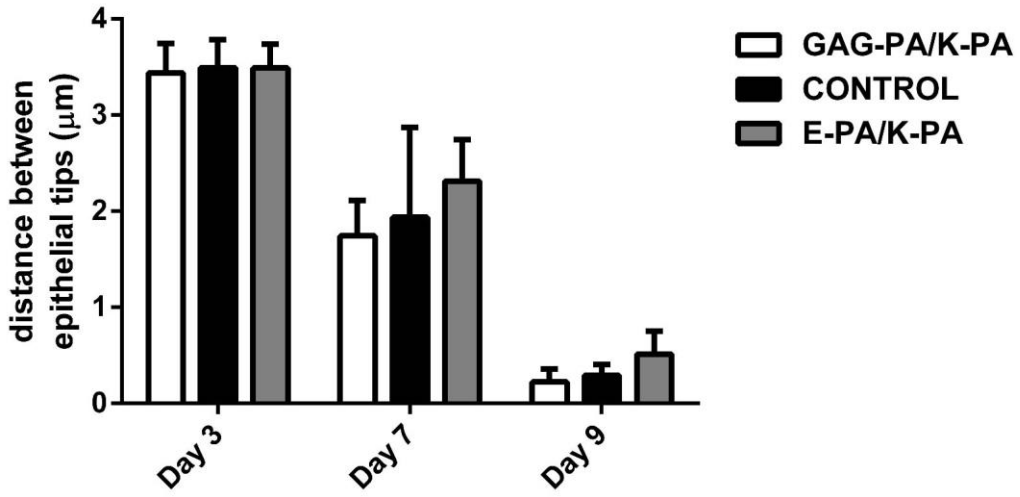

Figure 2.13 The distance between epithelial tips of GAG-PA/K-PA, E-PA/K-PA and control tissue sections. Distance was measured from epithelial tips of wound sections by using ImageJ.

2.3.8. Granulation tissue formation accelerated with bioactive gel treatment

Dermal regeneration was further characterized by visualization of granulation tissue formation both with H&E and Massons's trichrome staining on day 9 (Figure 2.14). Light microscopic examination on day 7 showed that granulation tissue per total wound area was 58% in the GAG-PA/K-PA treated groups whereas it was around 45% for other groups. At days 7 and 9,

granulation tissue area per total wound area was significantly higher in GAG-PA/K-PA treated group (Figure 2.15).

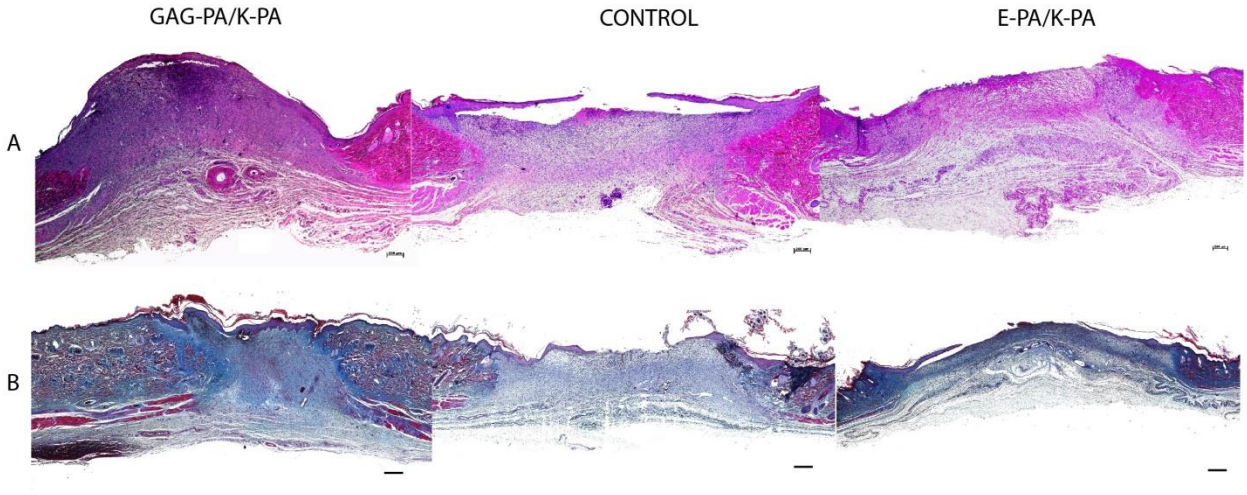

Figure 2.14 H&E and Masson's trichrome staining of tissue sections on day 9.

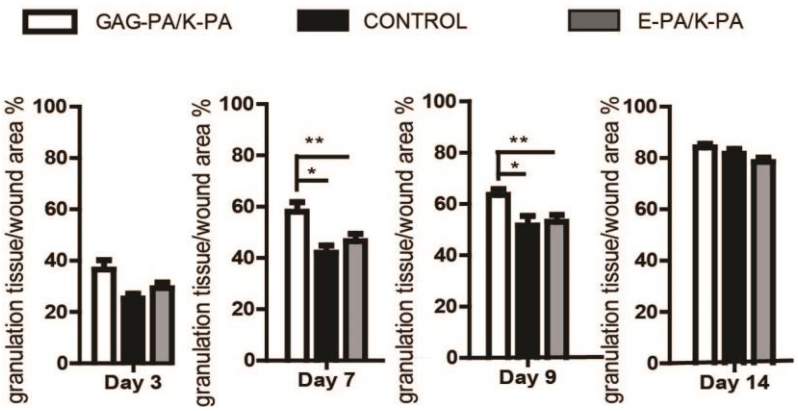

Figure 2.15 Quantification of total granulation tissue area to wound area on days after wounding. One-way ANOVA analysis was performed. * $p < 0.05$, ** $p < 0.0.1$

2.3.9. Collagen deposition

Massons's trichrome staining suggests that control and E-PA/K-PA treated sections have few and poorly arranged collagen bundles at the wound site on day 9 (Figure 2.14, Figure 2.17). On

the other hand, granulation tissue of GAG-PA/K-PA treated wounds contained thicker and better-organized collagen fibrils and bundles compared to controls (Figure 2.17). Although there was a dramatic difference of collagen organization between bioactive gel and controls on day 9, collagen deposition occurs in all groups on day 14 (Figure 2.16).

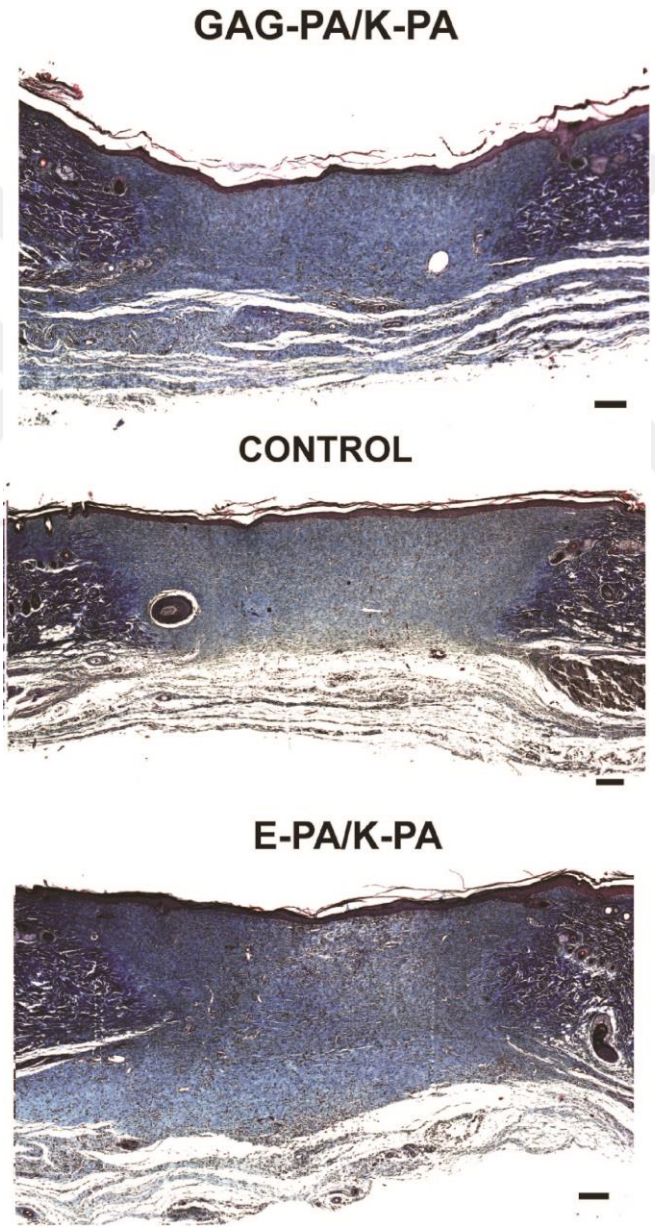

Figure 2.16 Masson's trichrome staining of GAG-PA/K-PA, control, E-PA/K-PA at day 14. Scale bars are 200 μm.

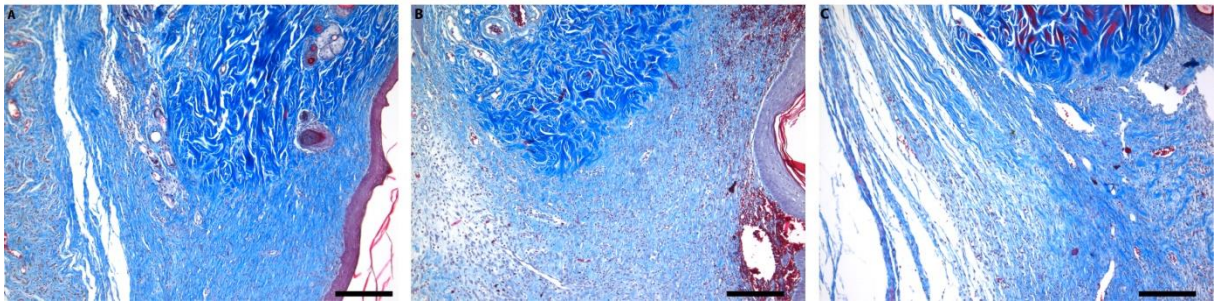

Figure 2.17 Masson's Trichrome staining of GAG-PA/K-PA, control, E-PA/K-PA at day 9. Original magnification 10x, scale bars = 200 µm. Blue color identifies collagen tissue, red color identifies keratin and muscle fibers.

2.3.10. GAG-PA/K-PA treatment induces myofibroblast activation

Tissue sections were stained with alpha smooth muscle actin (SMA) to monitor the transformation of fibroblast cells to into myofibroblasts in the wound area. At day 9, immunostaining of alpha SMA, showed that activated fibroblasts were abundantly located at the wound margins (Figure 2.18A-C). The positive immunostaining of alpha smooth muscle actin per granulation tissue was quantified at days 7 and 9 (Figure 2.18). The results of this analysis indicated that the number of myofibroblasts and intensity of staining were significantly higher in the granulation tissue area of GAG-PA/K-PA treated wounds compared to controls.

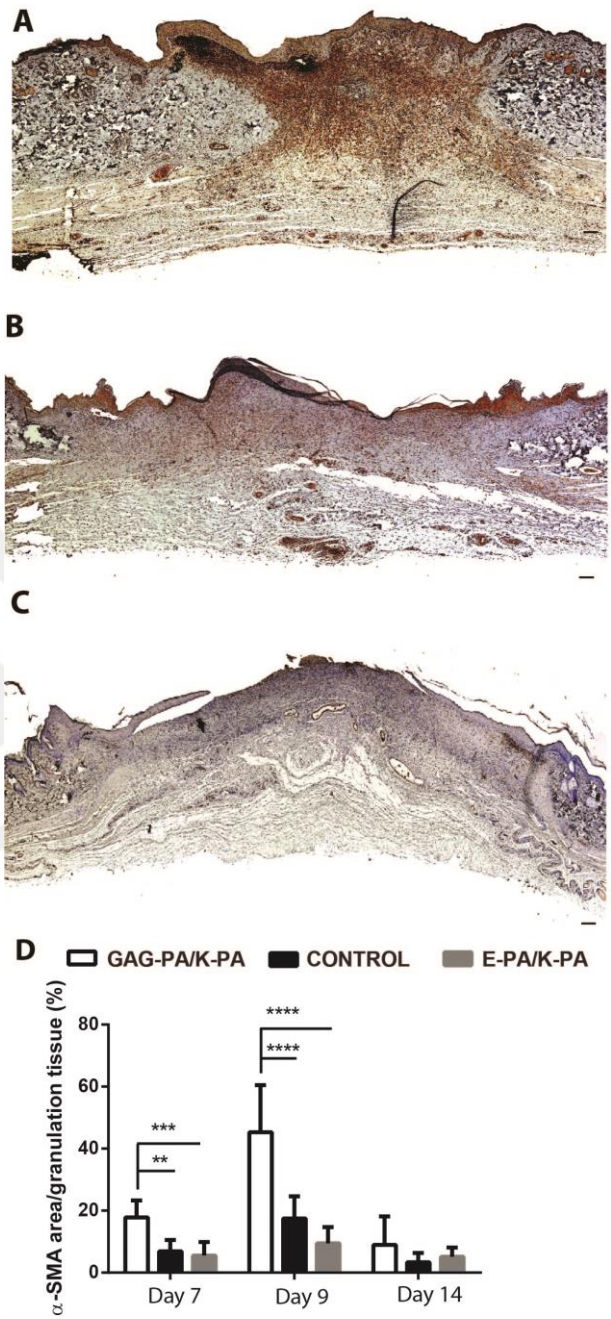

Figure 2.18 GAG-PA/K-PA treatment induced alpha smooth muscle actin expression in diabetic wounds. α-SMA staining (brown) of wound tissues on day 9 treated with GAG-PA/K-PA (A), control (B) and E-PA/K-PA (C), with hematoxylin counterstaining of nuclei (blue). Quantification of percentage of α-SMA positive staining per granulation area at indicated time

points (Day 7, 9 and 14) post wounding (D). Two-way ANOVA was performed. * $p < 0.05$, ** $p < 0.01$, and *** $p < 0.001$, scale bars = 200 µm.

2.3.11. Heparin mimetic PA nanofibers induce robust neovascularization in diabetic wounds

Since angiogenesis is a crucial event in wound healing especially for the closure of chronic wounds, we examined the efficacy of heparin mimetic peptide nanofibers to induce the neovascularization in diabetic skin tissue (Figure 2.19A-C). As evaluated by serial sectioning, total number of vessels per field markedly increased in heparin mimetic peptide nanofiber treated rats at days 7, 9 and 14 (Figure 2.19). In addition to the quantification of vessel numbers, histological analysis showed that large vacuolar-like vessels were seen in the wound bed of GAG-PA/K-PA treated tissue sections (Figure 2.19A). Next, we tested whether heparin mimetic peptide nanofibers increase VEGF secretion to identify the mechanisms underlying the effects of these gels on promoting number of blood vessel formation.

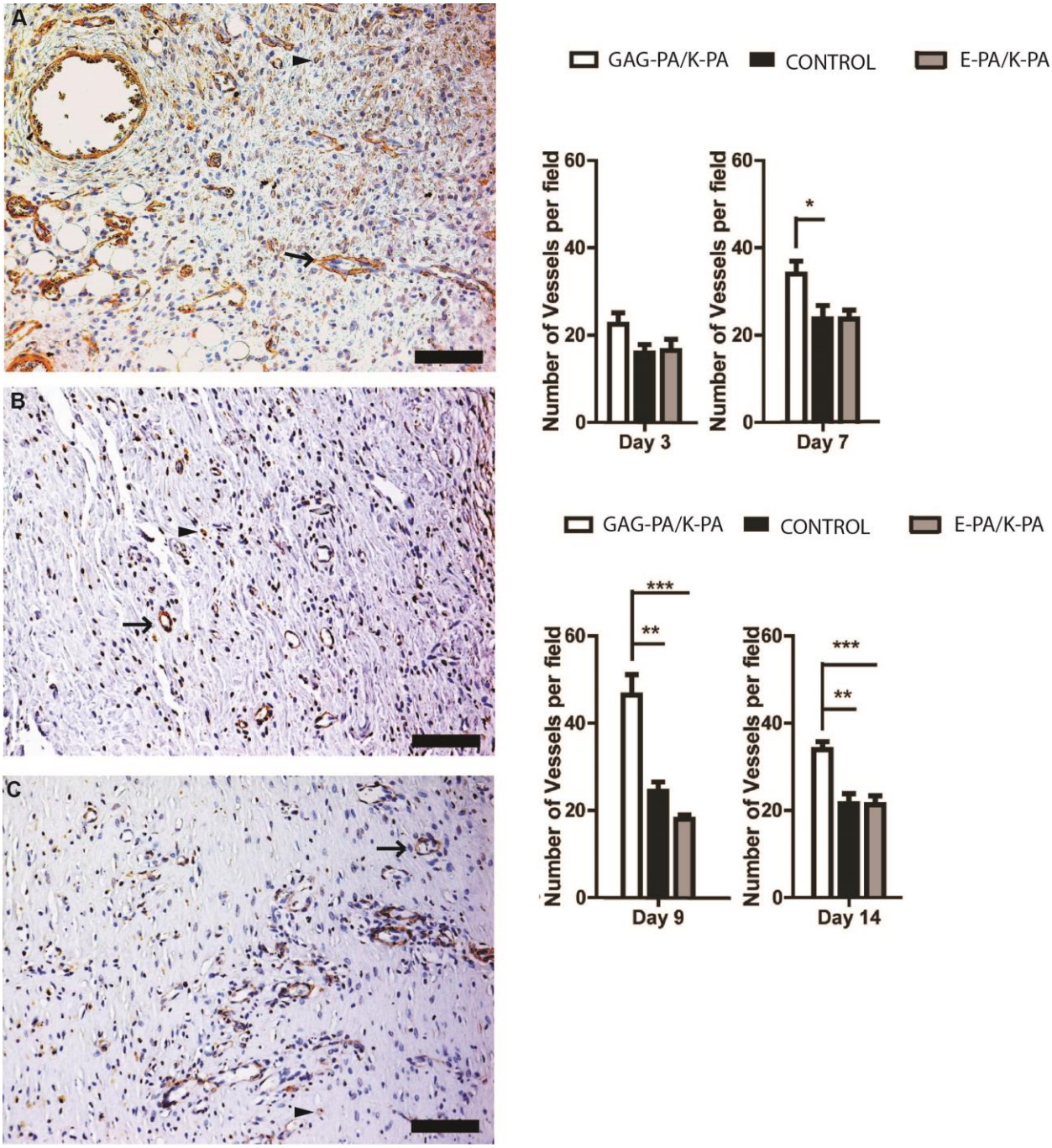

Figure 2.19 Accelerated blood vessel intensity in GAG-PA/K-PA treated wound area suggests that heparin mimetic peptide nanofiber treatment induced angiogenesis. Representative von Willebrand factor staining (brown) images of wounds treated with GAG-PA/K-PA (A), PBS (B) control and E-PA/K-PA (C) at day 9 and hematoxylin-blue

counterstaining of nuclei. Representative examples of large vessels (arrow) as well as capillaries (arrowheads) were showed (A, B, C). Quantitative analysis of number of vessels per field was performed from images. Data are presented as means ± SEM. *p<0.05, **p < 0.01, ***p<0.001, scale bars = 100 µm.

2.3.12. Heparin mimetic PA nanofibers promote angiogenesis via induction of VEGF expression

VEGF protein expression was quantified in diabetic skin wounds by western blot analysis at day 7 (early response) and day 14 (late response) to understand the basis of the enhanced angiogenesis in on GAG-PA/K-PA treated animals. No significant difference was found at VEGF protein level between groups on day 7 by western blot analysis (Figure 2.20). Higher expressions of VEGF were observed in GAG-PA/K-PA treated animals on day 14 compared to both E-PA/K-PA and PBS control animals (Figure 2.21). As such, it is likely that VEGF expression was stimulated at later days of recovery by the GAG-PA/K-PA system.

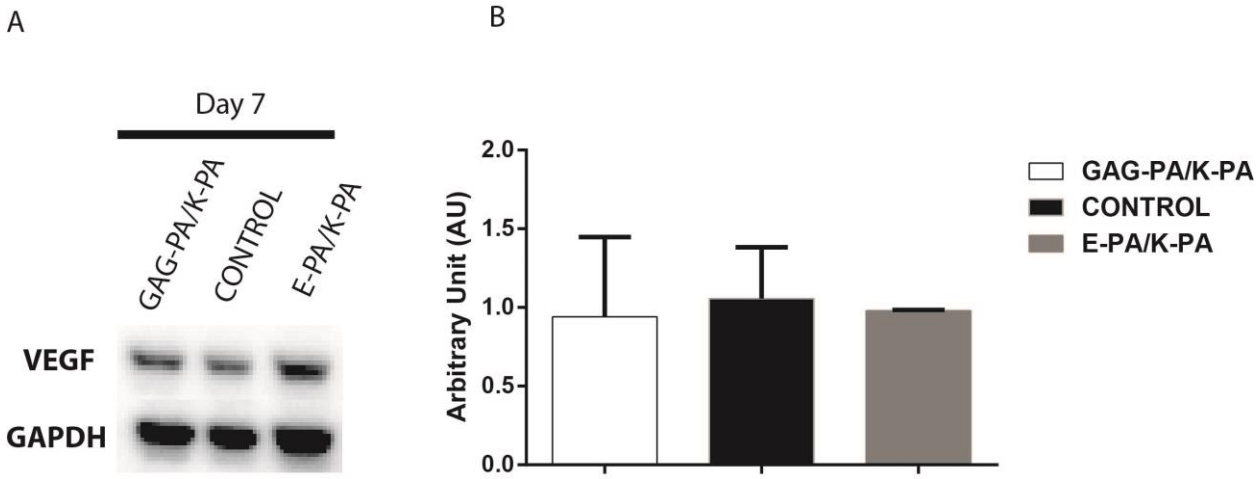

Figure 2.20 The representative western blot analysis and quantification of VEGF expression. Rats were treated with bioactive (white), non bioactive (black) and PBS control

(gray) and protein samples were collected on day 7. The density of the bands was evaluated by ImageJ and normalized to GAPDH signal. Data are presented as means ±SEM, n=3.

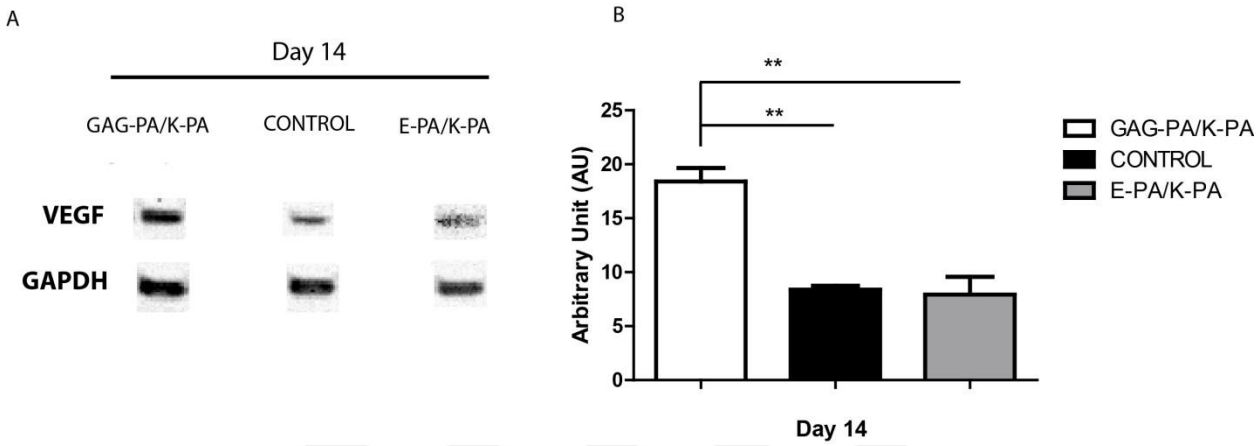

Figure 2.21 VEGF expression was enhanced in GAG-PA/K-PA treated animals, while lower expression was observed in control and non-bioactive PA treated samples on day 14. The density of the bands was evaluated by ImageJ and normalized to GAPDH signal. Western blot analysis showed that VEGF expression in GAG-PA/K-PA treated group was almost two folds higher than controls. Data are presented as means ± SEM. **$p < 0.01$.

2.3.13. Bioactive gel treatment affects infiltration of inflammatory cells

Characterization of inflammatory stage of wounds was performed by CD68 (monocyte/macrophage marker) staining (Figure 2.22). Quantitative analysis showed that number of macrophages was higher in both heparin mimetic GAG-PA/K-PA (92.6 ±6.8) and non-bioactive E-PA/K-PA (91.6 ± 8.2) peptide nanofiber treated groups in contrast to PBS treated control (46.7 ±14.5) animals on day 3 (Figure 2.22D). Although the number of macrophage was twofold higher than PBS control on early onset, no difference was found on day

7. Moreover, a gradual increase in monocyte/macrophage number was observed in GAG-PA/K-PA group on day 9.

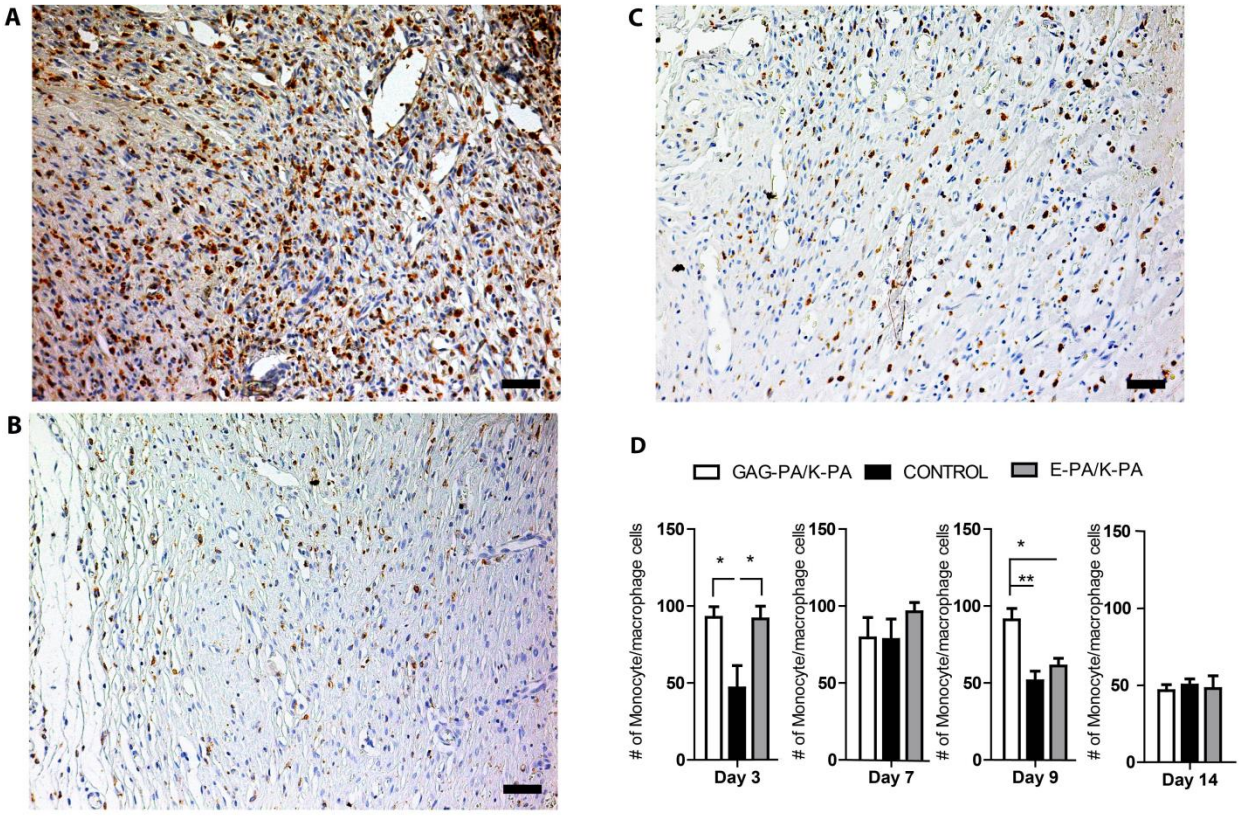

Figure 2.22 Monocyte/macrophage infiltration was increased in GAG-PA/K-PA treated wounds on day 9. CD68 immunostaining for bioactive gel (A), PBS control (B) and non-bioactive gel treated group (C). Brown color indicates presence of monocyte/macrophage and hematoxylin-blue counterstaining of nuclei. Quantitative analysis of number of monocyte/macrophage cells on days 3, 7, 9 and 14 post wounding (D). Data are presented as means ± SEM. *$p<0.05$, **$p < 0.01$, scale bars = 50 µm.

2.4. Discussion

Vascular complications that eventually lead to unhealed wound ulcers are characteristic of diabetes. Reduced expression of growth factors and impairment of angiogenesis are the main problems associated with diabetic foot ulcers. In this study, heparin mimetic peptide nanofibers were found to enhance wound healing rate by accelerating angiogenesis, promoting re-epithelialization process and stimulating the expression of VEGF. This finding correlates with studies that report that heparin-binding structures exhibit positive effects on wound healing [72, 73].

Animal wound healing models are important biological tools for understanding the cellular and molecular bases of tissue repair and play a vital role in the development and validation of potential strategies for clinical treatment. Their optimization is therefore important for the determination of the effectiveness of a prospective material or treatment method. While transgenic animals are ideal for the investigation of the diabetic wound healing process, there is an increasing amount of evidence that shows that STZ administration can create a suitable model of type I diabetes for wound healing studies [74-76]. In the present study, we have also implemented minor modifications to our experimental protocol to better accommodate the properties of the peptide amphiphile gels used. In particular, a preliminary study had shown that gels in uncovered wound areas may leak from the wound and mix with each other due to the movement of the animals; as such, potential gel mixing was prevented by coating the wounds with a non-woven, hypoallergenic, air-permeable elastic tape.

The main function of heparan sulfate proteoglycans (HSPGs) is their ability to modulate angiogenesis by binding to VEGF [77]. VEGF has an extracellular matrix (ECM)-binding domain and possesses binding affinity for HSPGs [78]. In our previous studies, we presented a

heparin mimetic peptide amphiphile (PA) nanofiber system that mimics the function of heparan sulfate by presenting optimal arrangement of functional groups (-COOH, -OH and -SO_3) on nanofibrous structures [79]. In these previous studies, we also showed that the presence of all of these functional groups within the same system is critical for growth factor binding, and that control peptides containing only one or two of these groups exhibit limited functionality compared to GAG-PA [79]. Furthermore, high binding affinity of peptide system to $VEGF_{165}$ rather than $VEGF_{121}$ (which lacks heparin-binding domain) showed that growth factor binding was site specific [80]. These studies also demonstrated that this nanofiber system showed better growth factor binding, enhanced induction of angiogenesis and neurogenesis than control PA nanofibers *in vitro* [81]. Our present findings showed that wound healing rate was accelerated in the GAG-PA/K-PA treated group compared to PBS control and non-bioactive peptide treated groups due to enhanced growth factor activity. As such, the increase in regenerative capacity is attributable to the amino acid sequence of the heparin mimetic group rather than the nanofibrous structures of the peptide amphiphile systems.

In diabetes, phases of wound healing process do not occur in synchrony, due to complications of the disease. We analyzed the progress in wound healing at different time points (days 3, 7, 9, and 14) along two weeks after treatment application. We found that gel treatment does not cause any difference on healing rate at the first stage of wound healing process (hemostasis), as the diabetic wounds began to release cytokines and growth factors for cell recruitment [82]. On the other hand, heparin mimetic hydrogel treatment enhanced wound healing at the inflammation and the proliferation phases.

CD68 staining was performed to observe monocyte/macrophage recruitment to the wound area and to investigate the extent of the immune response during the inflammation phase. The

presence of macrophage was required not only for efficient wound repair but also for induction of neovascularization [83, 84]. Reduced and abnormal vascularization was found in wounds of macrophage deficient mice [85, 86]. The nanofibrous structure of the scaffolds might be one factor that induces the early infiltration of monocyte/macrophage cells to the wound area, as both bioactive and non-bioactive PA treated wounds exhibited heightened inflammatory responses on day 3; however, this scaffold effect was temporary. On day 7, PBS treated rats had also similar number of monocyte/macrophage to gel treated rats. Inflammatory response was significantly higher in GAG-PA/K-PA treated group on day 9 correlated with enhanced neovascularization. In contrast, non-bioactive gel and PBS treated rats exhibited diminished expression of macrophages on day 9. In efficient wound healing process, wound macrophages disappear at the end of inflammatory phase [83]. The reduction of number of monocyte/macrophages in GAG-PA/K-PA treated group on day 14 indicated that macrophage infiltration ceased within wound area.

Keratinocyte migration and differentiation are inhibited in diabetic wounds [87]. Interaction of keratinocytes with fibroblasts is crucial for proper wound healing as these interactions induce the secretion of growth factors and cytokines [88]. The results presented here show that heparin mimetic hydrogel treatment recruits keratinocytes to leading edge and allows their persistent migration. The proliferation phase is also compromised in diabetic wounds [89]; however, re-epithelialization scoring and epithelial thickness analysis in this study indicate that tissue proliferation was promoted in heparin mimetic hydrogel treated wounds.

Myofibroblasts are specialized fibroblasts that play important roles in collagen synthesis and scar formation [90]. During wound healing, myofibroblasts develop from granulation tissue and transiently express α-SMA. Bioactive gel treatment was found to recruit cells to the myofibroblastic phenotype, which is essential for remodeling during the wound healing process.

It is notable that α-SMA expression was significantly higher in the heparin mimetic group on day 7 and 9. This result is also in correlation with the observed increase in granulation tissue formation. VEGF expression is known to induce myofibroblast transformation through the activation of TGF-β1. We have also observed a two-fold increase in VEGF expression in heparin mimetic PA treated animals compared to control. Thus, the significant myofibroblast presence and positive SMA staining in GAG-PA/K-PA treated wounds may be due to stronger VEGF expression in the wound area.

VEGF is essential for early blood vessel formation and angiogenesis. Wounds of STZ induced rats had diminished expression of VEGF compared to non-diabetic wounds [91]. Western blot analysis showed that VEGF expression was similar between samples on day 7, but increased in GAG-PA/K-PA treated wounds on day 14. During the wound healing process, VEGF expression was obtained from many cell types such as endothelial cells, fibroblasts, smooth muscle cells, platelets, neutrophils and macrophages. The presence of high number of those cells in the wound area contributes to VEGF secretion upon heparin mimetic gel treatment.

Increases in the number of newly formed vessels, together with high VEGF expression patterns, suggest that heparin mimetic gels are able to protect and stabilize the wound environment through modulation of angiogenesis. We also demonstrated that non-bioactive fibers had little to no influence on wound healing, except for an increase in early macrophage recruitment, which is a non-significant trend towards delayed recovery, suggesting that the effects observed in the GAG-PA/K-PA group were sequence-specific. Overall, heparin mimetic bioactive peptide nanofiber gels were found to be effective in increasing VEGF expression and promoting vessel formation in diabetic wounds.

2.5. Conclusion

In this study, we describe the application of a previously developed heparin mimetic peptide nanofiber system for the treatment of diabetic wounds. This bioinspired material promoted wound healing in the STZ-induced diabetic rat wound model. Results presented in this study showed that heparin mimetic peptide nanofiber treatment has a significant impact on the inflammation and proliferation phases of the healing process. The application of the bioactive gel formed by these peptide nanofibers to wound area promotes angiogenesis, re-epithelialization, and inflammatory response. In addition, cell recruitment was accelerated and macrophage infiltration was increased during the inflammatory phase in GAG-PA/K-PA treated rats. A marked increase of expression of VEGF and the number of blood vessels are strong evidences of the induction of angiogenesis in diabetic wounds. Overall, these results show that heparin mimetic peptide nanofibers present a promising therapeutic platform for the treatment of dermal wounds in diabetes patients.

2.6. Materials and Experimental Section

2.6.1. Materials

9-fluorenylmethoxycarbonyl (Fmoc) and tert-butoxycarbonyl (Boc) protected amino acids, [4-[a-(20,40-dimethoxyphenyl) Fmocaminomethyl]enoxy]acetamidonorleucyl-MBHA resin (Rink amide MBHA resin), Fmoc-Asp(OtBu)-Wang resin and 2-(1H-Benzotriazol-1-yl)-1,1,3,3-tetramethyluronium hexafluorophosphate (HBTU) were purchased from NovaBiochem and ABCR. Antibodies were purchased from Abcam and Millipore. Streptozocin (STZ) was purchased from Sigma Aldrich and biopsy punch from Microtek Medical (Zutphen, NL). Animals were anaesthetized with 2% Alfazyne (xylazine hydrochloride) and 10% Alfamine

(ketamine hydrochloride). All other chemicals and materials used in this study were analytical grade and obtained from Invitrogen, Fisher, Merck, Alfa Aesar, and Sigma-Aldrich.

2.6.2. Synthesis and characterization of peptide amphiphiles (PA)

Functionalized PA molecules were synthesized manually by standard solid phase Fmoc peptide synthesis chemistry (Figure 1.17). GAG-PA (C12-VVAG) and K-PA (C_{12}-VVAGK-NH2) were synthesized on Rink amide resin while E-PA (C_{12}-VVAGE) was synthesized on Wang resins. Amino acid couplings were performed with 2 equivalents of amino acids activated with 1.95 equivalents of HBTU, and 3 equivalents of DIEA for 1 equivalent of starting resin. Coupling time for each amino acid was 2 h. Lauric acid addition was performed similarly to amino acid coupling except that coupling time was 4 h. Fmoc removal was performed with 20% piperidine/dimethylformamide (DMF) solution for 20 min. 10% acetic anhydride/DMF solution was used to permanently acetylate the unreacted amine groups after each coupling step. DMF and dichloromethane (DCM) were used as washing solvents. Cleavage of protecting groups and peptide molecules from the resin was carried out by 95% trifluoroacetic acid (TFA) containing cleavage cocktail (95% TFA, 2.5% water, 2.5% triisopropylsilane) for 3 h. Excess TFA removal was carried out by rotary evaporation. PAs in the remaining solution were precipitated in ice-cold diethyl ether overnight. The precipitate was collected next day by centrifugation and dissolved in ultra-pure water. This solution was frozen at −80 °C for 4 h and then lyophilized for one week. Synthesis of PAs were characterized by Agilent 6530 quadrupole time of flight (Q-TOF) mass spectrometry with electrospray ionization (ESI) source equipped with reverse-phase analytical high performance liquid chromatography (HPLC) with Zorbax Extend-C18 2.1 × 50 mm column for basic conditions and Zorbax SB-C8 4.6 × 100 mm column for acidic conditions. An optimized gradient of 0.1% formic acid/water and 0.1% formic acid/acetonitrile for acidic

conditions and 0.1% ammonium hydroxide/water and 0.1% ammonium hydroxide/acetonitrile for basic conditions were used as mobile phase for analytical HPLC, respectively. A reverse-phase preparative-HPLC (Agilent 1200 series) system was employed for purification of GAG-PA by using Zorbax Extend-C18 21.2 × 150 mm columns. Residual TFA was removed from positively-charged K-PA by 0.1% HCl treatment. All lyophilized PA samples were reconstituted in 20 mM HEPES buffer at pH 7.4 for further use.

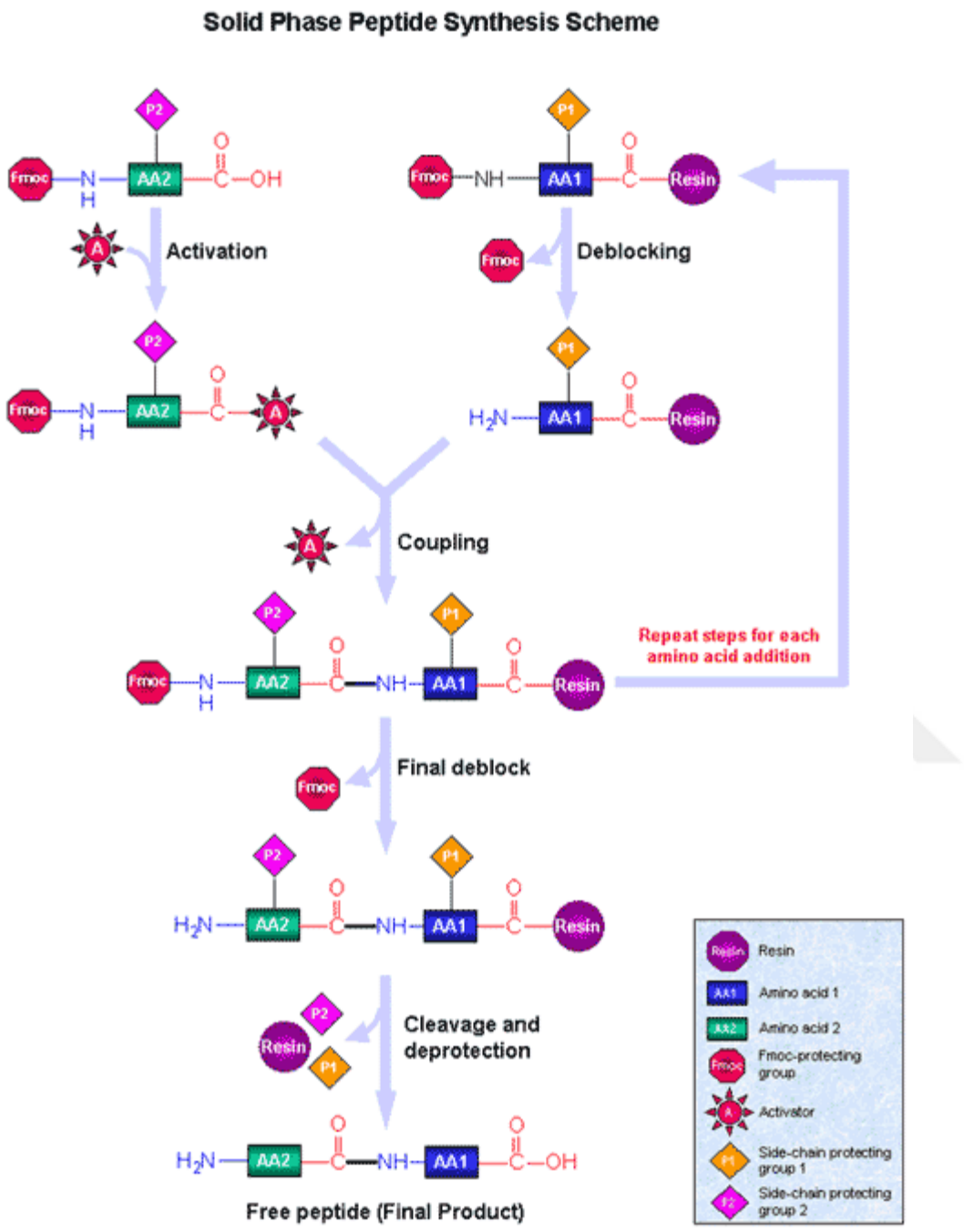

Figure 2.23 Synthesis route of a typical peptide peptide amphiphiles by using solid phase peptide synthesis. This synthesis relies on subsequent removal of a protecting group from the N-terminus for coupling with an activated ester. After the completion of coupling steps, resin linker and the side chain protections can be removed with TFA-containing cleavage cocktails.

2.6.3. Animal models

Male Sprague–Dawley (SD) rats (weight, 300 to 350 g; age, 12 to 14 weeks) were obtained from ADACELL Laboratory (Ankara, Turkey). Rats were exposed to a 12 h light-dark cycle and fed a standard laboratory diet with food and water provided *ad libitum*. The local Animal Experiments Committee approved all procedures and study design. Animals were fasted overnight and given an intraperitoneal injection of STZ (Sigma Aldrich, St. Louis, MO) at a dose of 45 mg/kg body weight in 0.1 mol/L sodium citrate buffer, pH 4.5 for the induction of diabetes. Blood glucose concentrations were monitored weekly by a GlucoDr Super Sensor Blood Glucose Test Meter (Korea) from tail vein blood. Animals that exhibited blood glucose levels over 20 mmol/L throughout the induction period were considered to be stably diabetic and used for wound healing experiments. Approximately 95% of animals were become stably hyperglycaemic after STZ injection.

2.6.4. Wound creation and treatment

3 weeks after STZ injection, 60 male Sprague Dawley (SD) rats were randomly divided into 3 groups for GAG-PA/K-PA treatment (n= 5 each for D0, D7, D9 and D14), PBS control treatment (n= 5 each for D0, D7, D9 and D14) and E-PA/K-PA treatment (n= 5 each for D0, D7, D9 and D14) (Figure 2D). Rats were anesthetized by intraperitoneal injection of xylazine hydrochloride (Alfazyne, 10 mg/kg) and ketamine hydrochloride (Alfamine, 25 mg/kg). Prior to creation of wounds, dorsal hairs of diabetic mice were completely shaved and the underlying skin was sterilized with povidone iodide. Three full-thickness wounds of 6 mm diameters were created on the dorsal skin using a biopsy skin punch for all treatment groups (Microtek Medical, Zutphen NL). Bioactive and non-bioactive gels were prepared immediately prior to their topical application. 1% (w/v) of gels or saline for 300 µl were applied directly onto each wound area and

covered with Octacare non-woven wound dressing (OCTAMED). This wound dressing was preferred due to its elastic, air permeable, sterile, non-allergenic, long-term powerful adhesion and absorbent band properties that can be easily removed from wound. The optimization studies showed that re-application of gel on day 2 accelerated wound healing in diabetic rats. Therefore, gels (and PBS) were re-applied and the wounds were re-dressed two days post-wounding. Thereafter, the animals were individually caged. At each experimental end point (day 0, 3, 7, 9 and 14), animals were sacrificed and their tissues were extracted for subsequent analyses. Body weights were measured using an electronic balance on the day of wounding (day 0), as well as on days 3, 7, 9, 12 and 14 post wounding.

2.6.5. Measurement of Wound Area

Wound margins were traced on days 3, 7, 9 and 14 post wounding by using transparent papers. The wound tracing was performed only on euthanized rats. The boundary of wound lines was traced from edge of the healthy epithelium. Wound area was traced on the graph paper and calculated with ImageJ.

2.6.6. Sectioning and staining

On days 3, 7, 9 and 14, diabetic rats were sacrificed and their skin tissues were fixed with 10% formalin and embedded in paraffin. Tissue sections (5 μm) were deparaffinized in xylene, rehydrated through graded alcohols to distilled water, and stained with hematoxylin and eosin (H&E). Collagen formation was evaluated by Masson's trichrome staining. For this purpose, sections were initially deparaffinized, rehydrated, placed in Weigert's hematoxylin, and rinsed under tap water for 10 min. Sections were then immersed into phosphomolybdic acid, aniline blue, acetic acid and ethanol in the order provided.

2.6.7. Histological quantifications

All quantifications associated with H&E staining were performed using ImageJ. Images of H&E stained tissue sections were taken with 50 X magnifications by an up-right microscope (Zeiss Axio Scope A1) and visually inspected for epithelialization scoring (0 absent, 1 weak, 2 moderate, 3 complete reepithelialization of the wound). Scoring was performed by three researchers who were blind to the study design. The thickest distance between the top and the bottom of the epithelium was measured for the quantification of epithelial thickness. Additionally, the distance between epithelial tips were calculated from images via measurement of length of gap between ends of epithelial tissue. The epithelial distance measurement was performed at day 3, 7 and 9 with ImageJ tool. On day 14, re-epithelialization was complete for most of the samples; as such, distance was not calculated for this day. The whole granulation tissue area was traced and measured with ImageJ. Monocyte/macrophage staining images were taken with 100x magnification by up-right microscope.

2.6.8. Immunohistochemical Staining

Tissue sections were deparaffinized and hydrated in graded ethanol solutions and distilled water. Endogenous peroxidase was inactivated with 3% hydrogen peroxide for 10 min at room temperature. Nonspecific binding sites were blocked with 10% normal goat serum for 2 h at room temperature. Antigens were then detected by indirect binding with primary antibodies and HRP-conjugated secondary antibodies. Serial sections were immunolabeled with anti-von Willebrand factor antibody (1:400 dilution; ab6994, Abcam), alpha smooth actin antibody (1:500 dilution; ab76549, Abcam) or CD68 antibody (1:200 dilution; ab31630, Abcam) to evaluate the degree of healing in wound tissues. Sections were developed in 3,3’-diaminobenzidine (DAB) and counterstained with hematoxylin.

The number of blood vessels was counted from at least 6 randomly selected fields in each section; sections were immunolabeled with anti-von Willebrand Factor (vWF) antibody and quantified by two independent observers under 200x magnification. Quantifications were performed with positive staining of vWF staining +lumen formation. ImageJ analysis system was used to calculate the number of vessels in each field.

2.6.9. SEM characterization of peptide amphiphiles molecules

Scanning electron microscopy (SEM) samples were prepared by incubating 1 wt% of GAG-PA/K-PA or E-PA/K-PA gels for 20 min on silicon wafer. Samples were then dehydrated by immersion into increasing concentrations of ethanol, dried in a critical point drier (Tousimis, Autosamdri-815B) and coated with 6 nm Au-Pd layer prior to analysis.

2.6.10. Circular dichroism (CD) analysis

Circular dichroism (CD) experiments were performed using a J-815 Jasco spectrophotometer. 3.6×10^{-4} M aqueous solutions were diluted from 1 mM stock peptide solutions for CD spectroscopy. Measurements were acquired at room temperature with 500 nm/min scanning speed, 1 nm bandwidth and 0.1 nm data pitch within the data interval of 300 to 190 nm. Three consecutive measurements were averaged for each sample. The results were converted to and represented as molar ellipticity.

2.6.11. Oscillatory Rheology

Oscillatory rheology measurements were performed with an Anton Paar Physica RM301 rheometer operating with a 25 mm parallel plate configuration at 21 °C. 1 wt % of GAG-PA/K-PA or E-PA/K-PA with total volume of 300 µL was loaded on the center of the lower plate. The upper plate was brought to 0.5 mm gap position and the gel was incubated for 10 min before

measurement. Storage moduli (G') and loss moduli (G") values were scanned at an angular frequency of 100 to 0.1 rad/s, with 0.5% shear strain. Three repeats were performed for each gel.

2.6.12. RNA Isolation

RNA and protein samples were isolated from skin tissue via TRIzol® Reagent (Ambion). Homogenization was performed after dissection of wound samples. After homogenization of tissues in Trizol, 1/5 v/v chloroform was added into sample. They were kept for 2-3 min at room temperature. Then they were centrifuged for 17 min with 15000 rpm at 4 °C. The resulting aqueous upper phase (clear) containing the RNA was transferred into a fresh microtube; interphase and the lower phase containing the proteins were stored at -20 °C for protein isolation. Isopropanol (1/2 v/v) was added to the RNA containing phase and mix 15 times (up-down). Solution was incubated at -20 °C over night or 20 min. The probes were centrifuged for 12 min with 15000 rpm at 4 °C and subsequently the supernatant was discarded. The pellets were washed twice with 70% ethanol by vortexing and centrifugation (12000 rpm, 10 min, 4 °C). Ethanol was totally removed from samples and pellet was solved in 20 µL of RNAse free water. Finally the RNA probes were stored at -20 °C.

2.6.12.1. Quantification of RNA

RNA concentration was measured by Nanodrop that is based on a cuvette free spectrophotometric technique. It enables us to determine concentration by pipetting 1 µL of samples with high accuracy. Before making a sample measurement, a blank must be measured. 2 µL of water was used for blank. After blank measurement, samples were pipetteD onto lower measurement pedestal and arm was closed. After each measurement, arm must be cleaned by using a soft laboratory wipe. In order to assess purity of RNA, the absorption ratio between 260/280 and 260/230 of sample were checked. For the 260/280 ratio values betwen 1.8 - 2.0

were accepted as pure RNA. For 260/230, it should be in range of 1.8 - 2.2. Since lower ratios indicate contaminations, only pure RNA was used for further analyses.

2.6.13. Protein Analysis

2.6.13.1. Protein Isolation

All proteins were isolated from skin tissue via TRIzol® Reagent (Ambion). The stored micro tubes (at -20 °C) containing the protein phases were defrosted and treated with 120 µL absolute ethanol absolute. After incubation at room temperature for 2-3 min the probes were centrifuged at 2000 rcf for 5 min at 4 °C to precipitate the DNA. The supernatant containing the proteins was transferred into fresh microtubes, followed by precipitation by means of adding 600 µL isopropanol to the probes and incubation at room temperature for 10 min. After centrifugation at 12000 rcf for 10 min at 4 °C the supernatant of each probe was discarded and the pellet was subsequently washed three times with 0.3 M guanidine hydrochloride in 95% ethanol. Therefore the probes were incubated with 800 µL of the washing buffer at room temperature for 20 min and afterwards centrifuged at 7600 rcf for 5 min at 4°C. After the third washing step this procedure was repeated once with 95% ethanol which was then completely removed from the pellets. Then the pellets were solved in 150 µL of 1% SDS containing protease inhibitors (1:1000) by incubating the probes over night at 50 °C. On the next day, insoluble components were removed by centrifugation with 10000 rcf for 10 min at 4°C. Eventually, the supernatants were transferred into fresh micro tubes and stored at -20°C.

2.6.13.2 Quantification of isolated proteins by BCA assay

The protein samples were quantified using BCA assay which is based on bicinchoninic acid for colorimetric detection. BCA assay standards, a series of dilutions of known concentration (2000-0 µg/µL) are prepared from bovine serum albumin (BSA). Unknown concentrations of samples

are determined from standard curve. 25 µL of each sample was pipette on microplate. Developing solution was prepared from BCA protein assay kit, for 200 µL; 196 µL BCA reagent A + 4 µL BCA reagent B were mixed. After adding the developing solution to each probe, plate was incubated at 37 °C for 30 min. A longer incubation might increases the sensitivity of the assay but incubation must be stopped before color becoming too dark to avoid unlinear reaction. Absorbance was measured at 560 nm by microplate reader and concentration of the proteins was calculated by BSA standard curve.

2.6.13.3. SDS PAGE

SDS-PAGE is a technique that separates molecules according to molecular weight. Two acrylamide gels are prepared for SDS-PAGE system. Upper gel (stacking gel) concentrate or "stack" the protein samples into a very narrow zone prior to separation. Separating (or resolving) gel is responsible for separating proteins by size. Protein separation by SDS-PAGE is used not only for estimation of molecular mass, but also to determine purity of protein samples and western blot analyses.

For SDS-Page, 15% resolving and 5% stacking gels were used.

Components	15 % Resolving Gel	5 % Stacking Gel
dH_2O	1.1 mL	1.4 mL
Acrylamide / Bis (37:1)	2.5 mL	0.33 mL
Tris/HCl, 1 M, pH 6,8	-	0.25 ml
Tris/HCl, 1,5 M, pH 8,8	1.3 mL	-

10 % SDS	0.05 mL	0.02 mL
10 % APS	0.05 mL	0.02 mL
TEMED	0.002 mL	0.002 mL

Table 2.2 Components of resolving and stacking gel for SDS PAGE.

For preparation of 5 mL of 15% resolving gel, 1.1 mL of dH_2O, 2.5 mL of acrylamide, 1.3 mL of 1 M Tris/HCl (pH 8.8), 0.05 mL of 10% SDS, 0.05 mL of 10%APS and 0.002 mL TEMED were mixed. After adding TEMED and APS gel will be polymerized fairly quickly, therefore they were added at last step. While pouring the resolving gel, some space (around 2 cm) for stacking gel was left. Isopropanol was added for removing bubbles at top of the gel and to avoid dry up the gel. Resolving gel was incubated at RT for about 20 min for polymerization. 5% stacking gel was prepared according to table (see above) and poured on top of the resolving gel. A comb was inserted into stacking gel followed by incubation for 20 min at RT. Before loading 30 µL of protein samples were mixed with 4X loading dye and boiled at 100 ºC for 5 min. Chamber was filled with electrode buffer and wells were washed with syringe. Gels were loaded with 37, 5 µL of protein probes and 5 µL of a pre-stained protein ladder. Proteins were separated at 20 mA for 80 min.

2.6.13.4. Protein Transfer onto a PVDF Membrane

After electrophoresis, the separated molecules were transferred or blotted onto polyvinylidene difluoride (PVDF) membrane. In SDS-PAGE system, glass plate was opened and stacking gel was removed. Resolving gel was equilibrated in 1X transfer buffer. For electrophoretic transfer

of proteins semidry electroblot system ("Semi-Dry Electrophoretic Transfer Cell) was used. Whatman papers were equilibrated in Anode I, Anode II and Cathode buffers as seen in Figure. PVDF membrane was equilibrated for 15 min in methanol, 2 min in water and 5 min in Anode II buffer, respectively. By sandwich method, two whatman papers and gel were placed on blotting membrane with three whatman papers. Air bubbles were removed by rolling with 15 mL falcon tubes. Finally the blot was soaked with 1x transfer buffer and the upper plate of the transfer cell (cathode) was fixed. Protein transfer was performed at 14 V for 30 min for one gel. When an electric field was applied, the proteins moved out of the polyacrylamide gel onto the surface of the PVDF membrane.

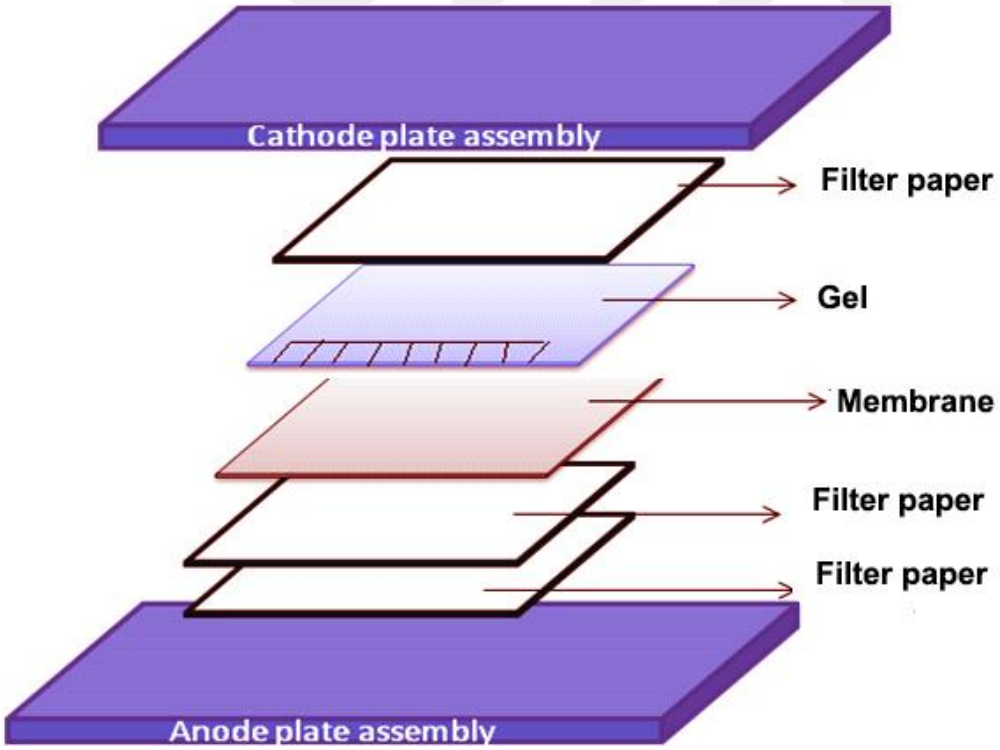

Figure 2.24 Semi-dry blotting of proteins. First filter paper close to anode is washed with anode buffer I. Second paper washed with Anode II. Membrane is activated in methanol for 15 min and washed with Anode buffer II. Acrylamide gel is washed with Anode II buffer and

carefully placed on filter papers. Last filter paper close to cathode plate was washed with cathode buffer.

Transfer Buffers	**Components**
Anode I Buffer	0,3 M Tris-HCl (pH 10,4), 10% MeOH
Anode II Buffer	25 mM Tris-HCl (pH 10,4), 10% MeOH
Cathode Buffer	25 mM Tris-HCl (pH 9,4), 10% MeOH, 40 mM Glycine

Table 2.3 Transfer buffer and components used in semi dry blotting.

2.6.13.5. Antibody Incubation

	Name	**Company**	**Concentration**
Primary Antibody	Alpha-SMA	Millipore 04-1094	1:20000
Primary Antibody	VEGF	Millipore ABS82	1:2000
Secondary Antibody	Anti-rb IgG-HRP	Millipore Ab6721	1:2000
Secondary Antibody	Anti-m IgG-HRP	Millipore 12-349	1:1000
Housekeeping	GAPDH	MAB374	1:2000

Table 2.4 Company information and working concentration of antibodies.

After blotting, the membrane was transferred into a dish and was incubated with blocking solution (5% low fat milk in TBS-T) for 1 h in order to prevent nonspecific binding of antibodies. Primary antibodies were diluted (1:100) in 5% BSA in TBS-T. Membrane was incubated with primary antibodies overnight at 4 ºC on a shaker. Next day, membrane was washed three times for 10 min with TBS-T. Then, the secondary antibody linked to the enzyme

horseradish peroxidase (HRP) was diluted 1:2000 in 5% BSA in TBS-T. Membrane was incubated with secondary antibodies for 1 h and washed three times with TBS-T for 10 min.

For loading control, the membrane was additionally hybridized with anti-GAPDH antibodies. Membrane was washed three times with TBS-T for 5 min, and incubated in blocking solution for 30 min at RT. Membrane was incubated with antibody against GAPDH for 30 min. Since anti-GAPDH antibodies were directly coupled to the HRP, a secondary antibody was unnecessary. After washing of membranes three times with TBS-T for 5 min, development was performed as described above.

TBS (pH 7.4)	**10x**
Tris	30 g
NaCl	80 g
KCl	2 g
dH_2O	Up to 1 L

Table 2.5 Preparation of TBS solution.

TBS-T	**1x**
Tween 20	0.05%
TBS	Up to 1 L

Table 2.6 Preparation of TBS-T solution.

2.6.13.6. Visualizing antibody-antigen complexes

For visualization of antibodies, membrane was placed in transparent foil. 400 µL of "Luminol Reagent" and 400 µL of "Peroxide Solution" were mixed and homogenously applied onto the membrane. After incubation for 5 min at room temperature, membrane was placed in an imaging

system with a CCD camera for chemiluminescence detection. For quantification ImageJ software was used. Signals of the gene of interest were normalized to GAPDH signal and expressed as x-fold in comparison to control sample.

2.6.13.7. Coomassie staining

To confirm that proteins on the membrane were not degraded and were transferred properly onto the membrane, Coomassie blue staining was performed. Coomassie blue binds nonspecifically to virtually all proteins on membrane. For this, membranes were incubated with "Coomassie staining solution" for 45 min on shaker at RT. After staining, membrane was washed with "destaining solution" for 10 min to remove excess dye and left to dry at RT.

Commassie Staining Components	**Volume**
Isopropanol	250 mL
Acetic acid	100 mL
Coomassie brilliant blue	2.5 mL
dH_2O	Up to 1 L

Table 2.7 Preparation of Coomassie blue solution for protein staining.

2.6.14. Statistical Analysis

Statistical analyses were performed using GraphPad Prism 5. One-way and two-way ANOVA was used to compare the differences between the groups and Dunn's multiple comparison test was used for post-hoc correction. Error bars indicate the standard error of the mean.

Chapter 3

Diabetic Wound Healing in db/db mice with Angiogenesis-promoting, Glycosaminoglycan-mimetic Peptide Nanofibers

3.1. Objective

Impaired neovascularization and abnormal inflammatory responses are fundamental characteristics of diabetic wounds and contribute to delayed wound healing processes. Biomaterials capable of presenting extracellular matrix-mimetic signals may assist in the recovery of diabetic wounds by modulating the immune system and creating a more conductive environment for blood vessel formation. The present study investigates the effect of a GAG-mimetic peptide amphiphile (PA) nanofiber gel on the healing of diabetic wounds, with emphasis on the ability of the PA nanofiber network to regulate the expression of inflammatory cytokines. We demonstrate that GAG-mimetic peptide nanofibers are able to increase the rate of closure in diabetic wounds, can support tissue neovascularization, enhance the deposition of collagen and expression of alpha-smooth muscle actin (α-SMA), and eliminate the sustained presence of interleukin-6 (IL-6) and tumor necrosis factor-alpha (TNF-α) in the diabetic wound site. As the overexpression of pro-inflammatory markers is a hallmark of diabetes and interferes with wound recovery by preventing the healing process to proceed beyond the inflammatory phase, the GAG-mimetic peptide nanofibers accelerate diabetic wound healing by modulating the local immune response.

3.2. Introduction

3.2.1. Db/db Transgenic Mouse Model of Type-II Diabetes

The most common transgenic mouse models of type II diabetes are obese models, which are mainly db/db and ob/ob mice. Ob/ob has a deficiency in leptin, whereas db/db has a deficiency in the leptin receptor. Abnormal mRNA splicing occurs due to a single autosomal recessive mutation on chromosome four (leptin) in db/db mice and leads to leptin receptor deficiency [9]. The db/db mouse exhibits hyperglycemia within 4-8 weeks of age and develops obesity by 3 to 4 weeks. β-cell failure is observed following hyperinsulinemia.

Although, chemical injections (e.g. STZ) are the simplest way of induction for diabetes, they can also be toxic for other organs such as the kidney and liver. One of the similarities between human and diabetic mice is that diabetic properties of mouse models also depend on genetic background and age. In this study, the BKS.Cg-+ *Leprdb*/+ *Leprdb*/OlaHsd strain was used and db/db mice were purchased from Envigo Laboratories, USA, IN. Impaired cellular immunity, increased level of pro-inflammatory cytokines, and diminished cytokine release are the main immunological characteristics of db/db mice [92]. Additional characteristics of those mice are; infertility, diminished growth factor release, decreased levels of insulin-like growth factor-1 and increased minor glycosylated hemoglobin [92]. One of the disadvantages of db/db mice is a short life span; which makes it difficult to study the long term effects of type II diabetes in those animals [93]. However, it has been established that renal and microvascular complications can be investigated by using db/db mice [94, 95].

3.2.2. Effects of pro-inflammatory cytokines on wound healing

The initial inflammatory response is critical to facilitate complete wound closure. Interleukin (IL)-6, IL-1β, and tissue necrosis factor-alpha (TNF-α), are key mediators of inflammatory processes. Expressions of TNF- α and IL-1 are increased upon injury, infections or the release of proteolytic enzymes which may cause severe tissue damage. The main function of pro-inflammatory cytokines is to recruit inflammatory cells to the wound area and facilitate cytokine production. Mice deficient in the TNF receptor TNF-Rp55 had a decreased inflammatory response but still promoted wound closure [96]. It had been shown that mIGF-1 expression can significantly down-regulate proinflammatory cytokines, such as TNF- α and IL-1β, and regulate the expression of CC chemokines to recruit monocytes/macrophages [97].

Although the long term presence of pro-inflammatory cytokines is detrimental, complete elimination of it is unable to improve wound healing. Studies with IL-6 knockout mice showed delayed re-epithelialization and defects in granulation tissue formation [98].

3.3. Results

3.3.1. Synthesis of self-assembled GAG-mimetic peptide nanofibers

Lauryl-VVAGEGDK(pbs)S-Am (GAG-PA) and Lauryl-VVAGK-Am (K-PA) molecules were synthesized by Fmoc solid-phase peptide synthesis (Figure 3.2). As shown in the chemical structure of peptide amphiphiles molecules, they carry a hydrophobic alkyl tail, β-sheet forming sequences and bioactive epitope group (Figure 3.1). The GAG-PA molecule bears a strong negative charge (-3) due to its glutamate, aspartate and *p*-sulfobenzoic acid-modified lysine residues. On the other hand, K-PA carries a positive charge of +1, which is localized on the protonated amino group of the lysine residue and allows the molecule to serve as a charge-screening entity for the self-assembly of GAG-PA/K-PA.

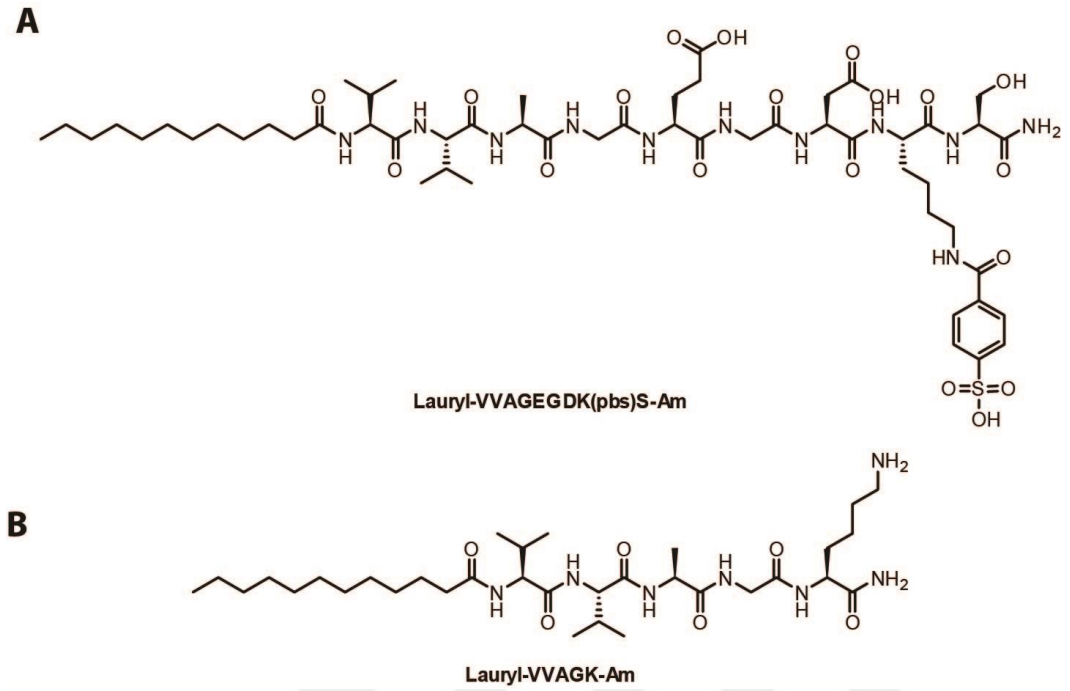

Figure 3.1 Chemical view of negatively charged GAG-PA and positively charged K-PA. PAs have three regions; hydrophobic tail (lauric acid), β-sheet forming amino acids (VVAG) and peptide epitopes.

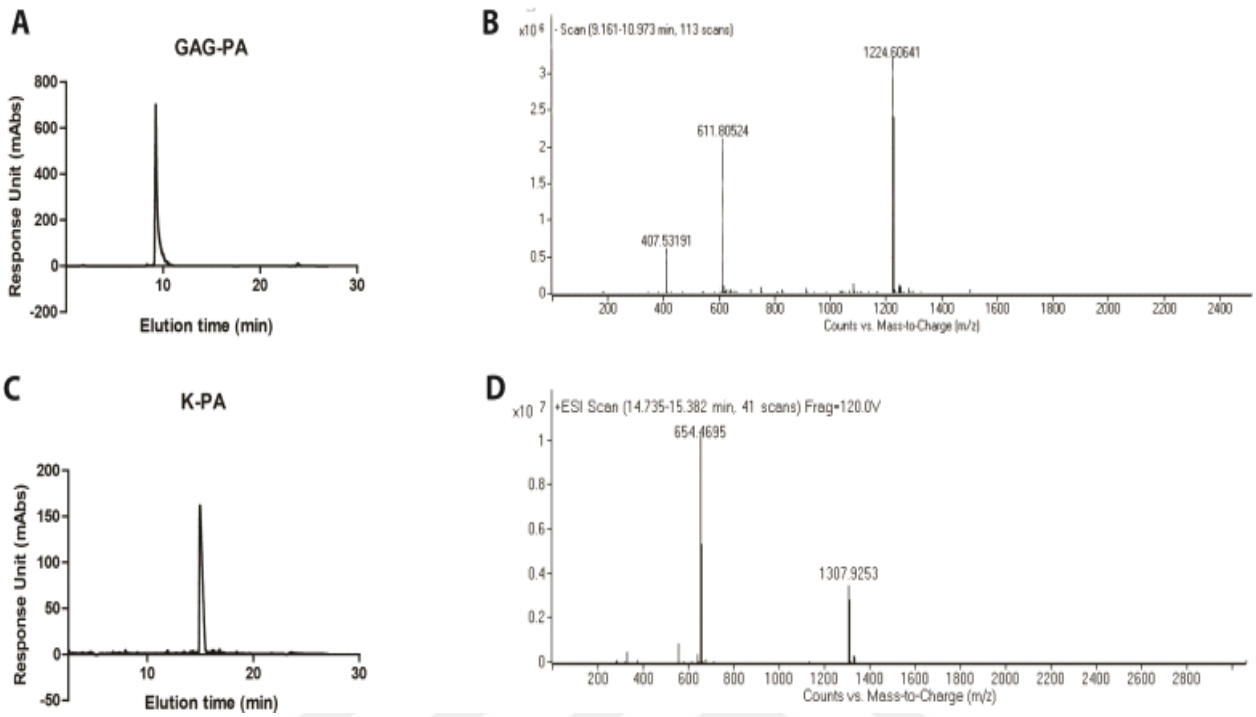

Figure 3.2 Liquid Chromatography and mass spectroscopy (LC-MS) of PA molecules used. HPLC chromatogram of purified GAG-PA (A) and K-PA (C) molecule at 220 nm. Mass spectra of peptides; for GAG-PA $[M-H]^-$ (calculated) = 1224.80, $[M-H]^-$ (observed) = 1224.60, $[M/2-H]^-$ (calculated) = 611.80, $[M/2-H]^-$ (observed) = 611.80, $[M/3-H]^-$ (calculated) = 407.53, $[M/3-H]^-$ (observed) = 407.53 (B), for K-PA $[M+H]^+$ (calculated) = 653.89, $[M+H]^+$ (observed) = 654.46, $[2M+H]^+$ (calculated) = 1308.76, $[2M+H]^+$ (observed) = 1307.92 (D).

3.3.2. SEM and TEM analysis

GAG-PA/K-PA scaffolds were characterized with SEM, and TEM analysis. Structural properties of the PA nanofiber system were characterized with SEM (Figure 3.3A) and TEM imaging (Figure 3.3B). The three-dimensional nanofibrous structure of PA nanofibers was found to be quite similar to the natural ECM [10]. TEM images of these mixtures demonstrated that

nanofiber structures were formed following the mixing of two oppositely charged peptides amphiphiles, with average diameters of 10-20 nm, and lengths up to several micrometers.

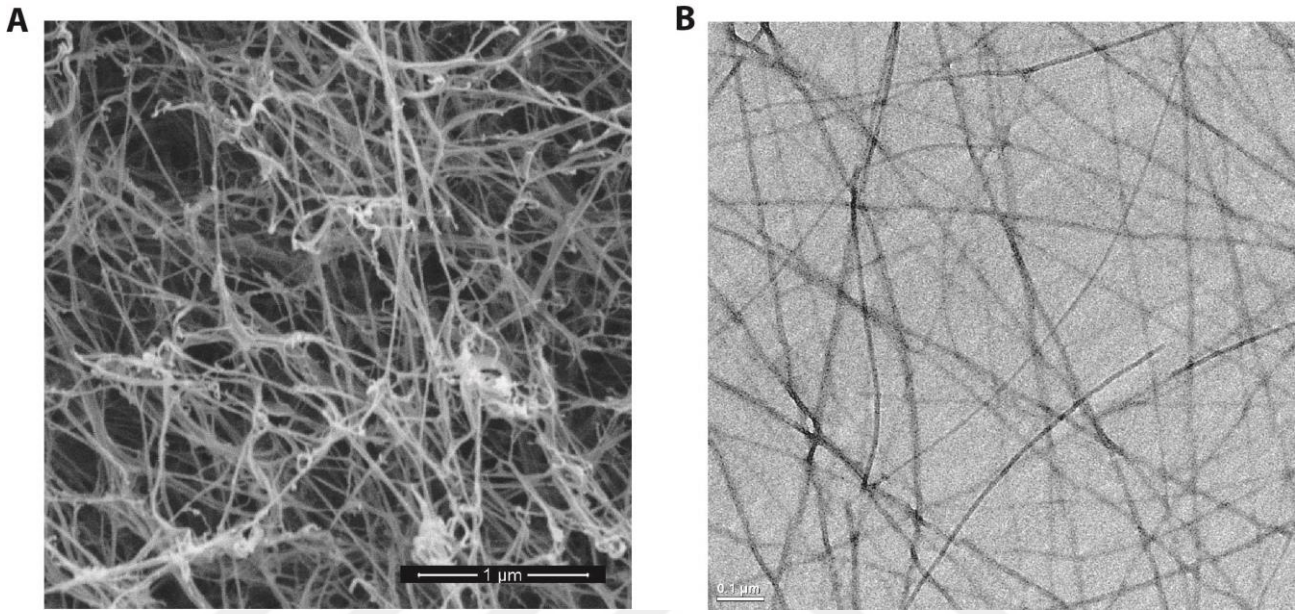

Figure 3.3 SEM and TEM images of GAG-PA/K-PA show peptide nanofiber networks. Scale bars are 1 µm in SEM and 0.1 µm in TEM images.

3.3.3. CD analysis of PAs

Circular dichroism (CD) spectroscopy analysis of PAs showed that co-assembled systems were oriented in a β-sheet conformation, presenting a negative peak signal at 220 nm and positive peak at 202 nm (Figure 3.4). While the GAG-PA/K-PA mixture had a β-sheet structure, the individual peptides exhibit a combination of weak β-sheets and random coils due to charge repulsion between individual peptide units.

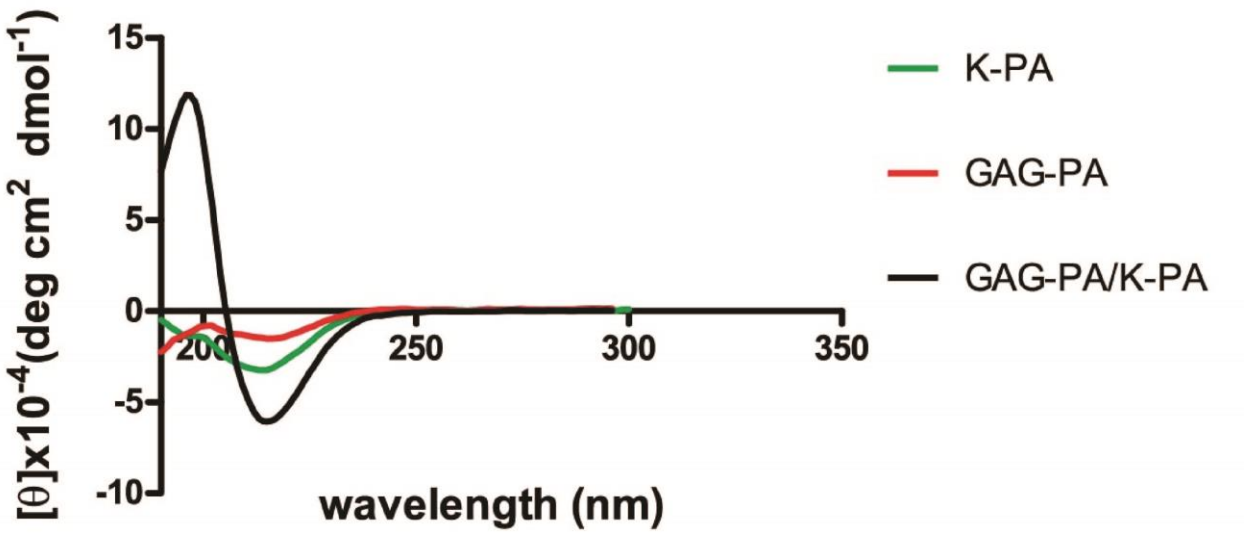

Figure 3.4 Characterization of peptide amphiphiles by circular dichroism. CD analysis showed that GAG-PA/K-PA contain β-sheet secondary structure.

3.3.4. Physical characteristics of the PA

Physical characteristics of the PA assembly matrix are critical for the material to remain at the wound site throughout the recovery period and support cell growth while allowing for cellular migration and recruitment. Mechanical properties of the matrix were investigated with oscillatory rheology. Storage (G′) and loss (G″) moduli were scanned from 100 to 0.1 rad/s of angular frequency and with a constant shear strain. The GAG-PA/K-PA mixture was found to have a higher storage modulus (G') than loss modulus (G"), suggesting that the peptide nanofibers form hydrogels at pH 7.4 (Figure 3.6). Storage moduli results show that the stiffness of the gels was around 7.5 kPa. The viscoelastic behaviors observed in PA scaffolds are favorable, as they facilitate its biodegradability by metalloproteinases in a manner similar to ECM remodeling.

Figure 3.5 Mixing of positively and negatively charged PAs resulted in the formation of gels at pH 7.4.

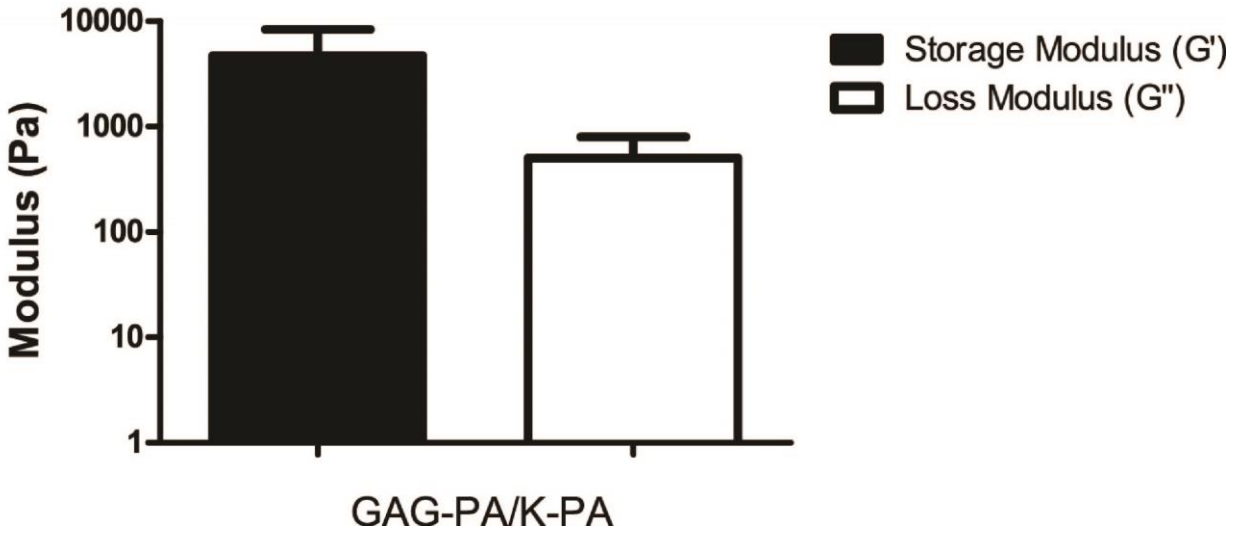

Figure 3.6 Oscillatory rheology analysis of GAG-mimetic peptide nanofibers. Oscillatory rheology measurement was performed for investigation of physical characteristics of the PA assembly. Storage modulus is higher than loss modulus also indicated gel characteristic of GAG-PA/K-PA nanofibers.

3.3.5. GAG-PA/K-PA treatment accelerates wound closure

Full-thickness wounds were created by 6-mm diameter biopsy punches and found to be consistent in size (Figure 3.7B). We analyzed the healing progress of diabetic wounds at different time points throughout 21 days of GAG-PA/K-PA treatment. Representative pictures of wounds from diabetic animals indicated that control animals carry scabs even after 21 days of recovery, while bioactive gel treated animals exhibited completely re-epithelialized wounds on day 21 (Figure 3.7A). Wound area quantifications showed that GAG-PA/K-PA treated mice showed significantly smaller wounds compared to the PBS control group on day 7, 14 and 21. Wound size was around 44.1% on day 21 in the bioactive gel treated group, while it was 58.4% in control. As such, the wound closure was not complete after 21 days even for the GAG-PA/K-PA treated group, but the wound sizes were significantly smaller than the control group.

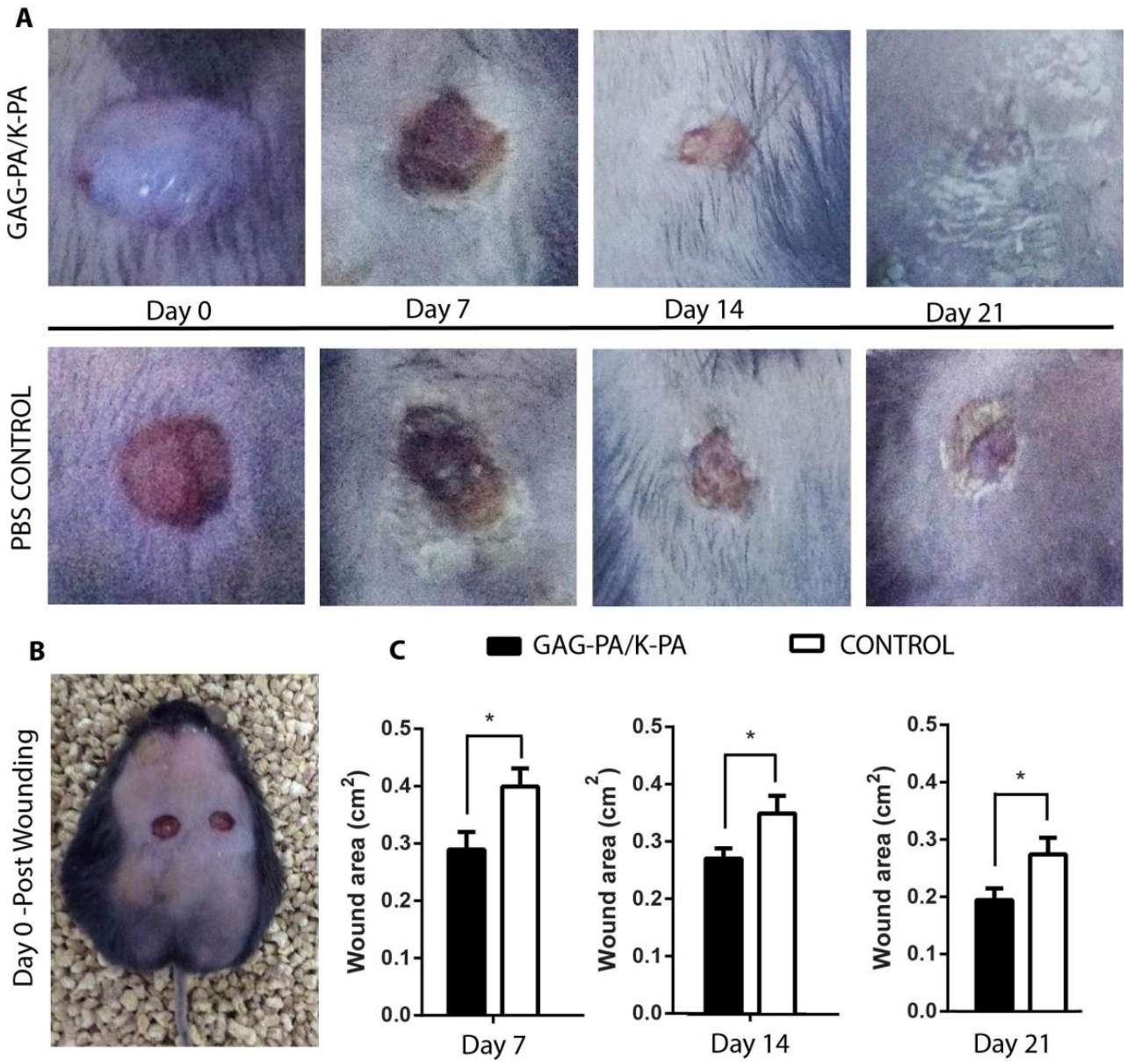

Figure 3.7 Bioactive GAG-mimetic peptide nanofiber treatment accelerates the recovery of diabetic wounds. Two wounds were created by biopsy punch at the dorsal skin of db/db mice on day 0, representative pictures illustrate the closure of wounds in GAG-PA/K-PA and PBS treated animals on days 0, 7, 14 and 21 (A, B). Skin wounds of animals treated with GAG-PA/K-PA nanofibers close faster than control animals, exhibiting smaller average wound areas at days 7, 14 and 21 (C). Values are expressed as mean ±SEM, (n=6), *$p < 0.5$.

3.3.6. Effects of GAG-mimetic gel treatment on tissue remodeling

H&E staining was performed on mouse skin sections to further investigate the changes that occur during the epithelialization, granulation tissue formation and tissue remodeling phases (Figure 3.8). Morphological changes on diabetic wounds, such as crust formation (C), replacement of the wound matrix (M) and granulation tissue (G) formation was observed on days 7 and 14 in both groups (Figure 3.8). H&E stained sections were analyzed to quantify granulation tissue formation and re-epithelialization in a single-blinded manner. Histological analysis of healing wounds in db/db diabetic mice showed faster keratinocyte proliferation and migration following GAG-PA/K-PA treatment compared to control. Calculation of granulation area per total wound area indicated that the formation of granulation tissue is faster in the bioactive group on day 7; however, granulation tissue formation rates were similar in later days of wound healing (Figure 3.9) (day 14 and 21). After twenty-one days of recovery, almost the entire wound area was covered by granulation tissue, suggesting that granulation had been successfully completed in both groups (Figure 3.9).

Re-epithelialization, which is one of the main markers of successful wound closure, was determined by scoring the histological analysis of epithelial tissue. We demonstrated that percentage re-epithelialization was markedly higher in bioactive nanofiber gel-treated mice on day 7 (Figure 3.9B). This result further confirms that bioactive gel treatment promoted wound healing by accelerating wound closure and re-epithelialization.

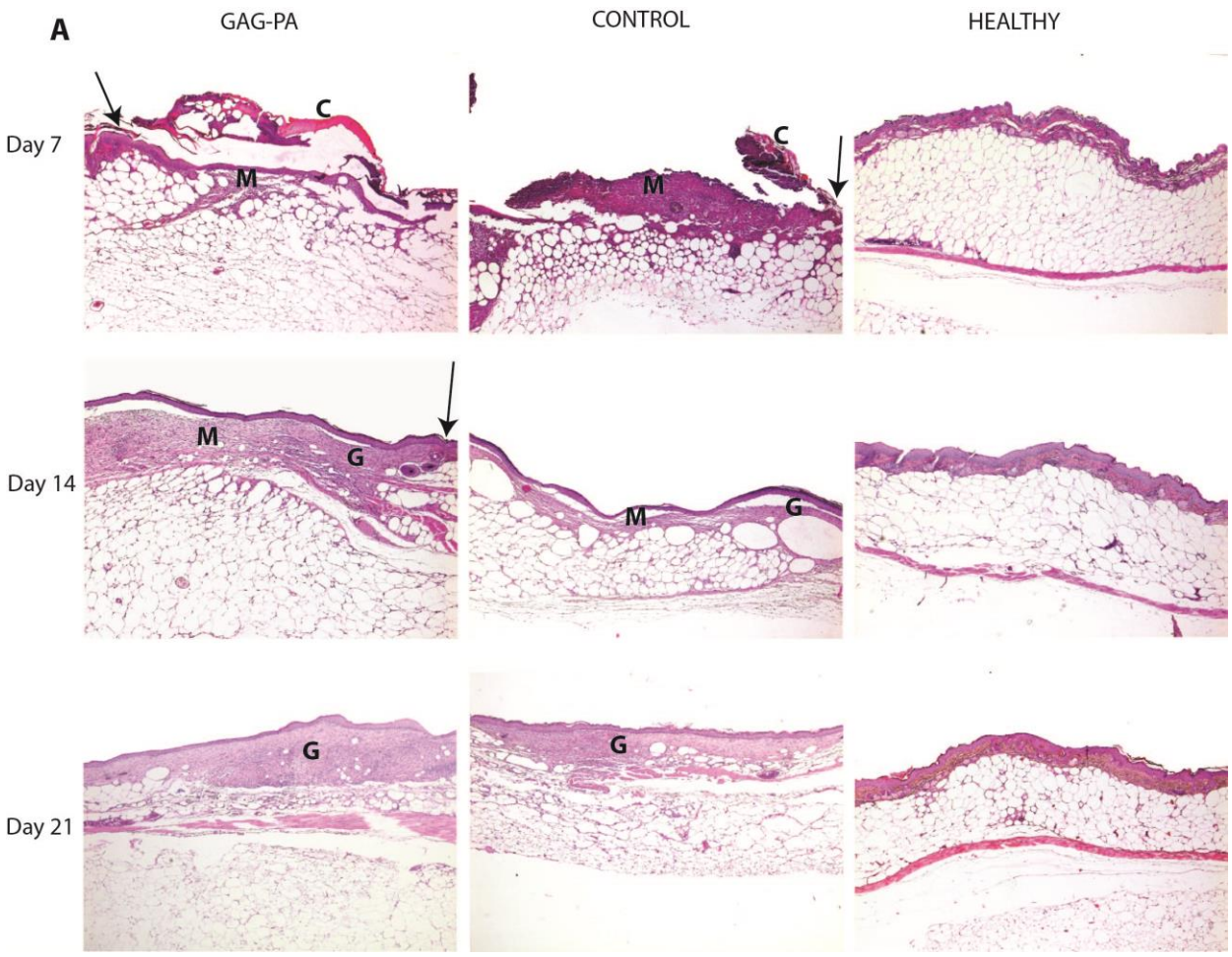

Figure 3.8 Histological analysis of H&E stained tissue sections from db/db mice treated with GAG-PA/K-PA and PBS, and unwounded controls. Changes in tissue morphology, such as the formation of a wound crust, wound matrix (M) and granulation tissue (G) were investigated throughout the recovery period . Arrows indicate original wound edge.

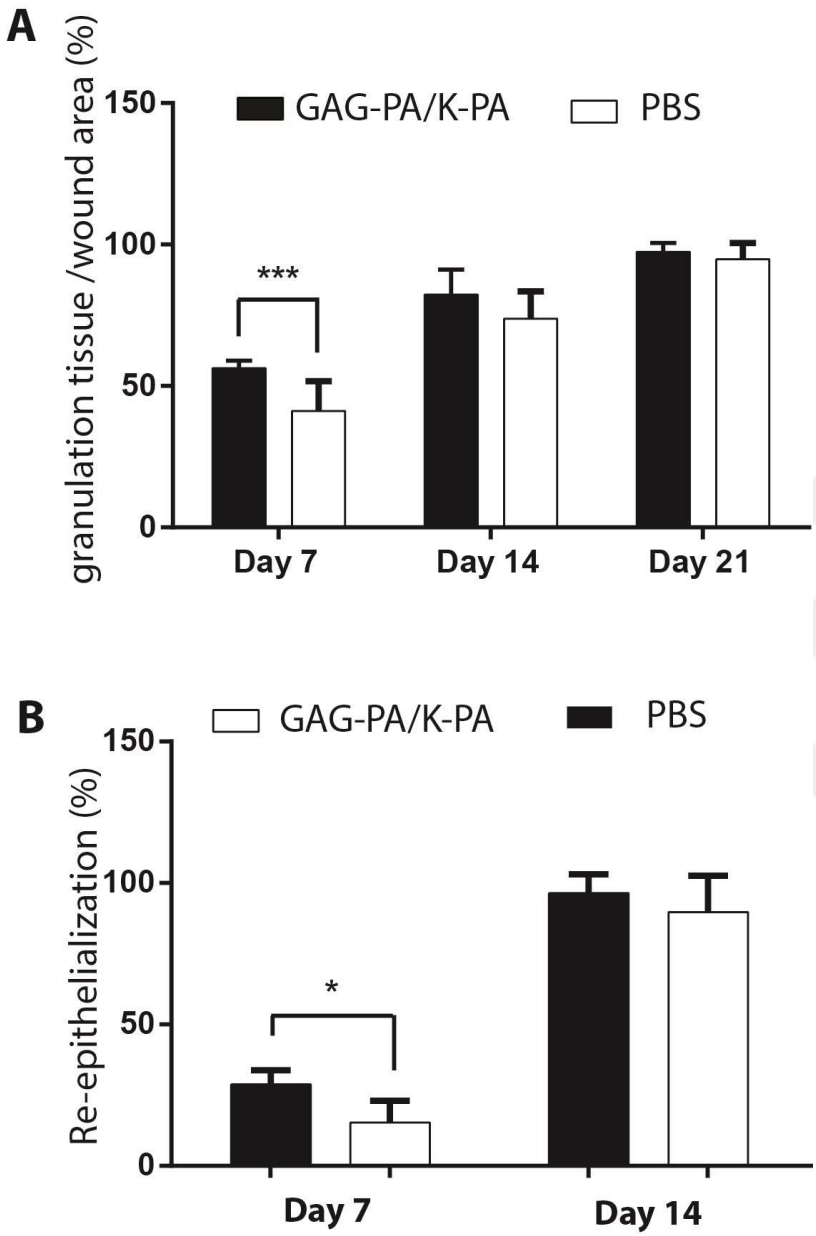

Figure 3.9 Analysis of tissue remodeling phase of diabetic wounds. The rate of granulation tissue formation was evaluated by calculating the ratio of the granulation tissue compared to the total wound area (A). In GAG-/PA-K-PA treated mice, re-epithelialization was faster on day 7 compared to PBS control (B).

3.3.7. Collagen deposition on db/db mice

Cross-sections of skin tissue were also stained by Masson's trichrome staining to understand whether bioactive gel treatment promotes collagen deposition. At the beginning of the proliferation phase, the collagen layer in the wound area mainly includes two types of collagens; type-I and type-III. However, collagen deposition occurs throughout the wound healing process, and newly deposited collagen is re-aligned at the remodelling phase in particular. Collagen alignment is not only critical for wound contraction, but also determines the severity of scar tissue formation [13]. Consequently, the localization and orientation of collagens were investigated with Masson's trichrome (Figure 3.10) and picrosirius red staining (Figure 3.12). In contrast to GAG-PA/K-PA treated mice, the ratio of collagen III/I rate in PBS control was significantly higher in the first seven days after wounding, but collagen deposition was nevertheless completed 21 days after wounding. Furthermore, the organization of collagens was analyzed under polarized light with picrosirius red staining. The green color represents type III collagen, whereas yellow and red color are indicators of type I [14]. As the wound healing proceeds, the green color disappeared and thick, yellow-red bundles of type I collagen can be observed in the wound areas of both groups (Figure 3.11). The pattern of collagen staining with picrosirius red was similar to Masson's trichrome staining, and collagens were more organized and aligned in GAG-PA/K-PA treated group compared to control. Masson's trichrome and picrosirius red staining results therefore showed that the remodeling phase of wound healing is more extensive in the bioactive PA-treated group compared to PBS-treated controls.

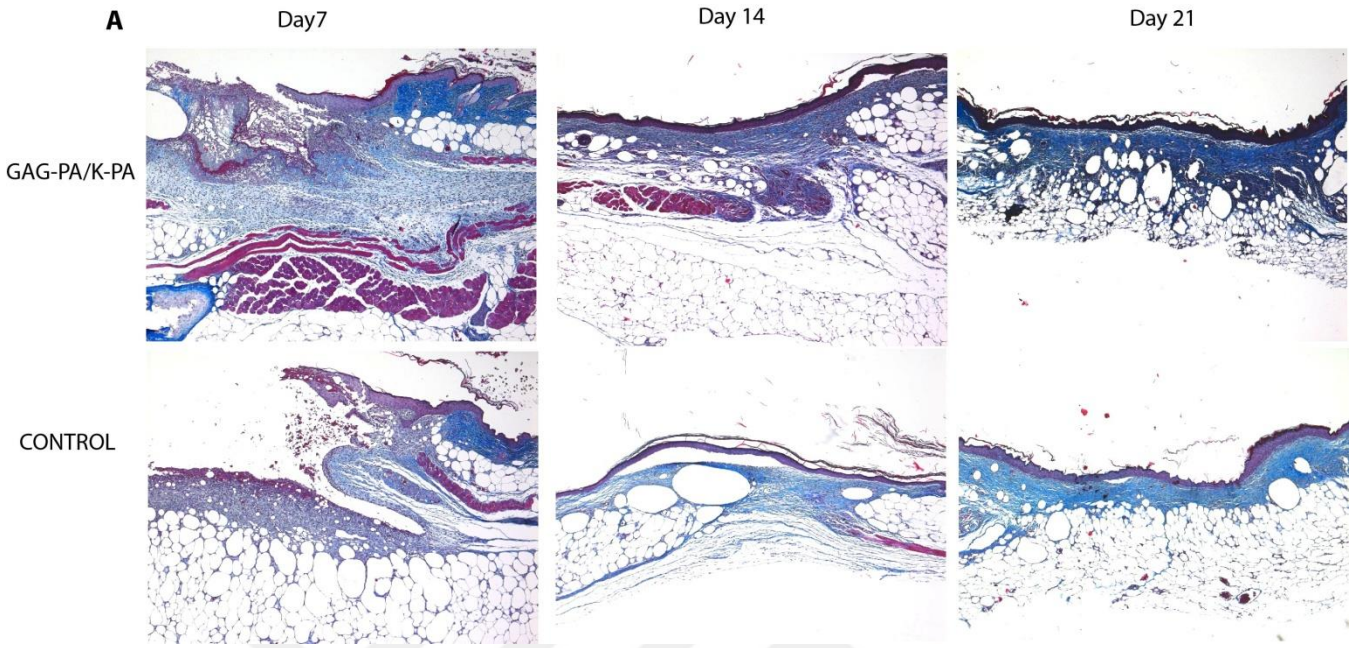

Figure 3.10 Massons' trichrome staining of wounds in both groups. The staining indicates that granulation tissue formation, re-epithelialization and cell infiltration occurs in both groups, but is faster in the bioactive gel-treated group on day 7.

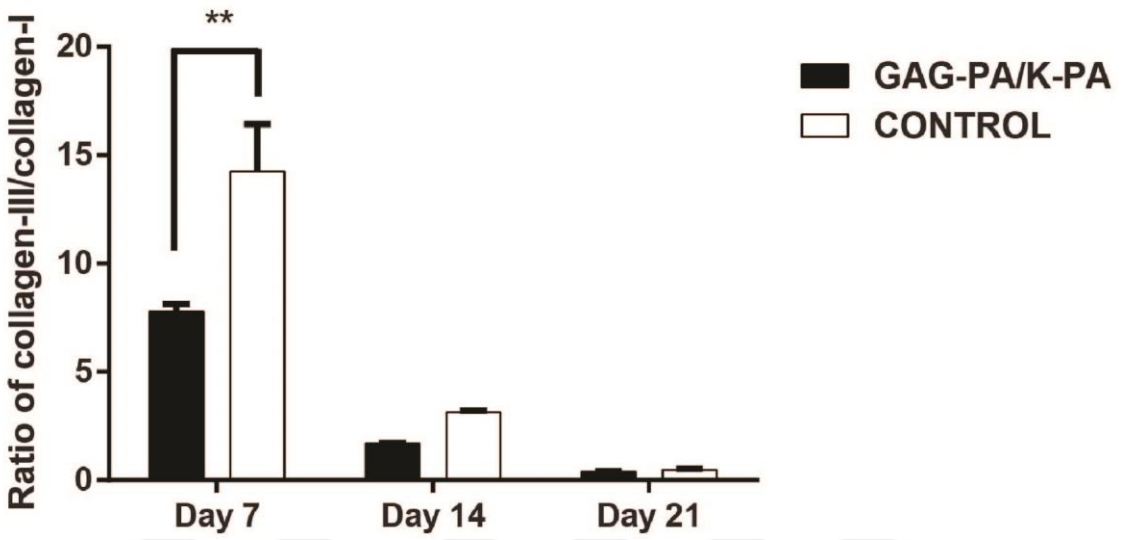

Figure 3.11 Quantification of the ratio of collagen III/I. The ratio of type III collagen to type I was dramatically lower on day 14, suggesting that collagen deposition was almost complete in both groups. Data are presented as means ± SEM, ***p< 0.001

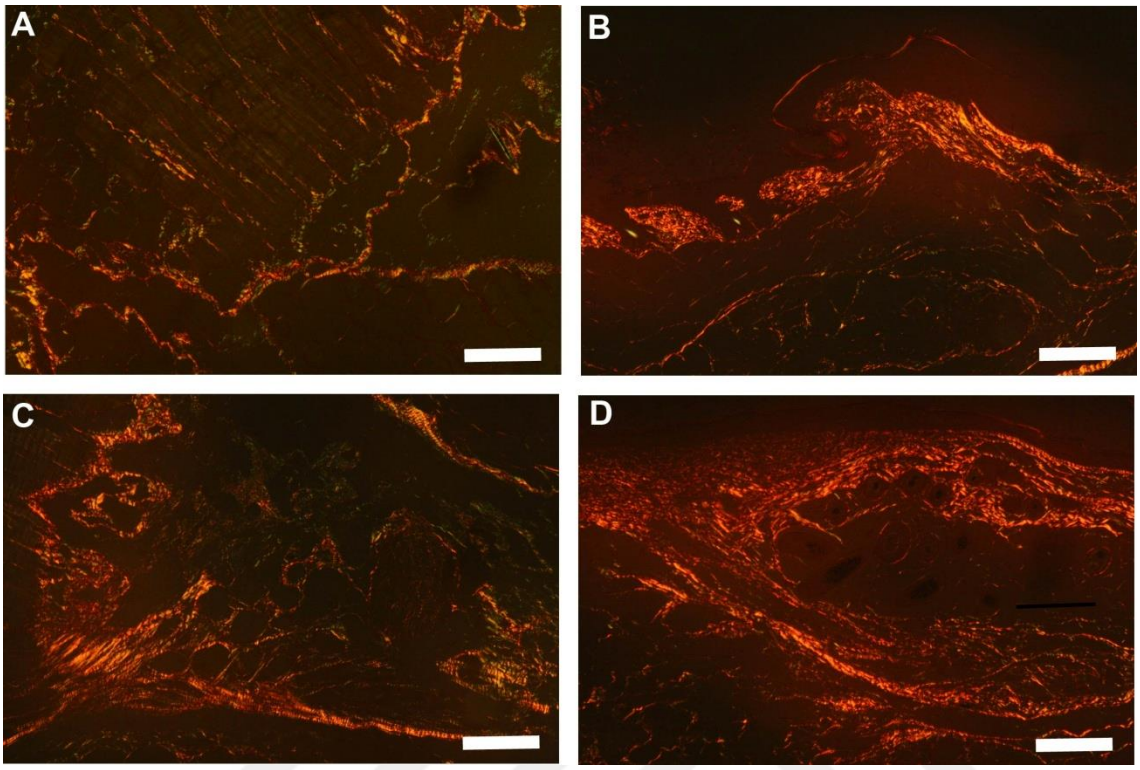

Figure 3.12 Collagen orientation in full-thickness diabetic wound samples treated with GAG-PA/K-PA and PBS. Sections were stained with Picrosirius Red in picric acid and photographed under cross-polarized light. Collagens were more organized in GAG-PA/K-PA treated group compared to PBS control (A vs. C and B vs. D). Images were taken on day 7 (A, C) and day 14 (B, D). Original magnification is 100x and scale bars are 200 µm.

3.3.8. Angiogenic response was accelerated with increased number of vessels and VEGF expression in heparin-mimetic gel-treated animals

It has been previously shown that GAG-mimetic PA nanofibers trigger the induction of angiogenesis in the cornea, and we were therefore prompted to determine whether enhanced angiogenesis is also present in diabetic wounds treated with this system [15]. Anti-Von Willebrand Factor antibody staining and VEGF expression analysis were performed to assess

neovascularization and the induction of angiogenesis (Figure 3.13). Blood vessel formation was examined by the immunohistochemical staining with von Willebrand Factor (Figure 3.13A). Quantifications were performed based on the positive staining of vWF and showed that the number of vessels was higher in the bioactive gel treated group compared to control on days 7 and 14 (Figure 3.13B). This result is consistent with the histological analysis of GAG-PA/K-PA treated wound tissue sections, which had a highly proliferative healing profile, especially on day 7.

Furthermore, the angiogenic response of diabetic wounds was investigated through the Western blot analysis of VEGF expression (Figure 3.14). The treatment of bioactive nanofibers significantly increased VEGF levels on days 7 and 21. Interestingly, the administration of GAG-PA/K-PA to the wound site did not cause a significant difference on VEGF expression on day 14. The number of blood vessels in GAG-PA/K-PA treated groups was higher than control on day 21 but the difference was not statistically significant. This result is in agreement with the increased expression profile of VEGF and supported the angiogenic activity of GAG-PA/K-PA treatment.

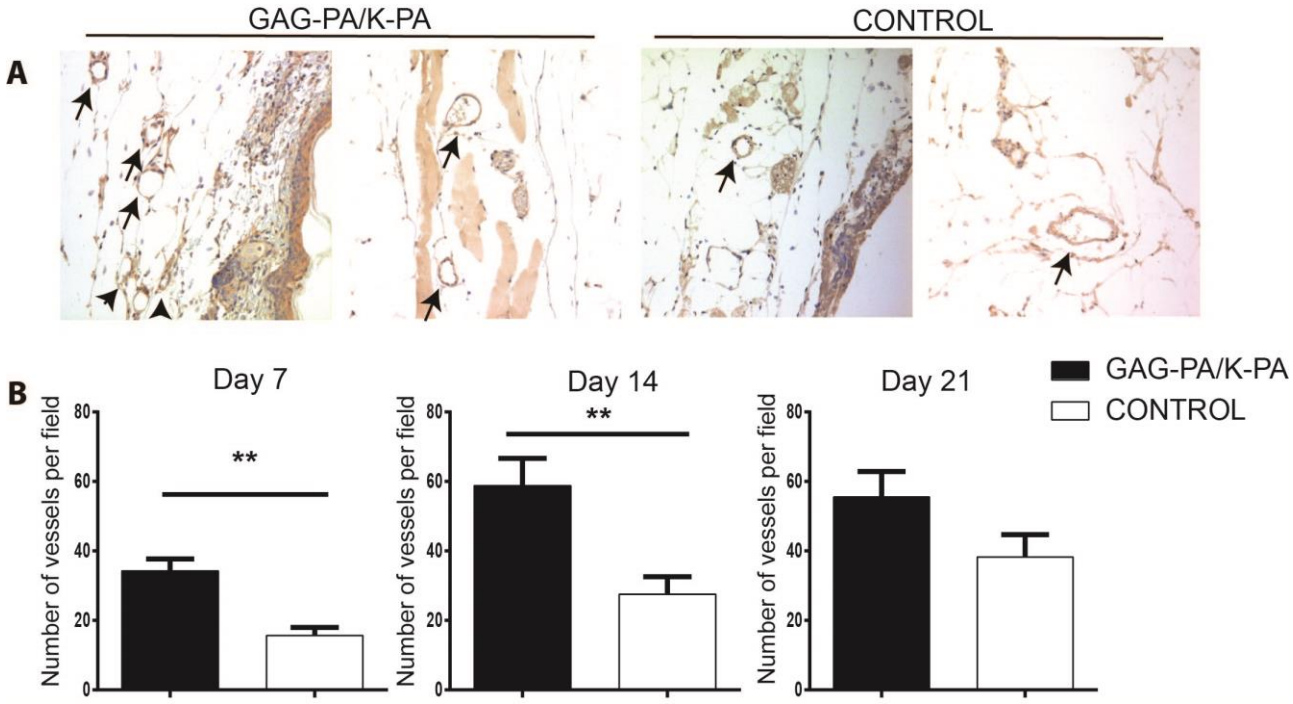

Figure 3.13 Angiogenic response of diabetic wounds from GAG-PA/K-PA and PBS treated mice. Immunohistochemical staining for von Willebrand Factor (vWF) (A) and quantification based on vWF staining (B) of the wound areas showed that number of blood vessels in bioactive gel treatment was higher than control on days 7 and 14. Arrows indicate blood vessels (brown color) (A).

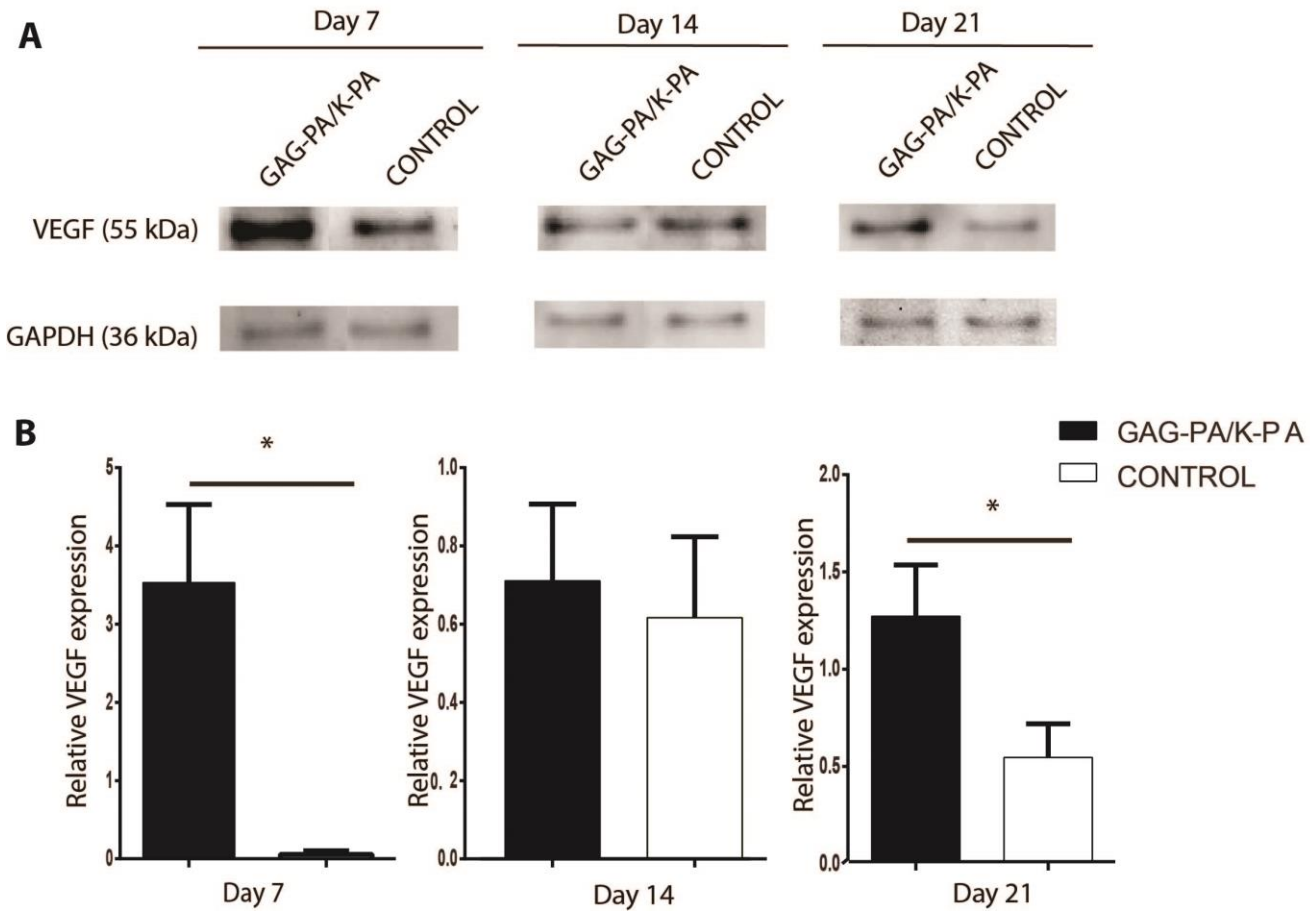

Figure 3.14 Western blot analysis of VEGF expression. Representative bands of GAG-PA/K-PA and control from western blot analysis of VEGF are shown in A. VEGF expression was quantified using Western blot bands and normalized to GAPDH (B).

3.3.9. α-SMA expression increases with bioactive gel treatment

The expression of α-SMA is a marker for the transition of fibroblast cells to myofibroblasts, which is essential for promoting wound contraction in tissue injury [16]. Besides myofibroblasts, α-SMA is expressed by pericytes, which are required for the maturation of blood vessels [17]. As such, α-SMA expression is an important marker for wound contraction and blood vessel maturation on wounds.

Immunohistochemical staining of wound tissue sections showed that the expression of α-SMA was higher in bioactive gel treated group on day 14 compared to control (Figure 3.25). Furthermore, western blot analysis was performed for quantification of SMA expression in tissue samples, and confirmed our α-SMA staining results (Figure 3.16). Similar to immunohistochemical analysis, protein levels of α-SMA increased two-fold following bioactive gel treatment compared to PBS controls on day 14 (Figure 3.16). However, α-SMA protein levels were very low and no change was observed between the groups at day 7, suggesting suggesting that the wounds were not mature enough to exhibit extensive α-SMA expression at this stage, while a large (but statistically non-significant) difference was observed between the groups at day 21. Immunohistochemical stainings for α-SMA also revealed extensive staining of blood vessel walls in the GAG-PA/K-PA treated wounds, suggesting that VEGF expression is upregulated in mice treated with the bioactive gel group.

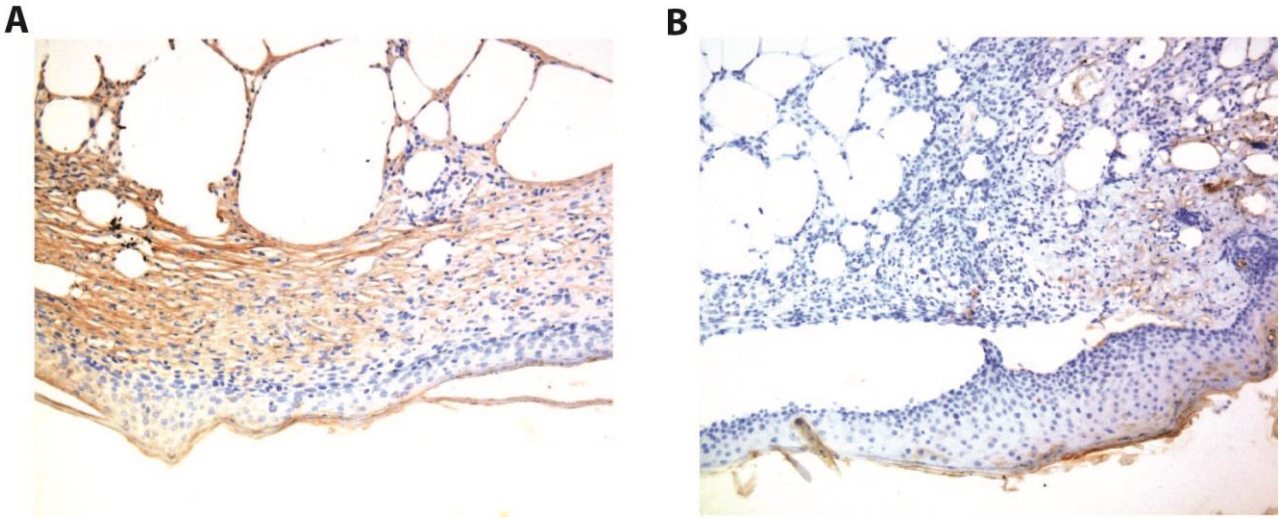

Figure 3.15 α-SMA expression increased in the wound area of bioactive gel treated samples. Alpha-SMA staining (brown) of tissue sections treated with GAG-PA/KP-A (A) and PBS control (B) on day 14, with hematoxylin counterstaining of nuclei (blue). The quantification

of α-SMA was based on Western blot analysis and normalized to GAPDH (C, D). Significance levels were set at: *p < 0.05.

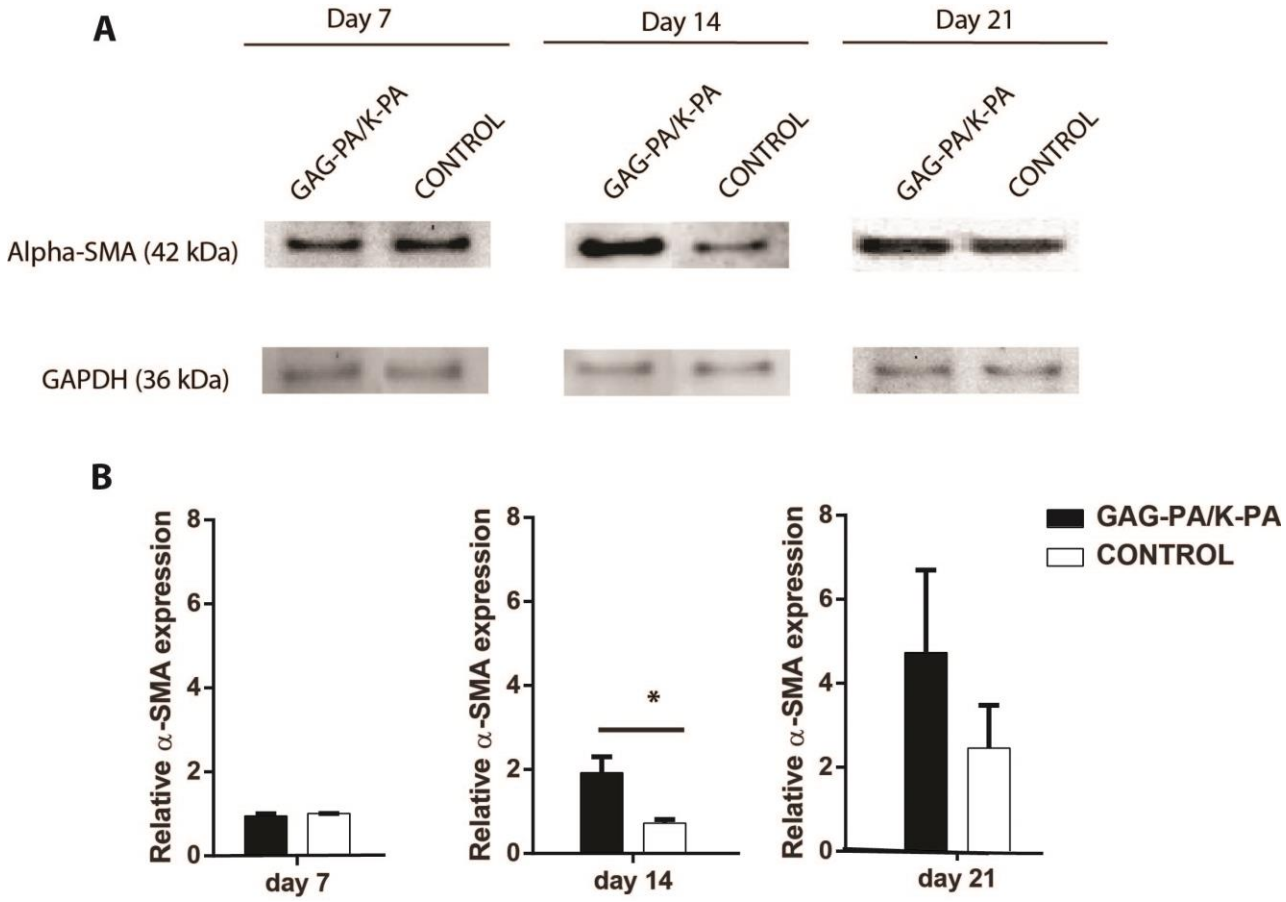

Figure 3.16 Western blot analysis of α-SMA expression on day 7, 14 and 21.

3.3.10. Heparin mimetic gel treatment affects wound inflammatory response

Characterization of inflammatory response of db/db mouse was performed by the ELISA analysis of two pro-inflammatory cytokines; IL-6 and TNF-α. IL-6 is a cytokine that is strongly expressed in cutaneous wounds, and its expression in db/db wounds was found to increase following the application of GAG-mimetic PA gels to the wound site. A significantly lower expression of the pro-inflammatory cytokine IL-6 was found in PA-treated wounds when compared with control at days 14 and 21 (Figure 3.17A). There was a marked increase of IL-6

expression in PBS-control treated wounds compared to their bioactive PA-treated counterparts (4.5 fold on day 14 and 2.5 folds on day 21), suggesting that the inflammatory response is prolonged in those animals. In contrast, the expression level of IL-6 in bioactive gel treated animals was close to that of unwounded db/db mice at these time points.

The expression of TNF-α was also found to exhibit a similar pattern as IL-6, with a significantly higher expression in both control and GAG-PA/K-PA-treated animals on day 7, which subsequently decreased on days 14 and 21 for bioactive but not PBS-treated groups (Figure 3.17B). These result suggest that treatment with GAG-PA/K-PA peptide nanofibers initially upregulates the expression of the pro-inflammatory cytokines IL-6 and TNF-α, but cytokine expression is then downregulated to mediate the transit from the inflammatory phase to the proliferative phase of wound healing.

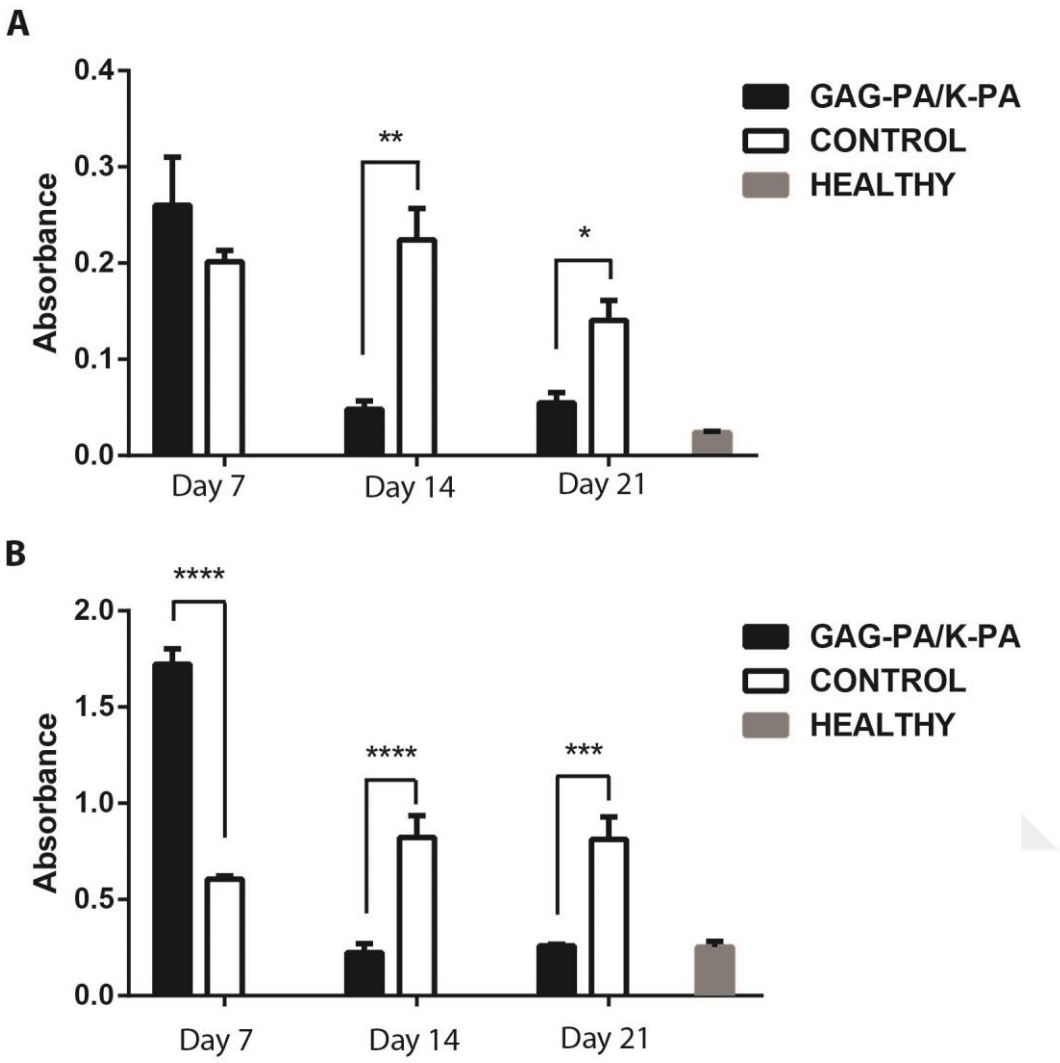

Figure 3.17 Expression of the pro-inflammatory cytokines IL6 (A) and TNF-α (B) in wound tissues on days 7, 14 and 21. IL-6 and TNF-α levels were measured by ELISA. Two-way ANOVA was performed to determine statistical significance, with significance levels set at: *p < 0.05, **p < 0.01, ***p < 0.001, ****p <0.0001.

3.4. Discussion

Diabetic wounds are characterized by a delayed healing response and potential progression into long-term ulcerations. Methods capable of enhancing their recovery is therefore critical to increase the quality-of-life of diabetic patients. In this work, we describe a novel hydrogel

platform that is able to improve the healing of diabetic wounds over a 21-day period. While the wounds were not completely closed even after 21 days of treatment, the open wound areas associated with bioactive hydrogel treatment were significantly smaller than control. In addition, histological methods were employed to evaluate the extent of granulation tissue formation, re-epithelialization and inflammation in the GAG-mimetic hydrogel-treated and non-treated groups, and a comparative analysis of each assay was performed to determine whether the repaired tissue is functional. A db/db mouse model was chosen to accurately reflect the pathophysiology of diabetes and investigate whether GAG-mimetic PA treatment is able to reduce the abnormalities in wound healing normally seen in diabetic injuries.

Skin wounds initially experience a rapid inflammation phase that recruits immune system cells to the site of injury, allowing the cleansing of cellular debris and prevention of bacterial infection. In addition, cytokines released during this phase support the recruitment, differentiation and proliferation of fibroblasts and epithelial cells, preparing the wound for the proliferative and remodeling phases that will follow the inflammatory response. The collagen deposition patterns of GAG-PA treated and non-treated animals suggest that bioactive peptide treatment increases the rate of tissue remodeling, as collagen III/collagen I ratios are consistently higher in controls compared to GAG-PA treated wounds. The wound remodeling process is characterized by a gradual switch from collagen III to the more stable collagen I, and the higher ratios of collagen III/collagen I seen in the control group suggests that remodeling is incomplete in these wounds. In contrast, GAG-PA treated animals exhibit a lower collagen III/collagen I ratio, suggesting that at least some amount of tissue remodeling had taken place even prior to day 7. α-SMA quantifications also support this conclusion, as this marker is associated with the maturation of myofibroblasts and was more abundant in GAG-treated samples at days 14 and 21.

Angiogenesis is another critical aspect of wound healing and primarily facilitates the transfer of oxygen and nutrients to the wound site during the proliferative and remodeling phases of wound healing. The inhibition of angiogenesis therefore imposes severe constraints to the metabolic resources that are available at the site of injury, and may consequently prevent wound closure in diabetic patients. Angiogenesis in GAG-mimetic PA-treated and non-treated mice was investigated by staining for von Willebrand factor, a glycoprotein that is a marker of neovascularization in the wound bed, and also by the Western blot analysis of VEGF. Von Willebrand staining results revealed extensive neovascularization occurs in bioactive PA-treated but not control groups, suggesting that the peptide network is able to enhance wound healing by facilitating the formation of new blood vessels. VEGF expression analyses further confirmed the presence of heightened angiogenic activity in diabetic wounds following GAG-mimetic PA treatment.

An important aspect of this study is the regulation of the pro-inflammatory cytokines TNF-α and IL-6 by GAG-mimetic nanofibers. While these markers are strongly expressed in recently inflicted wounds and serve to recruit and activate macrophages and leukocytes at the site of injury [99], their presence must gradually diminish for the healing process to continue. As such, a balance between pro-inflammatory and anti-inflammatory factors is necessary to stimulate the proliferation of native cells at the wound site following the initial recruitment of immune cells and removal of cellular debris. In db/db mice; however, a strong IL-6 and TNF-α presence is observed at both early and later stages of wound healing, leading to the sustained presence of pro-inflammatory macrophages and the impairment of the recovery process [100]. Our ELISA analyses suggest that IL-6 and TNF-α expressions are high in both GAG-mimetic PA-treated and control groups at day 7, but rapidly decrease in the bioactive hydrogel treated group by day 14 to

a level comparable to unwounded skin. In contrast, immunoregulatory markers are still strongly present at the wound site at days 14 and 21 for the control group, suggesting that biomimetic (but not control) hydrogels are able to modulate the immune response at the site of injury.

3.5. Conclusion

This study demonstrates that glycosaminoglycan mimetic PA nanofibers were able to induce angiogenesis and accelerate wound healing in genetically diabetic db/db mice. The application of bioactive gel to wound site was found to accelerate wound closure, re-epithelialization, myofibroblast activation and blood vessel formation. It has been previously shown that heparin-mimetic PAs provide an environment that leads the slow release of angiogenic growth factors, and especially VEGF. Molecular analysis of GAG-PA/K-PA treated wound tissues showed that VEGF expression was high even after 21 days following wounding. The remarkable increase on VEGF expression, together with positive α-SMA staining and extensive blood vessel formation at the wound site, suggests that angiogenesis is effectively induced by GAG-PA/K-PA in diabetic wounds. In addition, the expression pro-inflammatory markers IL-6 and TNF-α initially increase and subsequently decrease in GAG-PA/K-PA treated rats. A marked decrease in the expression of both markers is a strong evidence of improved transition between the inflammatory and proliferative phases in heparin-mimetic gel treated animals. The results of this study indicate a potential use of GAG-mimetic peptide nanofibers for the treatment of diabetic wounds exhibiting impaired regeneration.

3.6. Materials and Experimental Section

3.6.1. Materials

6 mm biopsy punches were purchased from Microtek Medical, Zutphen NL. ELISA antibodies for IL-6 (14-7061) and TNF-α (CMC3013) were purchased from eBioscience and Life Technologies, respectively. Db/db transgenic mice were supplied from ENVIGO, Indiana, USA. All ELISA reagents were purchased from Life Technologies. For peptide synthesis, 9-fluorenylmethoxycarbonyl (Fmoc) and tert-butoxycarbonyl (Boc) protected amino acids (except glyco-amino acid), [4-[α-(2',4'-dimethoxyphenyl) fmocaminomethyl]phenoxy]acetamidonorleucyl-MBHA resin (Rink amide MBHA resin) and 2-(1H-benzotriazol-1-yl)-1,1,3,3 tetramethyluronium hexafluorophosphate (HBTU) were purchased from NovaBiochem. DCM, DMF and TFA solutions were purchased from Sigma Aldrich.

3.6.2. Peptide synthesis and self-assembled nanofibrous network formation

Functionalized PA molecules were synthesized manually by standard solid phase Fmoc peptide synthesis chemistry. Lauryl-VVAGEGDK(pbs)S-Am (GAG-PA) and Lauryl-VVAGK-Am (K-PA) were synthesized on Rink amide resin. Amino acid coupling reactions were performed with 2 equivalents of Fmoc-protected amino acid, 1.95 equivalents of HBTU, and 3 equivalents of DIEA for 4 h. The Fmoc protecting group was removed with a 20% piperidine/DMF solution for 20 min. Peptides were cleaved from the resin using 95:2.5:2.5 TFA/TIS/H2O for 3 h. Excess TFA was removed by rotary evaporation. The remaining peptide was precipitated with ice-cold diethyl ether and freeze-dried. The peptide was characterized by quadruple-time-of-flight mass spectrometry (Q-TOF MS) and purified with reverse phase preparative HPLC (Fig.S.1).

Nanofibers were formed by mixing negatively charged GAG-PA and positively charged K-PA at pH 7.4 in a 1:2 ratio, respectively. Aqueous solutions of peptide amphiphiles were prepared in double distilled water.

3.6.3. Transmission Electron Microscopy (TEM)

GAG-PA/K-PA peptide nanofibers were diluted from 10 mM stock to 50 μM for TEM sample preparation. Peptide nanofibers were placed on a TEM grid, incubated for 7 min and stained with 2 wt % uranyl-acetate for 1 min. Imaging was performed with a FEI Tecnai G2 F30 TEM at 200 kV.

3.6.4. Scanning electron microscopy (SEM)

A mixture of GAG-PA and E-PA was prepared on a silicon wafer and incubated for 20 min for gelation. Peptide samples were dehydrated through gradually increasing concentrations of ethanol solutions and completely dried in a critical point dryer (CPD). Samples were coated with a 5 nm-thick Au-Pd layer and imaged by a FEI Quanta 200 FEG SEM, using the GSED detector at ESEM mode with 3-10 keV beam energy.

3.6.5. Circular dichlorism analysis

Secondary structures of nanofibers were assessed by circular dichroism (CD) analysis using a J-815 Jasco spectrophotometer. 3.6×10^{-4} M aqueous solutions of peptide amphiphiles were used for CD spectroscopy. Measurements were acquired at room temperature with a 500 nm/min scanning speed, 1 nm bandwidth and 0.1 nm data pitch within the data interval of 300 to 190 nm. Measurements were repeated three times and averaged for each sample. Results were represented as molar ellipticity.

3.6.6. Oscillatory Rheology

Oscillatory rheology measurements were assessed with an Anton Paar Physica MCR301. 10 mM of GAG-PA and K-PA were mixed 1:2 ratio as used in experiments. Rheological analyses were performed angular frequency was kept constant at 10 rad/s, and strain was increased between 0.1 and 100%. Storage and loss moduli were recorded accordingly.

3.6.7. Animals and wound healing model

All animal experiments were performed on 12-16 week old, genetically diabetic mice (db/db; BKS.Cg-+ *Lepr*^{db}/+ *Lepr*^{db}/OlaHsd, ENVIGO, USA, IN) in accordance with the guidelines set by the Etlik Diskapi Animal Ethics Committee.

Mice were anesthetized with xylazine hydrochloride (Alfazyne, 10 mg/kg) and ketamine hydrochloride (Alfamine, 25 mg/kg) and randomly divided into two cohorts as control (n=6) and GAG-PA/K-PA treated (n=6) groups. Two full-thickness circular wounds with 6 mm diameters were created on each animal using disposable biopsy punches. All wounded mice were housed individually. The wounding operation and postoperative treatments were performed by the same surgeon. Bioactive gels were applied topically to the wound area at a volume of 300 µl and concentration of 1% (w/v). Similarly, control wounds were treated with 300 µl of PBS solution. Both treatments were applied for 2 days. All wounds were covered with Octacare non-woven wound dressing (OCTAMED) to prevent the leakage of materials from the wound site. Animals were sacrificed on days 7, 14 and 21 for wound analysis.

3.6.8. Wound analysis

Mice were anesthetized with xylazine hydrochloride and ketamine hydrochloride prior to wound closure measurements. The wounds were photographed (day 7, 14, 21) and replicated on

transparent tracing paper (by tracing the border of the wound covered with epithelium) to calculate the percentage wound closure. The paper was then scanned and transferred into cross-sectional paper, and wound sizes were analyzed using ImageJ software.

3.6.9. Histological analysis

Removed skin tissues were fixed in 10% formaldehyde for 24h, embedded in paraffin and sectioned in 5 µm increments. Hematoxylin-Eosin (H&E) staining was performed for the determination of wound healing progress in the wound bed, and Masson's trichrome staining was performed for collagen deposition and granulation tissue analysis. Prior to both stainings, paraffin was removed with xylene washing and tissue sections were rehydrated through graded alcohols to distilled water. Rehydrated samples were either stained with hematoxylin and eosin (H&E) or immersed into phosphomolybdic acid, aniline blue, acetic acid and ethanol for Masson's trichrome staining. H&E- and Masson's trichrome-stained tissue sections were visualized on an up-right microscope (Zeiss Axio Scope A1).

Collagen content and organization was further investigated with picrosirius red. Picrosirius staining was performed with a counterstaining of hematoxylin. Slides were incubated in 0.1% Sirius Red in saturated picric acid for 1 hour at room temperature. They were then washed with acidified water, dehydrated through ethanol and xylene, and sealed with mounting medium. Picrosirius red staining slides were imaged under polarized-light microscopy (Zeiss Axio Imager.A2m).

3.6.10. Immunohistochemical (IHC) Staining Protocol

Paraffin embedded tissue sections were deparaffinized before IHC staining. Initially slides were immersed into xylene, two times for 10 min. Xylene- ethanol mixture was prepared and samples were treated for 5 min. For rehydration, slides were immersed into gradually reduced ethanol. Finally, samples were kept in water before antigen retrieval process. For HRP-conjugated detection such as 3,3'-diaminobenzidine (DAB), endogenous peroxidase activity was eliminated with hydrogen peroxide (H_2O_2). For this purpose 3% H2O2 solution was prepared and slides were treated for 10 min. Antigen retrieval is important for opening of epitopes especially in parafin embedded tissue sections. Methylene bridges are formed during the fixation procedure and mask epitopes and eliminate binding of antibodies. Antigen retrieval breaks those mthylene bridges and allows antibody interaction with epitopes. In this study two main types of antigen retrieval methods were used; heat mediated and enzymatic. Heat induced antigen retrieval is performed in vegetable steamer. Wide ranges of enzymes are used for antigen retrieval. Pronase was used for antigen retrieval before anti-von Willebrand Factor staining. Heat mediated antigen retrieval is used for anti-macrophage and anti-α-SMA staining. Sodium citrate buffer solution was prepared as in the following recipe;

Content	Sodium Citrate Buffer
Tri-sodium citrate (dihydrate)	2.94 g (10 mM)
Distilled water	1 L

Table 3.1 Buffer solutions for heat-induced epitope retrieval.

Tris sodium citrate was prepared in distilled water and pH of the solution is adjusted to 6.0 with 1 N HCl. 0.5 mL tween-20 is added into solution and can be store at RT for 3 months. For heat

mediated antigen retrieval method, sodium citrate buffer was added onto slide before placement into vegetable steamer. In general, slides were exposed to vapor for 15 to 30 min. After incubation slides were transferred under tap water to cool down. For enzyme mediated antigen retrieval, pronase was added onto slides and keep at 37 °C for 15 min. Then slides were washed with water in order to remove the enzyme and cool down the temperature of slides. Slides were washed for 5 min two times with 0.025% Triton X-100 in TBS with gentle agitation. Washing steps are important for removing of non-specific binding and Fc receptors. Blocking solution was prepared with 10 % nomal goat serum and 1% BSA in TBS and slides were incubated for 2 h with it. BSA in blocking solution reduces non-specific binding of primary and secondary antibodies. Slides were drained and wipe out with tissue paper around the tissue sections. Primary antibody is prepared in TBS with 1% BSA solution. The concentrations of each primary and secondary antibody were determined with optimization. The primary antibody; anti-von Willebrand Factor (1:500) was applied and incubated for overnight at 4°C. Next day remove the primary antibody by tapping and HRP-conjugated secondary antibody (1:500) was applied for 1 h at room temperature. Similar to primary antibody, secondary antibody was prepared in TBS with 1% BSA. After incubation slides were washed three times with TBS for 5 min. DAB chromogen and substrate were mixed and mixture was added onto slides. DAB is oxidized in the presence of peroxide and produces brown color reaction product. After 10 min of incubation counterstaining was applied. Hematoxylin was applied as counterstaining of all tissue sections. Mounting medium was added to cover the slides.

3.6.11. Protein isolation and Western blotting

Skin samples were homogenized in Trizol® reagent, and the protein-containing supernatant was removed and stored at -80 °C. Protein concentrations were determined using a BCA Protein

Assay Kit. An equal amount of protein per lane (50 μg) was separated by 5~12% SDS-PAGE and transferred to a polyvinylidene difluoride (PVDF) membrane. The membrane was blocked with 5% non-fat milk in TBS-T at room temperature for 2 h and then incubated with anti-VEGF antibody (Abcam, UK, 1 : 2000) and α-SMA antibody (Millipore, 1:50000) overnight at 4°C. After washing in TBS-T, the blots were incubated with a horseradish-coupled secondary antibody (goat anti-rabbit IgG; 1:2000, ab). The bands were visualized using Clarity™ western ECL blotting substrate. GAPDH (Millipore; 1:1000) was used as the internal control and treated with the same protocol. Protein amounts in each sample were quantified using ImageJ software.

3.6.12. ELISA

Cytokine concentrations in wound tissues were measured at the end of the experiment by ELISA. MaxiSorp™ plates (Thermo Scientific, NUNC) were coated with IL-6 (1:1000) or TNFα (1:500) primary antibodies through overnight incubation at 4 °C. On the next day, plates were washed, dried by tapping, blocked with 0.5% BSA (2 h) and incubated with isolated protein from tissues (overnight incubation at 4 °C). On the following day, protein samples were consecutively labeled with biotin-labeled secondary antibody (2 h) and HRP (horse radish peroxidase)-conjugated streptavidin (1 h) at room temperature. Plates were washed 5 times with washing buffer and dried by tapping between each consecutive step. TMB (3,3′,5,5′-Tetramethylbenzidine) substrate was added at the last step and the reaction was stopped after 30 min by 1.8 N H_2SO_4. Colour formation was measured by a microplate reader (Spectramax M5, Microplate reader) as absorbance at 450 nm wavelength. In order to obtain exact absorbance values that are attributable solely to dye color, the measured values were subtracted from a reference value (at 650 nm). All treatments were performed with at least three replicates and shown as mean ± standard deviation.

3.6.13. Statistical analysis

Statistical analyses were performed using GraphPad Prism 5. Data analysis was carried out using the student's t test with the raw data. When multiple comparisons were performed, two-way ANOVA was used. Error bars indicate ± SEM (standard error of mean).

Chapter 4

Inhibition of VEGF mediated corneal neovascularization by anti-angiogenic peptide nanofibers

4.1. Objective

Atypical angiogenesis is one of the major symptoms of severe eye diseases, including corneal neovascularization, and the complex nature of abnormal vascularization requires targeted methods with high biocompatibility. The targeting of VEGF is the most common approach for preventing angiogenesis, and the LPPR peptide sequence is known to strongly inhibit VEGF activity by binding to the VEGF receptor neuropilin-1. Here, the LPPR epitope is presented on a peptide amphiphile nanofiber system to benefit from multivalency and increase the anti-angiogenic function of the epitope. Peptide amphiphile nanofibers are especially useful for ocular delivery applications due to their ability to remain on the site of interest for extended periods of time, facilitating the long-term presentation of bioactive sequences. Consequently, the LPPR sequence was integrated into a self-assembled peptide amphiphile network to increase its efficiency in the prevention of neovascularization. Anti-angiogenic effects of the peptide nanofibers were investigated in both *in vitro* and *in vivo* models. LPPR-PA nanofibers inhibited endothelial cell proliferation, tube formation, and migration to a greater extent than the soluble LPPR peptide in vitro. In addition, the LPPR-PA nanofiber system led to the prevention of vascular maturation and the regression of angiogenesis in a suture-induced corneal angiogenesis model. These results show that the anti-angiogenic activity exhibited by LPPR peptide nanofibers may be utilized as a promising approach for the treatment of corneal angiogenesis.

Keywords: corneal neovascularization, anti-angiogenesis, peptide amphiphiles, neuropilin-1.

4.2. Introduction

Angiogenesis is the formation of new blood vessels from pre-existing networks and is tightly regulated through the activation of endothelial cells, local degradation of the extracellular matrix and vascular basement membranes, and stabilization of newly formed vessels through the proliferation and migration of the native cell population [12]. Endothelial cell activation or *turnover* status is critical for the modulation of this process and is determined by the positive (angiogenic) and negative (anti-angiogenic) regulators of angiogenesis, including VEGF, aFGF and bFGF [13]. Abnormalities in the production of these growth factors and their downstream elements may result in excessive or insufficient blood vessel formation, potentially interfering with the function of affected tissues.

Pathological angiogenesis occurs in many disorders, including corneal neovascularization, which causes visual impairment through the loss of ocular transparency [14]. Vascular endothelial growth factor (VEGF) and its receptors have been found to be significant modulators of angiogenesis, and their inhibition is an effective means of corneal neovascularization treatment. Although bevacizumab therapy has been shown to facilitate the regression of corneal neovascularization in animal studies and clinical reports, its effectiveness is limited by safety issues and the recurrence of neovascularization in certain cases [15]. High costs, difficulties of manufacturing and short half-lives are further disadvantages of bevacizumab and other antibody drugs [16]. Therefore, new therapeutics and formulations capable of eliminating these deficiencies are urgently needed.

4.2.1. Anatomy of the Cornea

The cornea is approximately 0.5 mm thick and contains six layers (Figure 3.1). No blood vessels are found in the cornea; as such, all available oxygen is obtained from tears. The epithelium layer is found on the anteriormost part of the cornea and functions as a barrier. The epithelium contains cells that exhibit a high capacity for regeneration. Bowman's layer is an acellular and nonregenerating layer that is found between the epithelium and the stroma. The stroma is composed of highly arranged collagen fibers and water, and forms the majority of the cornea. It does not contain any blood vessels and is perfectly transparent. One of the diseases related to stroma is macular corneal dystrophy. Dua's Layer is an acellular and strong structure which contains collagen-I fibers. Descemet's layer is the inner layer of basement membrane and provides a protective barrier against injury and infection. The corneal endothelium contains mitochondria-rich cells that are responsible for regulating the stromal fluid. Death of endothelial cells causes the destruction of fluid balance and loss of corneal transparency.

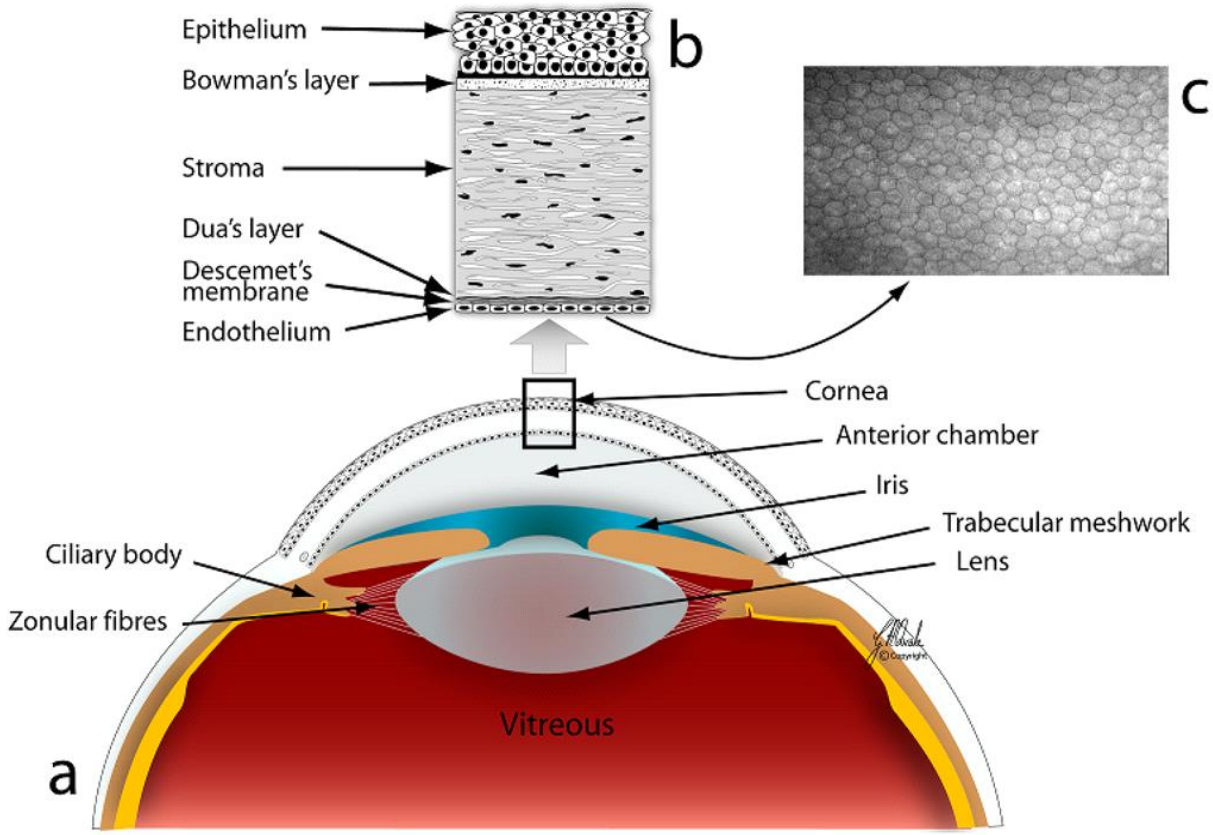

Figure 4.1 Schematic representation of cornea anatomy. Illustration of anterior of the eye (a). Cornea consists of endothelium, descremet's membrane, stroma, Bowman's layer and epithelium (b). Microscopic image of corneal endothelium (c) [17].

4.2.2. Corneal Neovascularization

Corneal neovascularization is an ocular disorder that caused by newly formed blood vessels disturbing the clarity of vision, potentially leading to vision failure [18]. The normal cornea is a transparent and avascular tissue. Expressions of angiogenic growth factors are accelerated upon injury and new blood vessels grow from the limbus. Pathogenesis of corneal neovascularization may be related not only to corneal injury but also to inflammation, contact lens–related hypoxia, chemical burns, corneal graft rejection, and infectious keratitis [19]. Inflammatory

neovascularization occurs due to injury, viral and bacterial infections. Contact lenses might cause increases in the level of lactate synthesis, which is a product of anaerobic metabolism. High levels of lactate stimulate macrophages and lead to the activation of angiogenic factors.

Vascular endothelial growth factor (VEGF) is a regulator of vascularization in many tissues and its expression is upregulated upon hypoxic injury in the cornea. VEGF family includes VEGF-A, placenta growth factor, VEGF-B, VEGF-C and VEGF-D. VEGF-A is especially important for the neovascularization process and binds its tyrosine kinase receptors VEGF-R1 (Flt-1) and VEGF-R2 (KDR-Flt-1) to activate pro-angiogenic responses in many tissues. There are many subtypes of VEGF receptors; such as VEGFR-1, VEGF-R2, VEGF-R3 (Flt-4) and neuropilin. Strategies involving the blocking of VEGF-A with monoclonal antibodies saw considerable success in inhibiting corneal neovascularization in animal models [20].

Fibroblast growth factor (FGF) is another growth factor that is directly correlated with corneal neovascularization. It has been shown that angiogenic properties of FGF are related to the interplay between FGF and VEGF [21]. Platelet-derived growth factor (PDGF) is responsible for stabilization of blood vessels by attracting pericyte progenitor cells. Strategies involving the usage of VEGF and PDGF antagonists were more effective than the blockage of VEGF in rabbits [22].

4.2.3. Treatment of Corneal Neovascularization

One of the current treatments of corneal neovascularization is corticosteroids. The effect of therapy can be improved by the combination of bevacizumab with corticosteroids such as betamethasone. However, corticosteroid treatment carries a high risk of cause glaucoma and cataracts. Photodynamic therapy may also be applied, and involves the irradiation of an injected

photosensitive dye to trigger the apoptosis or necrosis of endothelial cells and inhibit vascularization. Studies with verteporfin (Visudyne) showed that the reapplication of photodynamic therapy gave positive results under the metrics of angiogenic regression and vascular occlusion in patients [23]. Disadvantages of photodynamic therapy are high costs, complications in laser irradiation and side effects regarding the formation of reactive oxygen species in the eye [24].

Anti-VEGF agents, and especially anti-VEGF antibodies, are more widely used drugs for the treatment of corneal neovascularization. Bevacizumab, brand name Avastin® (Genentech), is a humanized monoclonal IgG1 antibody that directly binds VEGF, thereby preventing its interaction with VEGF receptors. U.S. Food and Drug Administration (FDA) approval was given for this drug in 2004 for its usage in the treatment of metastatic colorectal, glioblastoma, renal cell carsinoma, cervical and lung cancer [25]. The molecular weight of Avastin® is around 149 kDa, and the drug can be administrated via injection or topical application. Although Avastin® is not approved to treat corneal neovascularization, many studies showed its efficacy in the inhibition of angiogenesis [26]. Studies with bevacizumab treatment showed that it reduced the severity of neovascularization either through subconjunctival injection or topical application [27, 28]. Dastjerdi and colleagues showed that treatment with bevacizumab via subconjunctival injection is more effective than topical application in facilitating the regression of neovascularization in mice [26]. In the literature, there are many case studies showing that the efficiency of bevacizumab treatment resulted in significant regression of neovessel invasion area [28, 29].

4.2.4. Anti-angiogenic Properties of Peptide Nanofibers

Peptide-mediated targeting strategies exhibit considerable potential for inhibiting the activity of angiogenic factors. Self-assembled peptide amphiphile nanofibers consist of a hydrophilic head group containing bioactive epitopes and β-sheet forming sequences, which is chemically conjugated to a hydrophobic tail region that further assists in the assembly process [30]. They have a wide range of applications, such as tissue engineering, regenerative medicine, diagnostic tools, drug delivery and functional biomaterials [31-33]. They are favorable over proteins and other small molecules due to their stability and ease of preparation and purification. In addition, several reports have recently shown that peptide systems can be used as angiogenesis inhibitors [34-36].

The LPPR peptide sequence has previously been identified by the phage display technique and was shown to bind specifically to the VEGF receptor, neuropilin-1 (NRP-1) [37]. This binding strongly inhibits the activation of NRP-1 by $VEGF_{165}$, and the LPPR sequence is responsible for 75% of this inhibition [38]. In addition, the peptide was able to significantly decrease tumor growth through the inhibition of angiogenesis in an *in vivo* breast cancer model, while a similar peptide sequence, D(LPR), exhibited promising results for the treatment of retinopathy of prematurity [39, 40]. Since the LPPR peptide sequence is essential for the inhibition of VEGF activity, we utilized this peptide sequence on a self-assembled peptide amphiphile nanofiber system to increase epitope presentation and create a highly effective anti-angiogenic agent.

The Lauryl-VAAGKKGLPPR-Am peptide amphiphile molecule was designed and synthesized to form a β-sheet containing supramolecular structure, thereby increasing its solubility in water and presenting the functional epitope on a nanofiber system. The self-assembly process,

secondary structure and cellular localization of the peptide nanofibers were characterized in detail. The capacity of the peptide nanofiber formulation to inhibit blood vessel formation was then evaluated by using *in vitro* angiogenesis, scratch healing and tube formation assays. In addition, the effect of nanofibers was studied in an *in vivo* suture induced corneal neovascularization model. The efficiency of the bioactive PA nanofibers was found to be comparable to the commercially available drug bevacizumab and superior to the soluble peptide formulation.

4.3. Results

4.3.1. Synthesis and characterization of PAs

In this study, the LPPR peptide sequence was conjugated to a β sheet-forming peptide amphiphile molecule to create an effective anti-angiogenic nanofiber system. The nanofibrous morphology of this self-assembled peptide system can increase the presentation of the bioactive sequence to the VEGF receptor NRP-1, thereby blocking the former's angiogenic effect through competitive exclusion. In addition, the well-ordered structure of the peptide nanofiber system may increase the presentation of the bioactive epitope to the VEGF receptor neuropilin-1. As such, the soluble LPPR peptide was also synthesized in addition to the amphiphilic form. Lauryl-VVAGKKGLPPR-Am (LPPR-PA) was mixed with lauryl-VVAGE (E-PA) at a 1:1 ratio to form bioactive LPPR-PA nanofibers, while lauryl-VVAGKKK-Am (K_3-PA) was mixed 1:1 with E-PA to form non-bioactive control nanofibers. Both PA mixtures have a final charge of +1, resulting from the respective charges of E-PA (at -2) and LPPR-PA and K_3-PA (both at +3) (Figure 4.2). Chemical views of all peptides are given in Figure 3.4A. Solid-phase peptide

synthesis was used in the production of all peptide molecules used, and the peptide products were characterized by LC-MS and purified with preparative HPLC (Figure 4.3).

Circular dichroism (CD) spectroscopy was utilized to analyze the secondary structures associated with formation of nanofiber by peptide amphiphiles and their mixtures [20]. CD results showed that the nanofibrous structures formed by PA molecules contained β-sheet structures, as evidenced by their absorbance maxima at around 200 nm and minima at around 220 nm (Figure 4.4C). TEM and STEM were performed to investigate the morphology of the self-assembled nanostructures in solution and confirmed that the peptide formulations exhibited nanofibrous morphology (Figure 4.4B). Both control and LPPR-PA nanofiber structures were 10-20 nm in diameter and up to several micrometers in length. TEM imaging of the non-amphiphilic LPPR peptide did not yield observable results due to its lack of network formation.

The effect of peptide nanofibers on cellular viability of endothelial cells was analyzed with Live/Dead assay, which demonstrated that LPPR, control and LPPR-PA nanofiber did not alter the viability of HUVECs at a concentration of 100 μM (Figure 4.5). Cell survival rate of all treatment groups were similar to those on tissue culture plate (TCP) after 24, 48 and 72 h of incubation (Figure 4.5). Overall, these results indicated biocompatibility of control and LPPR-PA nanofibers.

A

Peptide sequence	Nomenclature	Net Charge (*)
Ac-LPPR-Am	LPPR	+1
Lauryl-VVAGKKGLPPR-Am	LPPR-PA	+3
Lauryl-VVAGE	E-PA	-2
Lauryl-VVAGKKK-Am	K3-PA	+3

(*) Theoretical net charge at pH 7.4

B

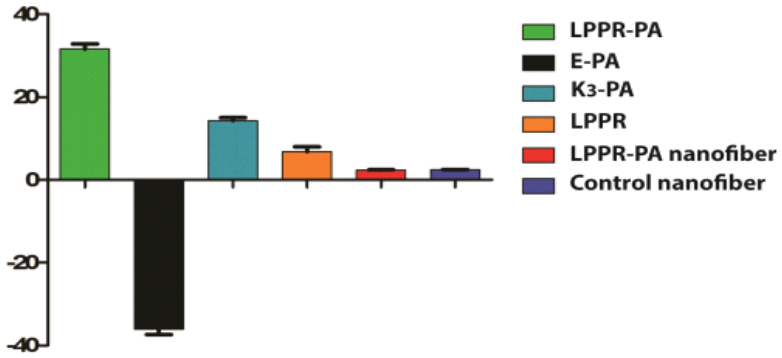

Figure 4.2 Peptide sequence with abbreviations and charges. The net charges of peptides were measured by zeta potential at pH 7.4.

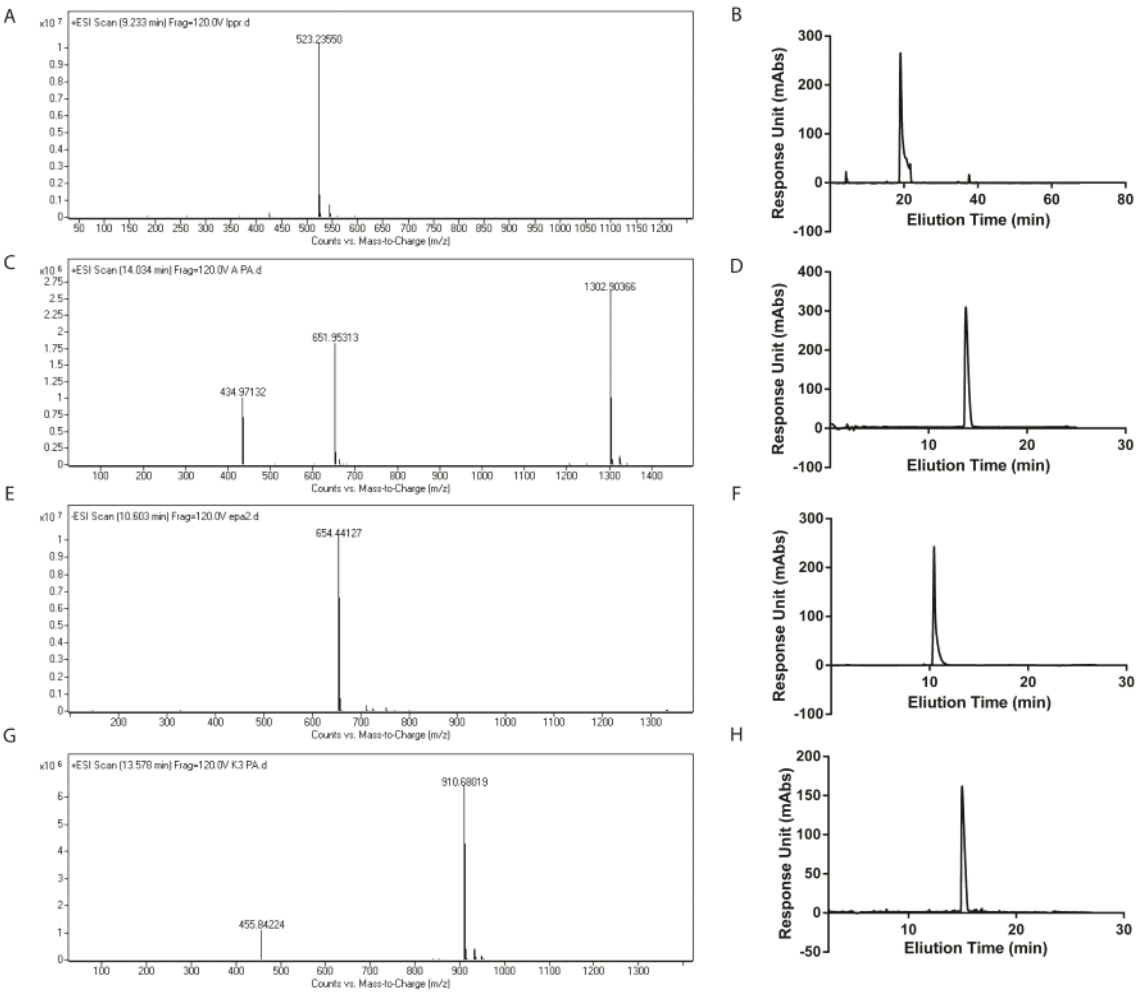

Figure 4.3 Liquid Chromatography and mass spectroscopy analysis of peptide and peptide amphiphile (PA) molecules. HPLC chromatogram of purified Ac-LPPR-Am (B), LPPR-PA (D), E-PA (F) and K_3-PA (H) molecule at 220 nm. Mass spectra of peptides; for LPPR $[M-H]^-$ (calculated) = 522.65, $[M-H]^-$ (observed) = 523.23 (A), for LPPR-PA $[M-H]^-$ (calculated) = 1302.72, $[M-H]^-$ (observed) =1302.90, $[M/2-H]^-$ (calculated) = 651.36, $[M/2-H]^-$ (observed) = 651.95, $[M/3-H]^-$ (calculated) = 434.24, $[M/3-H]^-$ (observed) = 434.97 (C), for E-PA $[M-H]^-$ (calculated) = 655.82 $[M-H]^-$ (observed) = 654.44 (E), for K_3-PA $[M+H]^+$ (calculated) = 910.24 , $[M+H]^+$ (observed) = 910.68, $[M/2+H]^+$ (calculated) = 455.12, $[M/2+H]^+$ (observed) =455.84 (G).

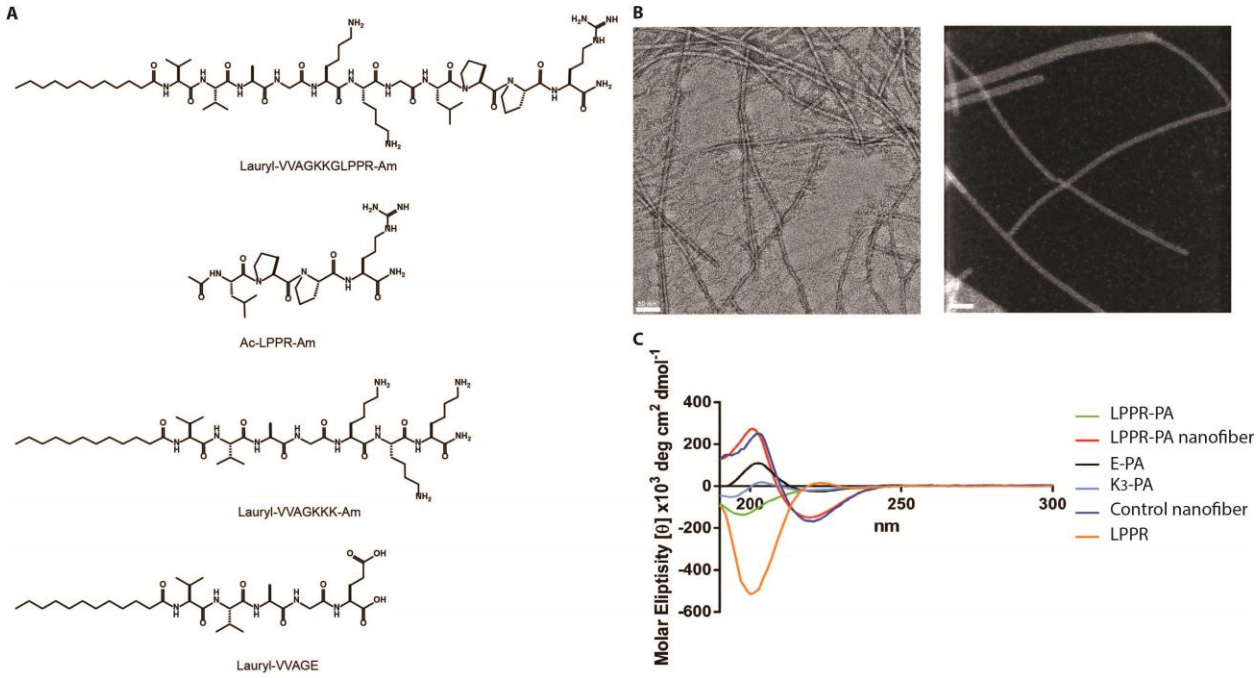

Figure 4.4 Self-assembled peptide amphiphile (PA) nanofibers at pH 7.4. Chemical structures of LPPR-PA, LPPR, E-PA and K_3-PA are provided (A). TEM images of the LPPR-PA nanofibers and STEM of control nanofibers were stained with uranyl acetate (scale bar = 50 μm) (B). LPPR-PA and control nanofibers formed β-sheet secondary structures analyzed by CD measurements (C).

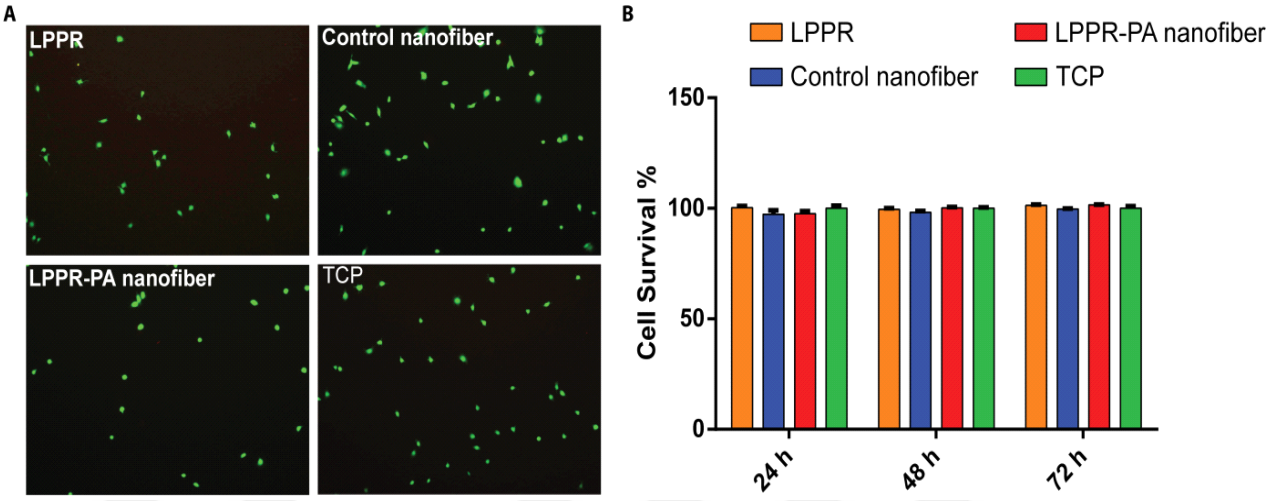

Figure 4.5 Viability of HUVECs cultured with peptides, PA nanofibers and TCP, as analyzed by Live/Dead assay. Qualitative (A) and quantitative (B) results showed that peptide samples and peptide nanofibers did not alter the viability of HUVECs compared to TCP.

In order to determine localization of LPPR-PA nanofiber peptide was mixed with FITC-labeled K_3-PA. During the synthesis of FITC labeled K_3-PA, Fmoc-Lys(Mtt)-OH was used. Mtt removal was performed by shaking peptides with TFA:TIS:H_2O:DCM in the ratio of 5:2.5:2.5:90 for 5 min, then washed with DCM. Fluorescent K_3-PA were synthesized by removing of Mtt and reacting with fluorescein isothiocyanate (FITC) while on resin. Furthermore the binding of LPPR-PA to HUVECs was investigated with confocal microscopy. K_3-PA was labeled with fluorescein by reacting with fluorescein isothiocyanate (FITC) (Figure 3.6). Cellular localization and distribution of the peptide was observed after 24 h. Confocal images showed that LPPR-PA nanofiber bind membranes of HUVECs and not present at the interior of cells (Figure 3.7).

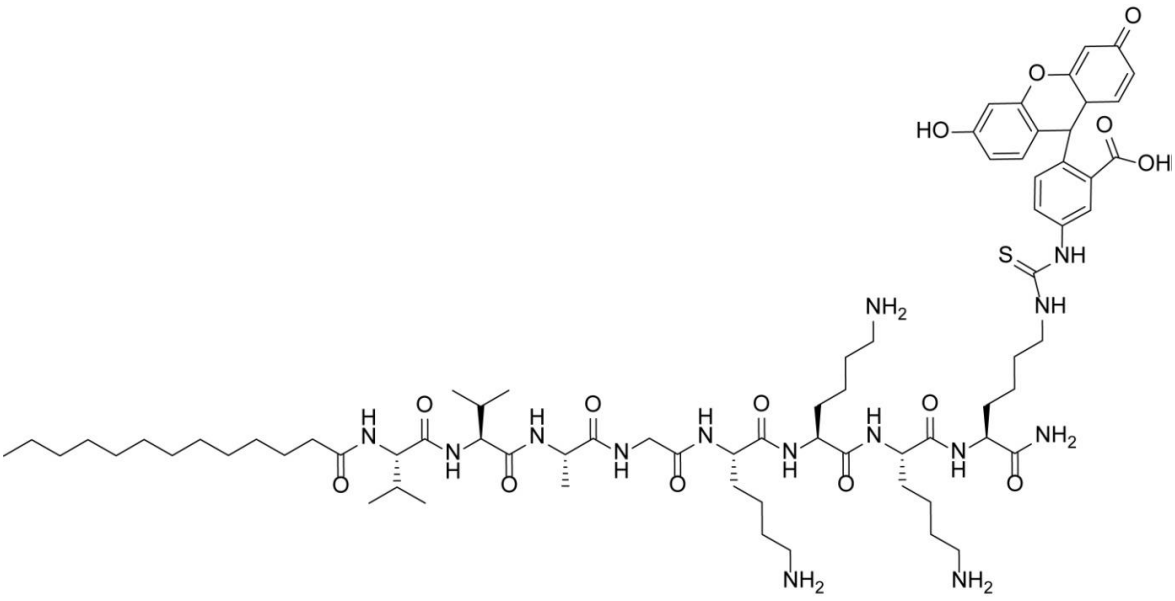

Figure 4.6 Chemical view of FITC labeled K_3-PA.

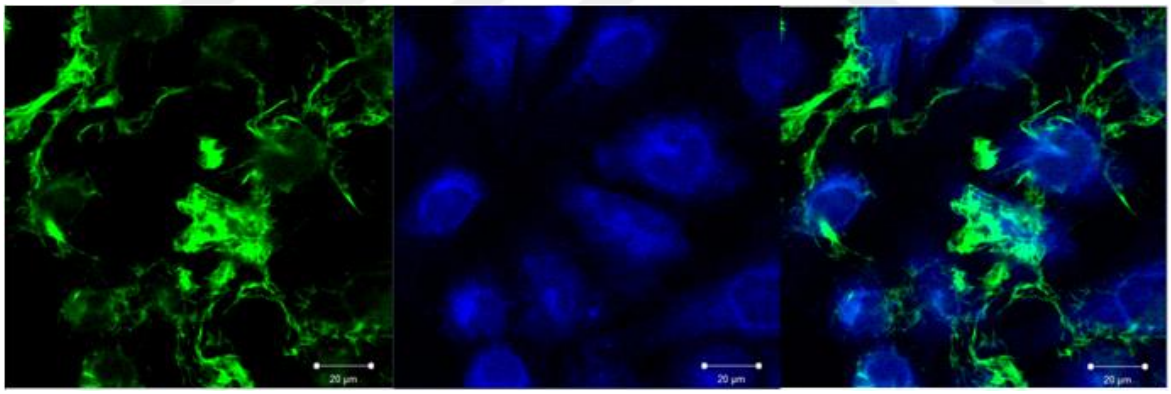

Figure 4.7 The localization of LPPR-PA nanofiber on HUVECs. The binding of FITC labeled LPPR-PA nanofiber to HUVECs was detected by confocal microscopy (green: FITC-PA (A), blue: TO-PRO-3(B), merge (C)).

4.3.2. LPPR-PA/E-PA treatment reduces endothelial cell proliferation, migration and angiogenic tube formation

Cell proliferation, migration and tube formation assays were performed to systematically assess the anti-angiogenic effect of LPPR-PA nanofibers on endothelial cells. Angiogenic regulators, such as VEGF stimulate the proliferation of endothelial cells during blood vessel formation; consequently, the proliferation of HUVECs was evaluated in the presence of VEGF to determine whether the peptide networks were able to disrupt the VEGF/NRP-1 interaction. Our results demonstrated that LPPR-PA nanofibers inhibited cell proliferation in a dose-dependent manner and with an IC_{50} of 107 μM, suggesting that the sequence is able to interfere with endothelial cell growth when incorporated into a peptide hydrogel material (Figure 3.8). Tournaire and colleagues have previously shown that ATWLPPR peptide treatment caused 60% inhibition in vascular endothelial cell proliferation at a concentration of 420 μM [14]. Here, 100 μM of LPPR peptide did not cause any effect on the proliferation of HUVECs, while the PA form of this sequence was much more effective in mediating the inhibition of cell proliferation. The inhibitory effect of LPPR-PA was also found to be sequence-specific, since control nanofiber did not show any activity at the same concentration (Figure 3.8A).

The migration of endothelial cells is an important step of angiogenesis and can be evaluated *in vitro* by scratch wound healing assay, where a gap is created on a cellular monolayer and its closure is measured to determine the rate of the surrounding cells migrating into the wound [21]. The inhibitory activity of LPPR-PA nanofibers was determined by analyzing the wound closure percentage of HUVECs after 24 h (Figure 3.9). Migration was found to be significantly lower than control in HUVECs treated with LPPR-PA nanofiber in the presence of VEGF. In addition, control nanofibers also inhibited cell migration compared to tissue culture plate (Figure 3.9B).

Consistent with the proliferation assay results, scratch wound closure measurements demonstrated that VEGF-mediated angiogenesis was markedly blocked by LPPR-PA nanofibers.

During angiogenesis, endothelial cells proliferate and migrate toward an angiogenic growth factor stimulus, and eventually form lumen-bearing tubes to conduct the blood flow. A Matrigel™ tube formation assay was therefore performed to investigate the anti-angiogenic properties of peptide formulations by quantifying their ability to prevent the formation of endothelial tubes. Matrigel™ contains a mixture of basement membrane components that stimulate endothelial cells to form capillary-like hexagonal structures, and is often preferred over other *in vitro* assays because of its ease of use and the ability to provide a rapid and quantitative assessment of angiogenesis [22]. Here, growth factor-reduced Matrigel™ reagent was used with 100 μM of VEGF to investigate VEGF-induced tube formation. Angiogenesis assay showed that only TCP control had well-ordered tube structures (Figure. 3.10A). Furthermore, tube length measurements were performed to compare the efficacy of treatments in inhibiting angiogenesis. LPPR peptide, control nanofiber, LPPR-PA nanofiber and bevacizumab treatments inhibited tube length by 67.3±7.19 %, 73.6±7.68 %, 93.08±6.19 % and 89.8±10.1 % compared to TCP, respectively. These data indicated that peptide treatments in general reduced the tubular assembly of endothelial cells, but LPPR-PA nanofiber treatment caused the most significant inhibition of tube lengths (Figure 3.10). The inhibition rate was as strong as bevacizumab treatment, suggesting that LPPR-PA nanofiber treatment was able to suppress VEGF-induced angiogenesis *in vitro*.

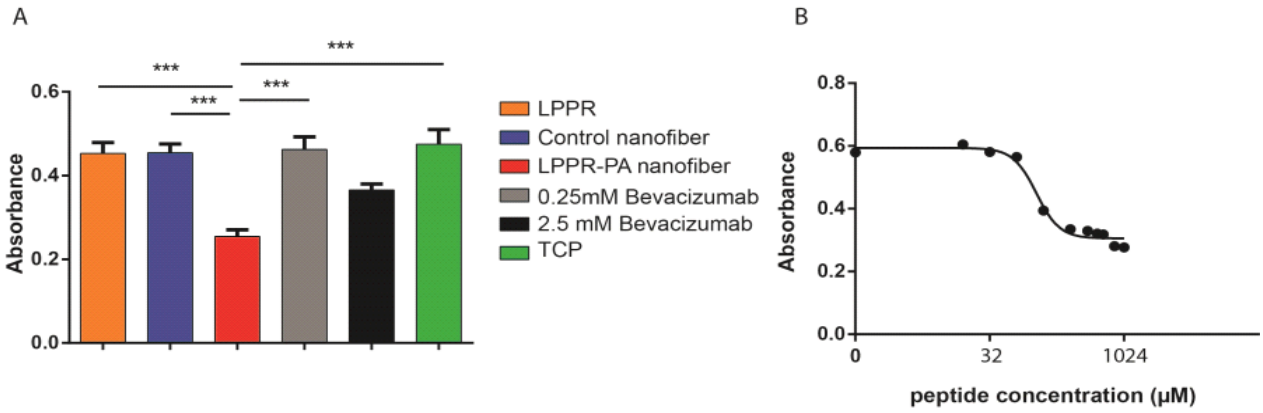

Figure 4.8 The quantification of inhibitory effects of LPPR-PA nanofiber on HUVECs. Effects of peptides and bevacizumab treatment on proliferation were investigated with proliferation assay (A). HUVECs were treated with different concentrations of peptides for 24 h to assess IC_{50} calculation of LPPR-PA by using an ELISA based-BrdU assay (B). Data are presented as means ±SEM, ***p<0.001. Scale bars 50 nm.

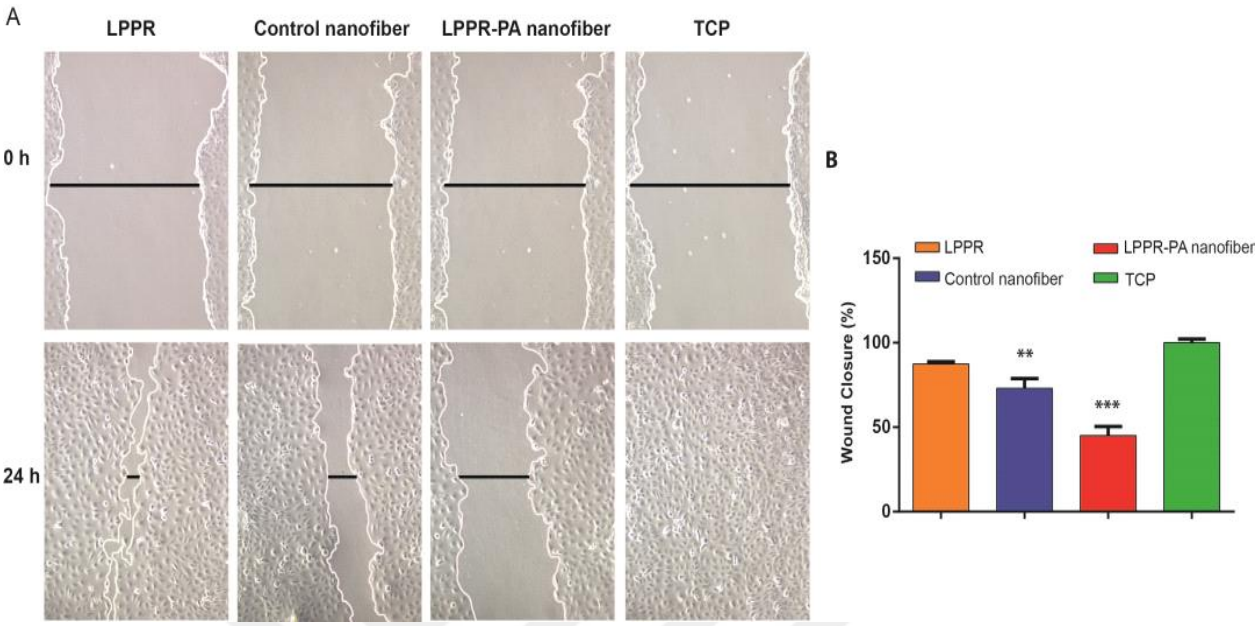

Figure 4.9 Anti-angiogenic peptide treatment inhibits cell migration. HUVECs treated with peptides or control was scratched and cell migration was imaged after 24 h (A). Both control and LPPR-PA nanofiber treatment significantly suppressed cellular migration. Wound margins were determined and closure percentages were calculated with Image J (B). One-way ANOVA analysis was performed at ** $p < 0.01$, and *** $p < 0.001$; images were taken at 100 X magnification.

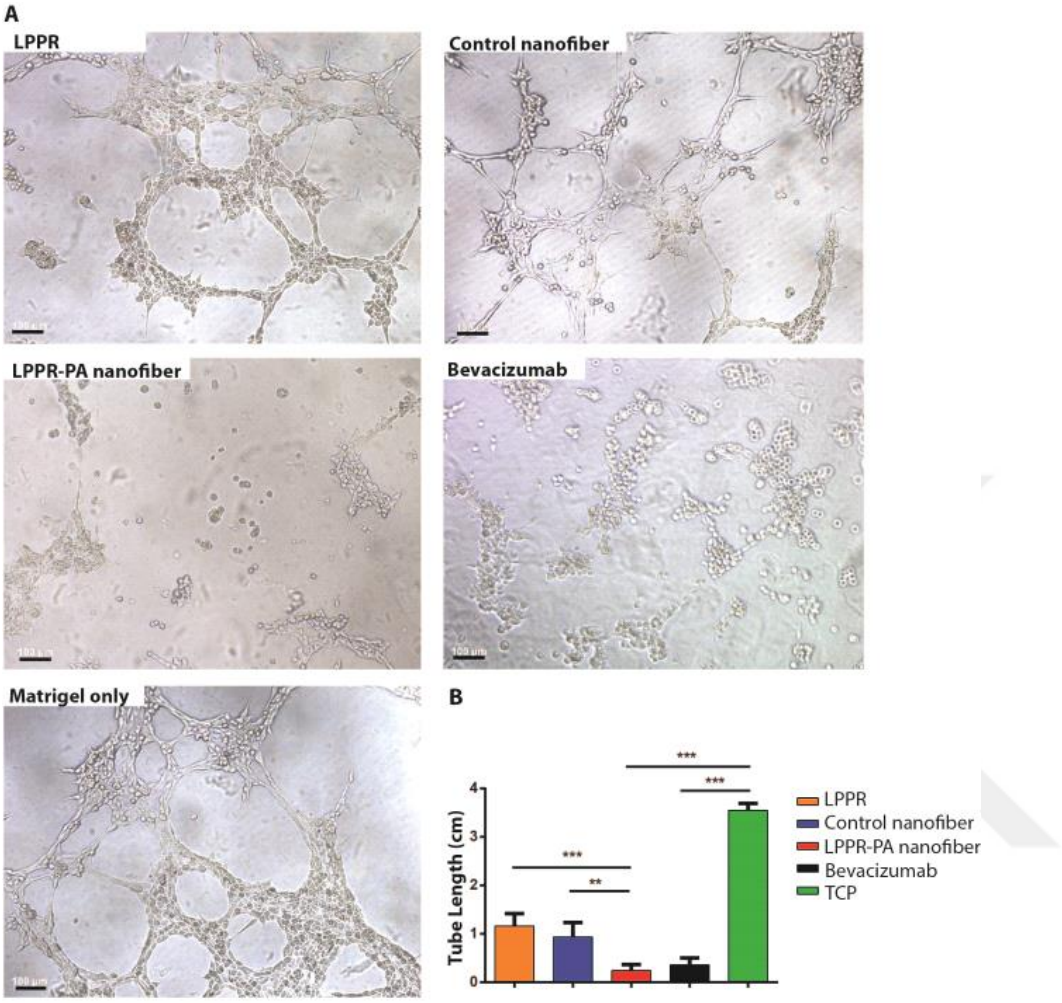

Figure 4.10 LPPR-PA nanofiber treatment suppressed tube formation in a Matrigel™ based angiogenesis assay. HUVECs with and without peptide treatment were plated on Matrigel™ and imaged after 6 h of incubation (A). Tube lengths were measured from images using Image J (B). One-way ANOVA analysis was performed at * $p < 0.05$ and *** $p < 0.001$. Scale bars 100 µm.

4.3.3. The subconjunctival injection of LPPR-PA nanofibers inhibits suture-induced corneal neovascularization

After demonstrating the anti-angiogenic activity of LPPR-PA nanofibers *in vitro,* we next investigated the *in viv*o efficacy of peptide nanofibers using a suture-induced corneal angiogenesis model. Preliminary studies showed that neovascularization began to occur near the corneal suture on day 1 or 2 after surgery and had advanced greatly by day 7. Consequently, subconjunctival injection of peptides was performed on day 7 to better reflect the clinical presentation of corneal neovascularization, which is typically diagnosed only after advanced neovascularization.

The *in vivo* anti-angiogenic activity of LPPR-PA nanofibers was evaluated through the measurement of blood vessel growth areas. Corneal neovascularization was induced in all treatment groups with a similar vessel growth area on day 7 (Figure 3.11 and 3.12). Representative images of corneas on day 14 and schematic illustration of *in vivo* experiments were given in Fig. S4. The subconjunctival injection of LPPR-PA nanofiber significantly inhibited corneal neovascularization in rats compared to other treatment group on day 14 (Figure 3.12). Moreover, the efficacy of the peptide nanofiber was higher than the LPPR peptide and bevacizumab: Bevacizumab showed a 51.2 % inhibition of corneal neovascularization in our rat model, while LPPR-PA nanofiber treatment resulted in around 81.3% inhibition relative to untreated controls. The efficacy of subconjunctival bevacizumab treatment in this model was similar to its efficacy in humans, suggesting that LPPR-PA nanofiber may be a better alternative for corneal neovascularizaiton therapy [23]. However, further studies are required to compare the safety of nanofiber injections and conclusively demonstrate the advantage of anti-angiogenic peptides for the treatment of CN.

The effects of the anti-angiogenic peptide nanofibers on new vessel formation were further characterized through von Willebrand factor staining on day 14 after surgery. The total number of vessels was calculated from both central and peripheral areas of the corneal surface. Histological and quantitative analyses of the cornea revealed that LPPR-PA nanofiber treatment led to a significant reduction in the number of blood vessels compared to untreated control (Figure 3.14). Although corneal neovascularization was not completely regressed, only a small number of vessels had remained in the peripheral area after a single injection of LPPR-PA. These data, in tandem with vessel growth area calculations, indicate that VEGF suppression plays an important role in the inhibition of corneal angiogenesis, and that LPPR-PA treatment can effectively reduce corneal neovascularization through this process.

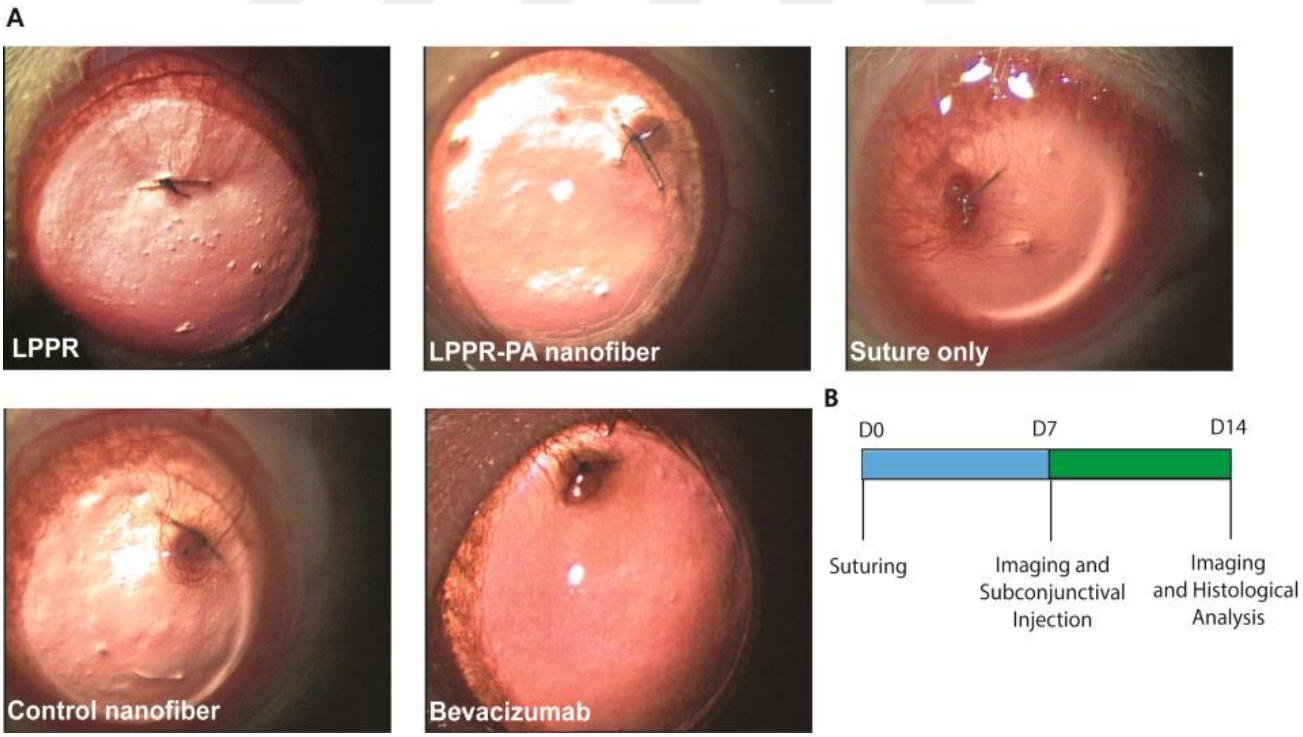

Figure 4.11 Representative images of LPPR, LPPR-PA nanofiber, control nanofiber, bevacizumab treated corneas and untreated control. Schematic diagram of *in vivo*

experiments (B). Suturing operation was performed on day 0, and 7 days after materials delivered to cornea via subconjunctival injection. Imaging and histological analysis of corneas was performed on day 14.

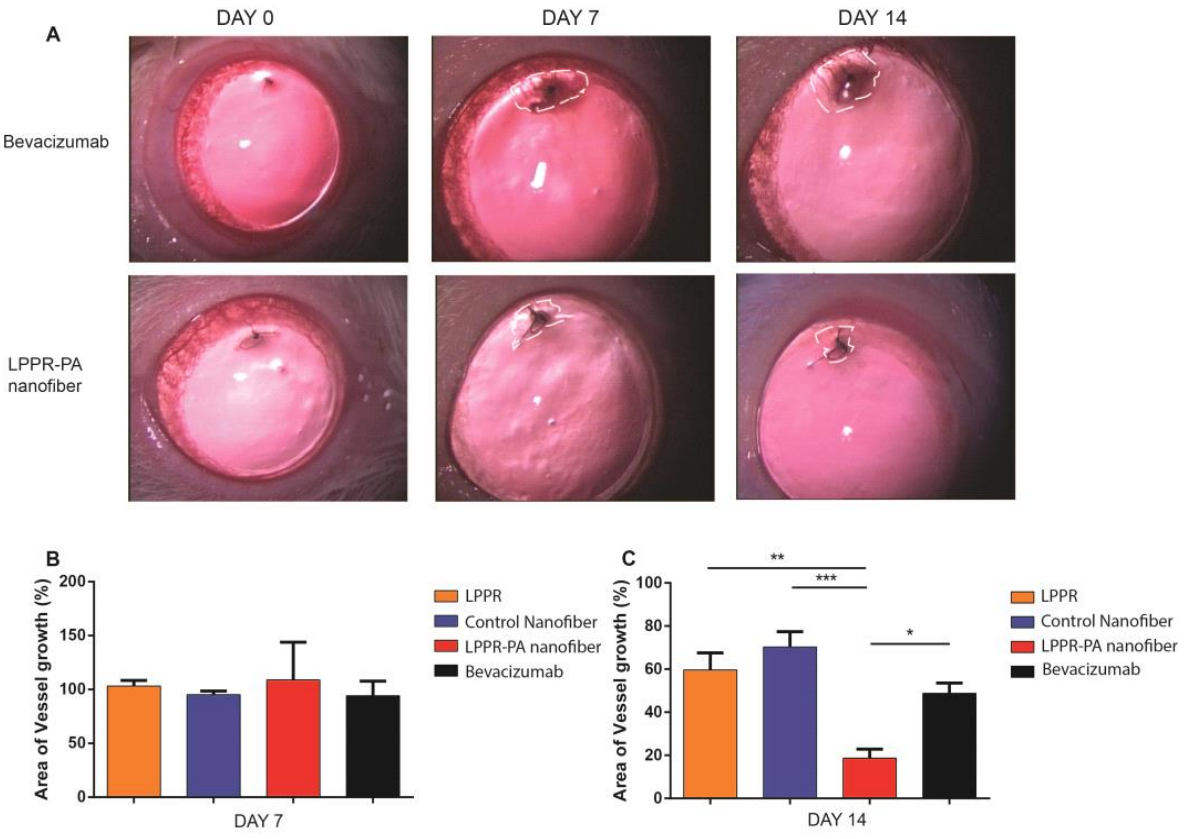

Figure 4.12 Inhibitory effect of LPPR-PA nanofibers on suture-induced corneal neovascularization in rats. Images of corneas treated with bevacizumab and LPPR-PA nanofiber were taken at day 0, 7 and 14 (A). Suture induction resulted in intensive neovascularization, which had similar vessel growth area on each group at day 7 (B). Reduced neovascularization was detected in LPPR-PA nanofiber-injected rats compared to other treatment groups. Quantification of vessel areas showed that the most significant inhibition of vascularization is found in the anti-angiogenic nanofiber treated group (B). One-way ANOVA analysis was performed at * $p< 0.05$, ** $p < 0.01$, and *** $p < 0.001$.

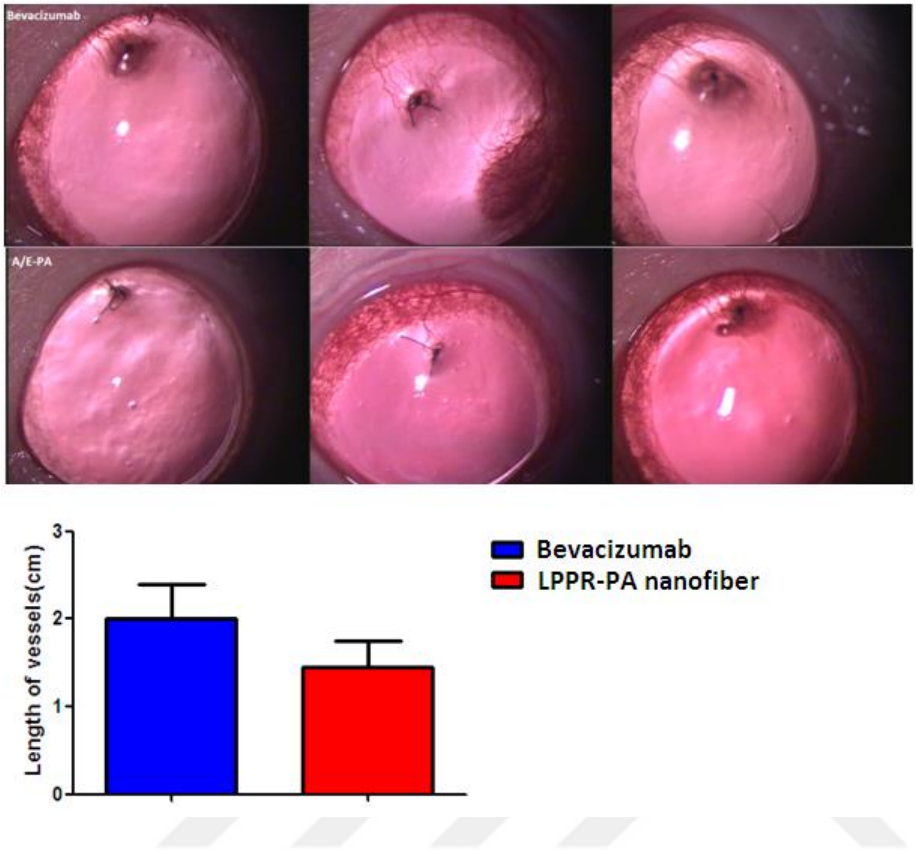

Figure 4.13 Imaging and measurement of length of blood vessels in bevacizumab and LPPR-PA nanofiber treated rat eyes. LPPR-PA nanofiber was effective as bevacizumab treatment.

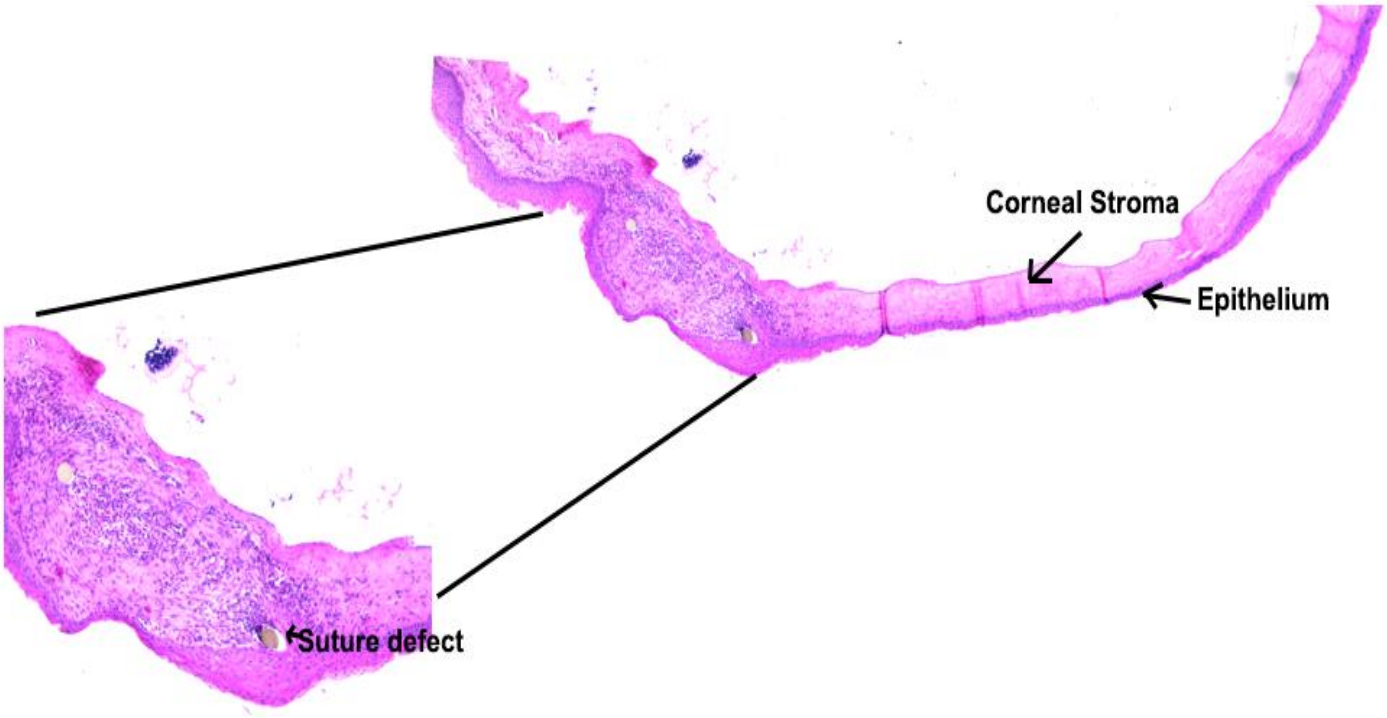

Figure 4.14 Hematoxylen and eosin staining of corneal tissue sections. Suture induction caused an injury on stroma. Abnormalities due to formation of blood vessels cause disruption of corneal stroma and epithelium.

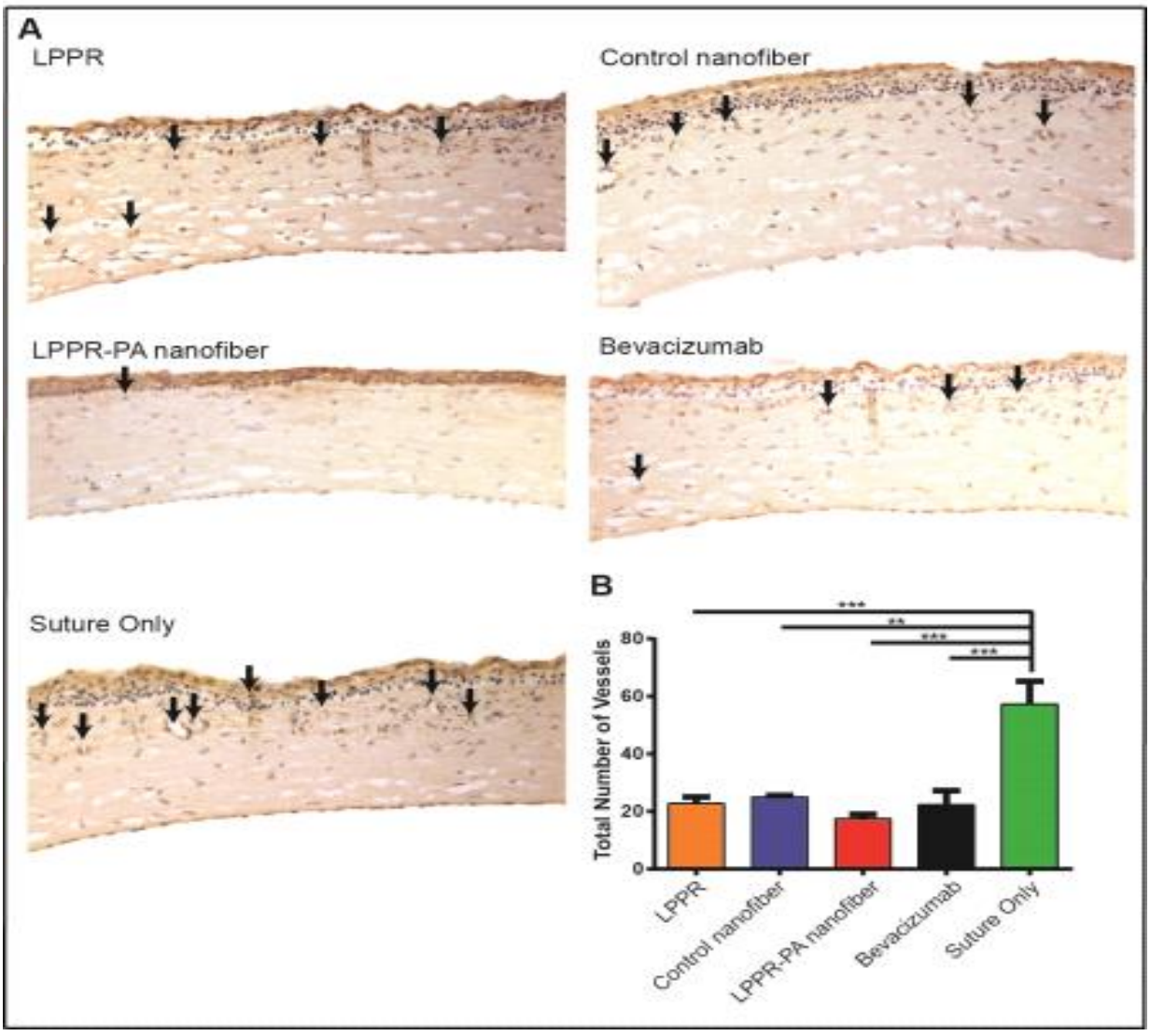

Figure 4.15 LPPR-PA nanofiber treatment inhibits corneal neovascularization. Histological (A) and quantitative (B) analysis of the cornea revealed that all treatments led to a significant reduction in the number of blood vessel when compared with the suture-only control. One-way ANOVA analysis was performed at * $p < 0.05$. Representative images of von Willebrand Factor (brown) staining of corneal tissue sections and hematoxylin-blue counterstaining of nuclei (blue). Arrows show blood vessels on corneal stroma.

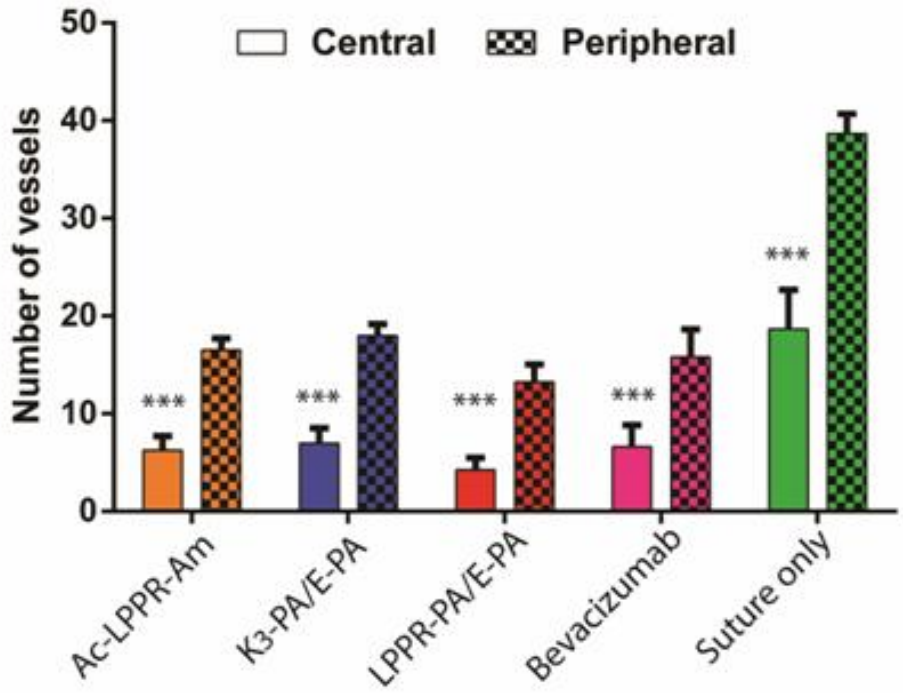

Figure 4.16 Number of vessels found in central and peripheral area of cornea. The distribution of blood vessels accumulates in central area in all groups. This phenotype is result of suture induced model.

4.4. Discussion

Disruption of aberrant VEGF signaling is the most common strategy for the treatment of corneal neovascularization, which aims to facilitate the regression and elimination of abnormal blood vessels. Since the angiogenic activity of VEGF is mediated by its receptors, the blocking of receptor-ligand interactions is a promising approach for anti-VEGF therapies. In this study, the LPPR sequence was incorporated into a peptide amphiphile sequence capable of self-assembling into a transparent and mechanically stable nanofiber matrix [24]. The LPPR-PA molecule contains hydrophilic head and hydrophobic tail regions, which mediate self-assembly through both electrostatic interactions and hydrophobic collapse to form ordered structures. The mixing

of LPPR-PA with oppositely charged E-PA formed stable nanofibers. TEM and CD analyses of peptide amphiphiles confirmed that the PA molecules formed β-sheet-rich nanofiber structures (Figure 3.4). The bioavailability and biocompatibility of peptide assemblies are critical for designing nanotherapeutic systems, and factors such as concentration, hydrogen bonding and charge may severely affect the biocompatibility of peptides [25, 26]. Consequently, the biocompatibility of the PA nanofibers was investigated using Live-Dead assay and both LPPR-PA and controls were found not to be toxic to cells at a concentration of 100 μM.

Anti-angiogenic properties of LPPR-PA nanofibers were investigated *in vitro* by cell proliferation, migration and tube formation assays. LPPR-PA nanofiber had significant inhibitory effect on cell proliferation in a dose-dependent manner. In contrast, the soluble LPPR peptide inhibited cellular growth only to a lesser extent, possibly because the nanofibrous architecture of peptide amphiphile systems improves the efficiency of the bioactive sequence by mediating its presentation to NRP-1. The binding of VEGF to NRP-1 was reported to be essential for VEGF-induced cell migration; consequently, an *in vitro* scratch wound healing assay was performed to examine the role of the LPPR sequence on cell migration [27, 28]. LPPR-PA nanofiber treatment was found to significantly inhibit wound closure by HUVECs in 24 h, suggesting that the bioactive nanofibers are able to effectively prevent VEGF-induced cellular migration. While a transwell migration assay would further support these results, the occlusion of transwell pores by the peptide prevents its application for the analysis of the present system. Although migration was markedly inhibited by the LPPR-PA nanofiber, the control nanofiber also surprisingly exhibited a suppressive effect compared to TCP. This effect may have been caused by the multivalent presentation of charged residues on peptide nanofibers, which can limit the migration of endothelial cells and allow control nanofibers to display some measure of anti-angiogenic

effect. HUVECs form capillary-like tubes when stimulated with angiogenic factors, and this property can be used to assess the anti-angiogenic properties of a broad variety of materials [29]. The angiogenesis assay demonstrated that peptide nanofiber treatment significantly reduced tube formation in the presence of VEGF, exhibiting a suppressive effect comparable to the commercially available drug bevacizumab. Control nanofibers also exhibited an inhibitory effect on tube formation, which normally requires the clustering of endothelial cells and may have been blocked by the prevention of cellular migration induced by control peptides.

While peptide sequences (including the LPPR motif) have previously been reported to inhibit endothelial cell proliferation and tube formation; peptide nanofibers described in the present study were observed to inhibit corneal angiogenesis to a greater extent than the soluble peptides, potentially because of the ability of well-organized peptide nanofibers to present their bioactive sequences in a coordinated and multivalent manner [14, 17]. In addition, peptide network treatment resulted in a substantially greater reduction in blood vessel numbers compared to the commercially available drug bevacizumab, suggesting that the LPPR-PA nanofiber system may be utilized as a novel therapeutic agent against corneal neovascularization.

The efficacy of nanofiber peptide treatment in cornea was investigated *in vivo* by using suture-induced angiogenesis model. This model is well-established in rats, sees widespread use in neovascularization research and has been shown to provide a quantitative and reproducible assessment of *in vivo* angiogenesis [30-32]. *In vivo* studies showed that LPPR-PA reduced corneal neovascularization more effectively than bevacizumab. This result was supported through the quantification of the number of blood vessels by the von Willebrand staining of corneal tissue sections. However, while we have demonstrated that LPPR-PA nanofibers inhibit

angiogenesis *in vitro* and reduce corneal vascularization *in vivo*, further studies are necessary to confirm the effectiveness of the material as a therapeutic agent.

It is well-known that the maintenance of the avascular and transparent structure of the cornea depends strongly on the balance between angiogenic and anti-angiogenic factors, and that VEGF plays a crucial role in this process. Due to its strong and highly specific affinity to VEGF, LPPR-PA might be utilized for the treatment of excessive vascularization associated with this growth factor. However, in disorders involving multiple growth factors, treatment with other anti-angiogenic molecules, such as anti-IGF-1 (Insulin-like growth factor-1), anti-PDGF (platelet derived growth factor), PEDF (pigment epithelium-derived factor) and endostatin, may be combined with LPPR-PA application for better prognosis.

4.5. Conclusion

Corneal neovascularization is associated with severe visual impairment and its rapid and effective treatment is of great importance for restoring the sight of the affected. The peptide nanofiber system described in the present study is able to reduce corneal blood vessel areas even after extensive vascularization had already taken place, and was as effective as a commercial agent in this capacity. Comparison of LPPR-PA nanofiber and LPPR peptide treatments suggested that the nanofiber form is more effective in reducing angiogenesis than the soluble peptide, possibly because of the ordered organization of the bioactive sequences in peptide nanofibers. A sustained release effect may also be responsible for this phenomenon, as the soluble peptide may dilute out of the cornea with time. Overall, data from a variety of *in vitro* and *in vivo* experimental approaches suggest that LPPR-PA nanofibers effectively inhibit endothelial cell proliferation and migration, aberrant capillary formation and neovascularization

in the eye, and may be utilized as a novel treatment against corneal neovascularization and possibly other angiogenesis-related disorders.

4.6. Experimental Section

4.6.1. Materials

All 9-fluorenylmethoxycarbonyl (Fmoc) and tert-butoxycarbonyl (Boc) protected amino acids, [4-[α-(20,40-dimethoxyphenyl) Fmoc-aminomethyl]phenoxy]acetamidonorleucyl-MBHA resin (Rink amide MBHA resin), Fmoc-Asp(OtBu)-Wang resin were purchased from NovaBiochem. 2-(1H-Benzotriazol-1-yl)-1,1,3,3-tetramethyluronium hexafluorophosphate (HBTU) was purchased from ABCR. Antibodies were purchased from Abcam and Millipore. Matrigel™ (growth factor reduced) was purchased from BD Biosciences (356230), Live-Dead viability assay kit from Thermo Fisher Scientific (L3224) and ELISA-based BrdU proliferation assay kit from Roche (11647229001). All other materials were obtained from Invitrogen, Fisher, Merck, Alfa Aesar, and Sigma-Aldrich. All materials were analytical grade.

4.6.2. Peptide synthesis and nanofiber formation

Peptide amphiphile (PA) molecules used in this study were synthesized by solid phase peptide synthesis. Rink amide MBHA resin (for Ac-LPPR-Am, LPPR-PA and K_3-PA synthesis) and Fmoc-Glu(OtBu)-Wang resin (for E-PA synthesis) were used as solid support. Coupling reactions of amino acids were performed with 2 equivalents of Fmoc protected amino acid, 1.95 equivalents of HBTU and 3 equivalents of N,N-diisopropylethylamine (DIEA) in DMF for 3 h. Fmoc removals were performed with 20% piperidine/dimethylformamide (DMF) solution for 20 min.

All peptides were cleaved from the resin using a mixture of trifluoroacetic acid (TFA), triisoproplysilane (TIS), and water at a ratio of 95: 2.5: 2.5 for 2.5 h. Excess TFA was removed by rotary evaporation and the sample was triturated with ice-cold diethyl ether. Diethyl ether was then removed and the pellet was dissolved in water for freeze-drying. Peptide samples were analyzed and purified by reverse phase preparative HPLC on an Agilent 6530 Accurate-Mass Q-TOF LC/MS equipped with an Agilent 1200 HPLC.

The bioactive LPPR-PA nanofiber was formed by mixing LPPR-PA and E-PA at a 1:1 molar ratio, while the non-bioactive K_3-PA/E-PA control nanofiber was similarly formed by mixing K_3-PA and E-PA at a 1:1 molar ratio. Net charges were +1 for both nanofibers and LPPR peptide (Fig. S1). Peptide mixtures and solutions were adjusted to pH 7.4 prior to use.

Circular dichroism (CD) measurements were carried out at 100 μM peptide concentrations in a 1-mm path length quartz cuvette. Measurements were acquired at room temperature at 500 nm/min scanning speed, 1 nm bandwidth and 0.1 nm data pitch using a J-815 Jasco spectrophotometer. The 190-300 nm spectral regions were monitored for the analysis of the secondary structures of peptides.

Transmission electron microscopy (TEM) and scanning transmission electron microscopy (STEM) samples were prepared at a final concentration of 100 μM of mixtures of positively and negatively charged peptides. 5 μL of samples were cast onto TEM grids and incubated for 5 min. Samples were then stained with 2 wt % uranyl acetate solution and washed twice with a drop of MilliQ water. Imaging was performed by using a FEI Tecnai G2 F30 TEM with electron energy of 100 kV.

4.6.3. *In vitro* cell culture studies

Human umbilical vein endothelial cells (HUVECs) were cultured in a humidified, 37 °C, 5% CO_2 incubator using 75 cm^2 polystyrene cell culture flasks containing low glucose Dulbecco's modified Eagle's medium (DMEM) supplemented with 10% fetal bovine serum (FBS, Gibco), 1% penicillin/streptomycin (P/S) and 2 mM L-glutamine.

Viability of HUVECs on soluble nanofibers was tested using Live-Dead viability assay. HUVECs were seeded in 96-well plates at a density of 2 x 10^3 cells/well. After 24 h of peptide incubation, cells were stained with Calcein AM and ethidium homodimer reagents at 2 μM and 4 μM concentrations, respectively. After 30 min of incubation, cells were observed under fluorescence microscope, and live and dead cells were counted with ImageJ (NIH) software. Viability was assessed by calculating the ratio of live cells to total cell numbers. Experiments were carried out with n = 4 and images were taken from 5 different locations per well.

Binding of LPPR-PA to HUVECs was detected with FITC conjugated K_3-PA. LPPR-PA nanofiber solution was mixed with FITC-labeled K_3-PA. Solutions were prepared as previously described [41]. HUVECs were seeded on 24 well plate and treated with 100 μM mixture of LPPR-PA and FITC-K_3-PA for 24 h. HUVECs were fixed in 4% parafolmaldehyde for 15 min and permeabilized with 0.1% Triton X-100. Cells were counterstained with 1 μM TO-PRO-3 (Invitrogen) in PBS for 10 min and mounted with ProLong® gold Antifade Reagent (Invitrogen). Samples were imaged by confocal microscopy (Zeiss LSM510) with the appropriate configurations for FITC (488 nm ex. laser/505-530 nm band pass emission filter).

Cell proliferation was evaluated using a colorimetric ELISA-based BrdU assay (Cell Proliferation ELISA, BrdU; Roche) according to the manufacturer's instructions. Briefly,

HUVECs were seeded onto a 96-well plate at a density of 5×10^3 cells/well. Cells were subsequently incubated with VEGF (100 ng/mL) in the presence or absence of peptides for 24 h at 37 °C, and the extent of BrdU incorporation was quantified by spectrophotometry. Each group was tested at least in triplicate, and the assays were repeated a minimum of three times. The IC_{50} of cell proliferation was calculated by taking untreated cells as maximum and using the GraphPad program.

For *in vitro* scratch wound healing assay, HUVECs were incubated with 100 µM of peptides for 24 h. 5 x 10^4 HUVECs per well were seeded in 24-well plates and grown into a monolayer culture with 100% confluency. After scratching through the monolayer with a pipette tip, wound closure was visually monitored with a Zeiss Axio Scope Inverted Microscope and the ability to recover from wounds (% closure) was quantified using proprietary software associated with the microscope system.

In vitro angiogenesis/tube formation assays were performed as previously described [18]. Briefly, the impact of peptide hydrogel formulations on *in vitro* angiogenesis was tested using HUVECs (4 x 10^4 cells/well) seeded in Matrigel™ (50 µL) coated chambered slides (96-well) containing 100 µM of peptide samples, with TCP utilized as control. HUVECs were incubated at 37 °C for approximately 6 h, and capillary-like structures were imaged using a Zeiss Axio Scope Inverted Microscope.

4.6.4. Animal models

All procedures involving animal experiments were approved by Gazi University Animal Ethics Committee. Suture-induced corneal angiogenesis was used as the neovascularization model, since the cornea is normally an avascular tissue and, therefore, serves as an ideal *in vivo* model for studying the effects of angiogenesis.

Adult male Sprague–Dawley (SD) rats were exposed to 12 h light-dark cycles and fed a standard laboratory diet with food and water provided *ad libitum*. All rats (weighing 200–220 g and aged 8 weeks) were deeply anesthetized prior to surgery. 10-0 nylon sutures were placed at 1-1.5 mm distance from the temporal limbus of the cornea, and the time of suture placement was considered as day 0. The suturing operation was performed on only one eye, while the other eye of the animal was left as internal control. Following suture placement, rats were randomized to five groups: Group I (n=4) treated with Ac-LPPR-Am, Group II (n=4) treated with K_3-PA/E-PA, Group III (n=4) treated with LPPR-PA/E-PA, Group IV (n=4) treated with bevacizumab and Group V (n=4) without any treatment (suture-only group). Corneas were observed for 7 days following the operation to ensure that the suture is successful in stimulating corneal neovascularization; only animals exhibiting neovascularization were subjected to further treatment. LPPR-PA nanofibers and control peptides were delivered to rat corneas by subconjunctival injection (1 cc of 1mM peptides) on day 7. Similarly, group IV received a subconjunctival injection of 0.1 cc bevacizumab (Avastin®) at a concentration of 25 mg/mL on day 7. Corneal images were taken using a surgical microscope on day 0 (operation day), day 7 (injection day), and day 14. Images were used to measure the corneal surface covered with neovascular vessels. To increase reproducibility, the entire surgery process was performed by a single investigator (B.A.) for every animal. Pupils were dilated with drops of tropicamide 0.5% (Tropamid®) prior to each imaging session [19]. Neovascularization of each cornea was evaluated by an examiner who was blind to the treatment groups. Corneas were then removed and processed for further histological analysis.

4.6.5. Histological analysis

On day 14, all rats were sacrificed and their eyes were fixed with 10% formalin and embedded in paraffin. Tissue sections (5 µm), which were taken with a Leica microtome, were deparaffinized in xylene, rehydrated through graded alcohols to distilled water, and stained with hematoxylin and eosin (H&E). Endogenous peroxidase was inactivated with 3% hydrogen peroxide for 10 min at room temperature, and nonspecific binding sites were blocked with 10% normal goat serum for 2 h. Antigens were then detected through indirect binding using their respective primary antibodies and HRP-conjugated secondary antibodies. Serial sections were immunolabeled with anti-von Willebrand factor antibody (1:400 dilution; ab6994, Abcam), and a secondary antibody (1:500 dilution; ab6721) to evaluate neovascularization. Sections were developed in 3,3'-diaminobenzidine (DAB) and counterstained with hematoxylin.

The number of blood vessels was counted from at least 6 randomly selected fields in each section. Sections were immunolabeled with anti-von Willebrand factor antibody and quantified by two independent observers under 200x magnification. Quantifications were performed by the ImageJ analysis system to calculate the number of vessels in each field.

4.6.6. Statistical Analysis

Statistical analyses were performed using GraphPad Prism 5. One-way ANOVA was used to compare the differences between the groups and Bonferroni's multiple comparisons test was used for post-hoc correction. Error bars indicate as ± SEM (standard error of mean). At least three independent repeats were performed for each *in vitro* experiment, with a minimum of n = 3 for each repeat. *In vivo* experiments were performed at a minimum of n = 4.

Chapter 5

Antibacterial Activity and Mechanical Effects of Black Silicon Surfaces on Mesenchymal Stem Cell Differentiation

5.1. Objective

Microbial contamination of surfaces is a major challenge in healthcare, medical devices and food industries. Black silicon surfaces are inspired from the wings of the dragonfly *Diplacodes bipunctata* and are highly hydrophobic. It exhibits a bactericidal effect due to its structure rather than chemical composition and kills bacterial cells through mechanical effects. Here, we investigated the antibacterial properties of black silicon on gram-positive and gram-negative bacteria via live/dead assay. Our cell toxicity assay showed that black silicon surfaces present anti-bacterial properties. This biomimetic surface is favorable due to its ease of coating. Furthermore, we investigated the response of mesenchymal stem cells (MSC) on black silicon surfaces with a range of 5 to 30 µm pillar size. Alizarin red staining of MSCs, which is an indicator of calcium deposition and osteogenic differentiation, did not show any differences on day 7. However, further analyses, such as alkaline phosphatase (ALP) activity and alizarin red stainings on day 14 and 28, are required for the detection of mechanical effects on MSCs.

5.2. Introduction

The ideal structure of a black silicon surface contains silicon pillars with slightly trapezoidal cross sections separated by pores with certain distances. These nanoscale spike structures give very low reflectivity, and black silicon is therefore a very favorable material for antireflection layers on solar cells [42]. In addition to its usage in solar cell technology, black silicon can be

used as an antibacterial surface [101]. In recent years, antibiotic/antimicrobial resistances have been on the rise and were found to be a major concern for the use of long-standing antibiotics against common pathogens. The overuse of antibiotics was indicated as the main cause of the resistance [43]. Usage of agents such as surface antibacterial solutions is also very common and contributes to the antibiotic resistance of bacteria. Black silicon surface provides an antibacterial surface via mechanical effect rather than the use of any antibiotics, chemicals or toxins. Black silicon surfaces are found to be highly effective against a range of bacteria, as well as endospores [101]. They provide estimated average bacteria killing rates of up to 450,000 cells per minute of exposure per cm^2 [101]. Silicon pillars are able to cause damage to cell walls of both gram-positive and gram-negative bacteria [101]. Gram negative bacteria have relatively thinner cell walls compared to gram positive ones. Gram negative bacteria are not stained with violet dye, and their color is red or pink under gram staining. Gram positive cell walls contain peptidoglycan and teicnoic acids, and their structure is therefore thicker than gram negative bacteria, which have lipopolysaccharides and lipoproteins. In this study, antibacterial characteristic of black silicon were investigated both in gram negative (*P. aeruginosa* and *E. coli*) and positive bacteria (*S. aureus* and *B. subtilis*).

Effective biomimetic strategies for the prevention of bacterial attachment can be derived from natural materials such as the self-cleaning and antibacterial wing surfaces of odonates. Here, black silicon surface has been shown to mimic dragonfly wings with a high water contact angle. *Diplacodes bipunctata* is also known as red percher dragonfly and is a fast-moving predatory insect with an aquatic nymphal stage. The hydrophobicity of the black silicon surface depends on its roughness [44]. In the literature, the most common technique for black silicon production is reactive ion etching (RIE). This technique enables the production of regular arrays of pillars with

a wide range of diameter. Here, black silicon surfaces were produced by a wet etching technique to possess small variations in diameter.

Mesenchymal stem cells (MSC) are fibroblastoid multipotent adult stem cells with a high capacity for self-renewal. The effect of length of pillars on mesenchymal stem cell differentiation was also investigated. It is known that the topographical pattern of surfaces affects the migration, proliferation, adhesion and alignment of cells [102]. Uncontrolled cell migration is associated with a wide range of chronic diseases and cancer [103]. To understand the underlying mechanism of the effect of topographical patterns of surfaces is critical for treatment of those diseases. Moreover, the induction of mesenchymal stem cell differentiation through the osteogenic phenotype is crucial for enhancing the recovery of non-healed bones.

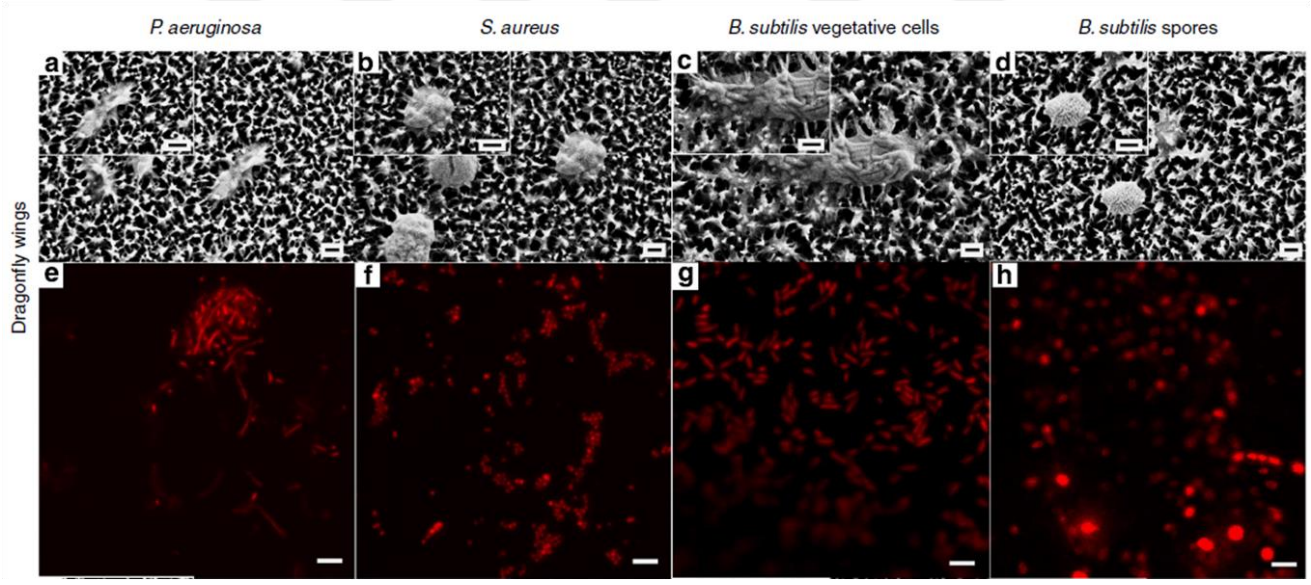

Figure 5.1 SEM images of bacteria on dragonfly wings. Confocal laser scanning micrographs confirm that gram negative and positive bacteria disruption by dragonfly wing. Dead bacterial cells were stained with propidium iodide (red) and live cells were stained with SYTO9 (green). Absence of green color indicates effectiveness of dragonfly wings [101].

5.3. Results

5.3.1. Antibacterial activity of black silicon surfaces

Black silicon surfaces with different diameters (5, 10, 15 and 30 µm) of pillars were produced by wet etching technique by Dr. Kinyas Polat. Viability of cells attached to black silicon surfaces was investigated using live/dead assay. In this assay, bacteria with intact cell membranes stain fluorescent green (SYTO9), while bacteria with damaged membranes stain red (propidium iodide). E.coli, gram negative bacteria, was incubated in LB medium on black silicon surfaces for 16 h. Since black silicon surface are super hydrophobic, they cause repulsion of LB medium in few seconds (Figure 5.4A). After few minutes of incubation, surface is covered with bacteria (Figure 5.4B). As seen in Figure 5.6, both live (a) and dead (b) cells were visualized after 16 h. A silicon wafer control surface did not kill any bacteria. These results indicated that black silicon surfaces are at least partially anti-bacterial. In this experiment, 3×10^6 cells were incubated on black silicon surface, 10 fold higher than average bacteria killing rates of dragonfly (3×10^5). Therefore, further experiments are required for calculation of killing rates of black silicon surfaces.

The transparency of LB medium indicated that number of living bacteria is lower on black silicon surfaces compared to silicon wafer control (Figure 5.5a-c). Surprisingly, color difference indicated that surface with 5 µm pillars were more toxic than 10 µm surfaces, suggest that pillar lengths affect anti-bacterial characteristic of black silicon (Figure 5.5a-b).

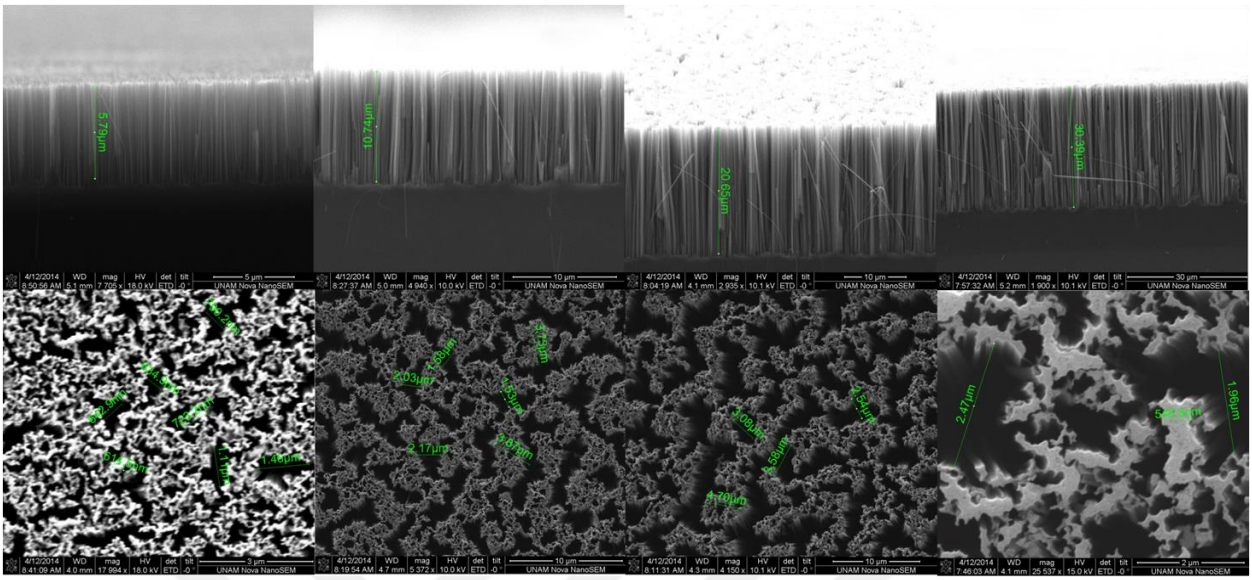

Figure 5.2 SEM images of black silicon surfaces with different pillar diameters. SEM images confirmed that wet etching techniques enables production of homogenously distributed pillar arrays with certain diameter. The diameter of pillars range between 5 to 30 µm (courtesy of K.Polat).

Figure 5.3 Bacterial cell incubation on superhydrophobic black silicon surface. E.coli culture in LB medium was added drop wise on black silicon surfaces. Although surface do not submerge into medium (left), after few minutes of incubation bacteria attach to surface (right).

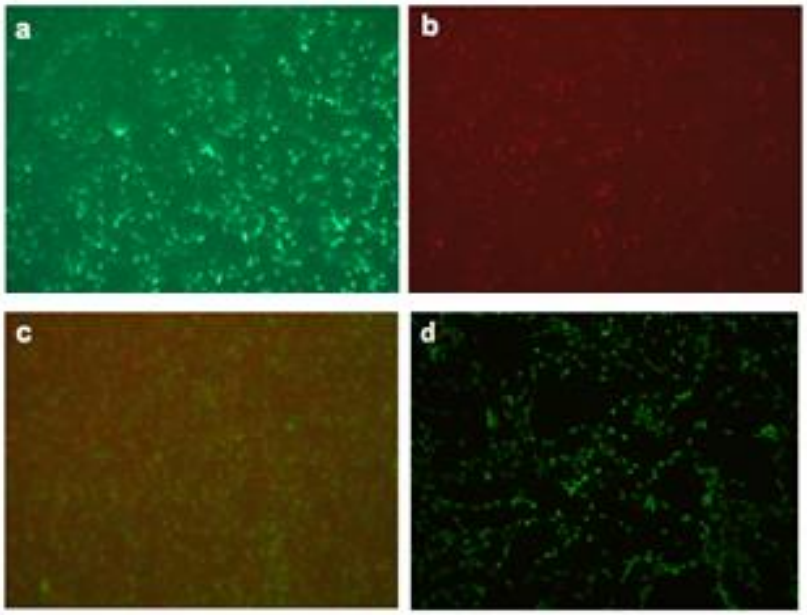

Figure 5.4 Live/dead assay of E.coli on black silicon surfaces after 16 h incubation. Green-SYTO9 (live cell) and red-propidium iodide (dead cell) staining showed that surface did not completely kill all bacteria (a, b, c). Silicon wafer was used as control (d).

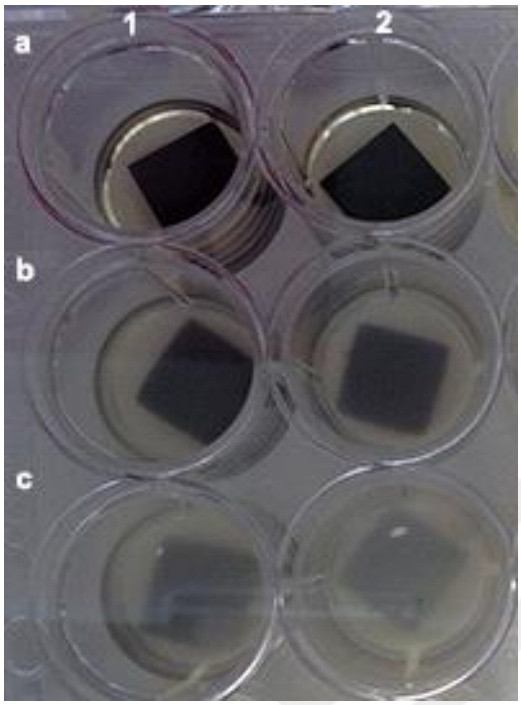

Figure 5.5 S.aerus cell incubation of black silicon surfaces after 24 h. Black silicon surfaces with 5μm (a), 10 μm and silicon wafer control. Color density of LB medium is correlated with growth bacteria number. Black silicon surfaces are less dense than silicon wafer control indicates anti-bacterial properties of surfaces.

5.3.2. Cellular viability of black silicon surfaces for HUVEC and rMSC

Measurements of cell viability of HUVECs and rMSC cells were performed with alamar blue assay. We used cells on bare tissue culture plate as a control. Relative cell viability data was normalized to TCP count as 100% (Figure 5.6 and Figure 5.7). Moreover, attachment and spreading abilities of HUVEC was examined by confocal imaging (Figure 5.6B-C). Cells were able to attach and sprout along the black silicon surface. Pillar structures with 5 μm diameter are biocompatible and did not cause any change on morphology of HUVECs.

Cellular viability assay showed that black silicon surfaces with different pillar diameters are not toxic for rMSCs (Figure 5.7). Furthermore, SEM imaging of rMSC on black silicon surfaces confirm the cell attachment on surface (Figure 5.10). During the production of black silicon surfaces complication of wet etching technique causes polydispersity of pillars on surface. Defects on some samples were detected with SEM imaging (Figure 5.9). Those defects disrupt homogeneity of the surface and might affect cellular behavior of rMSCs.

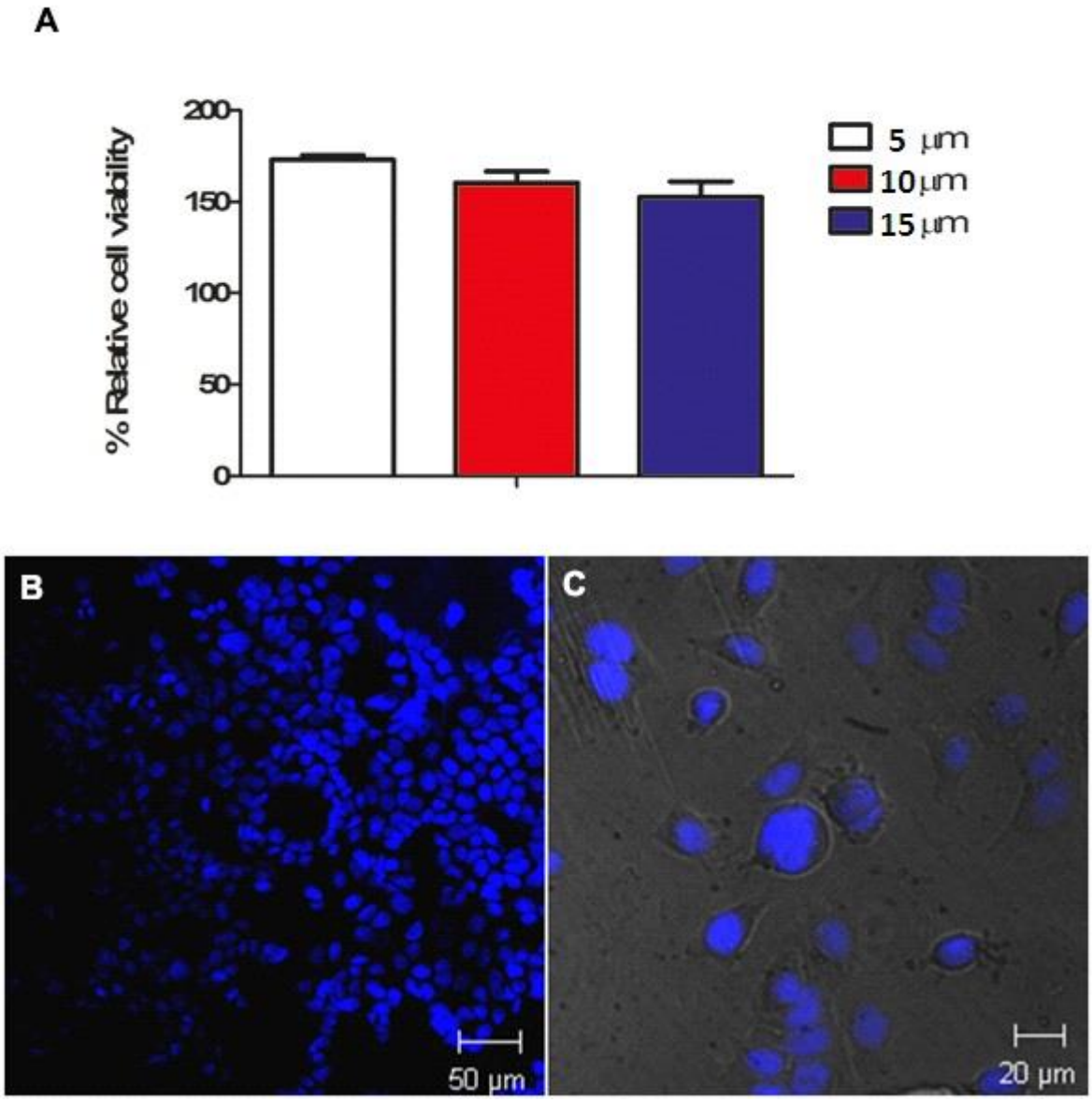

Figure 5.6 Viability analysis of HUVECs on black silicon surfaces with different pillar lengths. Cellular viability was quantified with alamar blue assay after 24 h (A: white; 0.5 µm, red; 1 µm, blue; 1.5 µm). Confocal imaging of HUVECs; TO-PRO-3 staining (B: nuclei; blue) and merge with DIC imaging (C) indicate that cells adhere and sprout on black silicon surface.

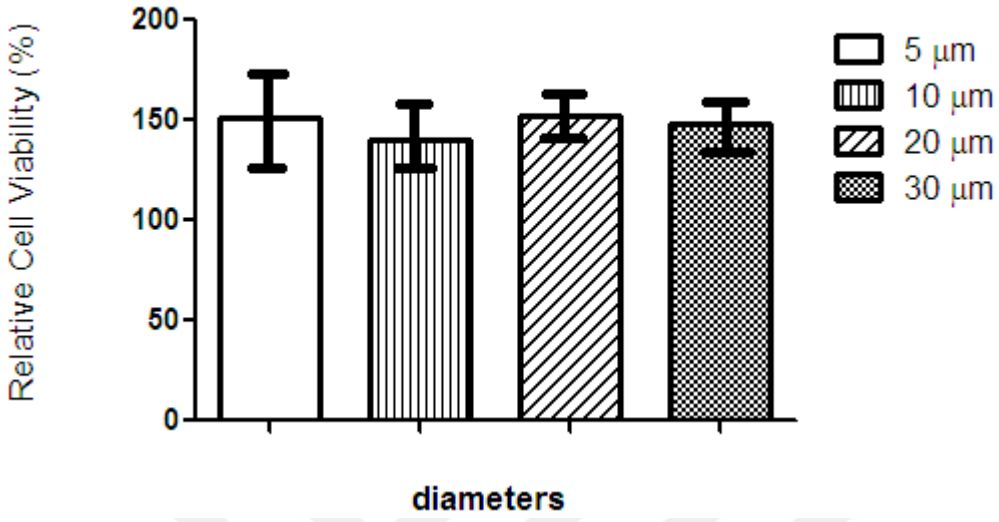

Figure 5.7 Relative cell viability of rMSCs on black silicon surfaces after 24 h. Alamar blue assay showed that black silicon surfaces are not toxic for rMSCs.

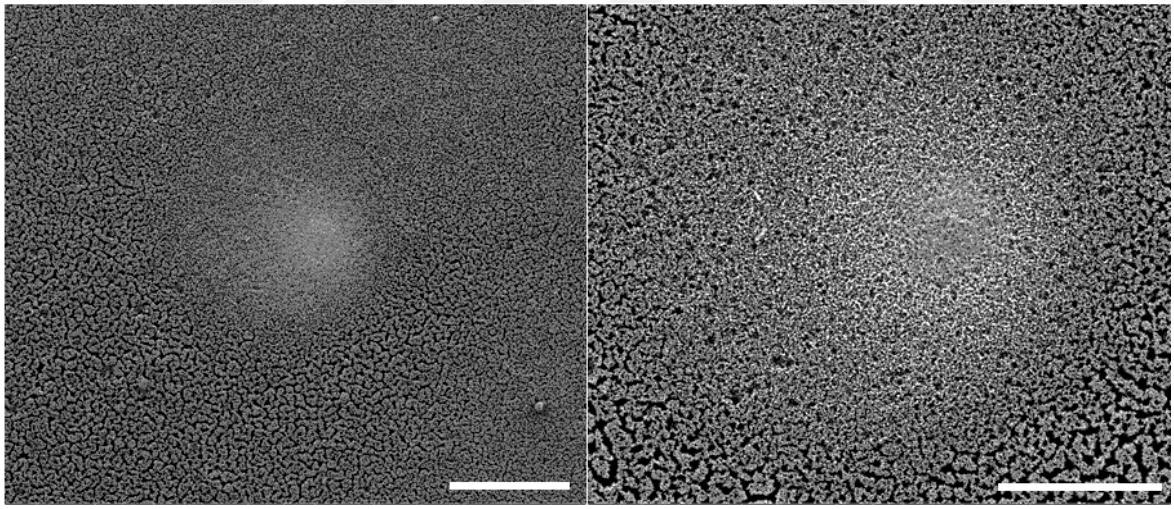

Figure 5.8 Top view of black silicon surface by SEM imaging. The distance between pillars is not homogenously distributed all around the surface. Bright area indicates density of pillar, accumulate in the middle. Scale bars are 100 and 50 µm, respectively.

5.3.3. Mesenchymal stem cell differentiation

Mesenchymal stem cells were incubated on black silicon surfaces at a density of 3 x 10^3 cells/cm^2. Alizarin red staining was performed for detection of osteogenic differentiation. Measurement of absorbance at 562 nm did not show any difference between groups (Figure 5.9). Moreover, SEM imaging showed that rMSCs still attach the surface on day 7. EDX analysis was performed for detection of calcium mineral deposition. However, calcium mineral were not detected on surface (Figure 5.11). These data are consisted with Alizarin red staining results. Since day 7 is early time point for osteogenic differentiation, calcium deposition was investigated on day 14 in normal medium. MSCs did not show any osteogenic activity on black silicon surfaces (5 µm and 10 µm) compared to silicon wafer control (Figure 5.12).

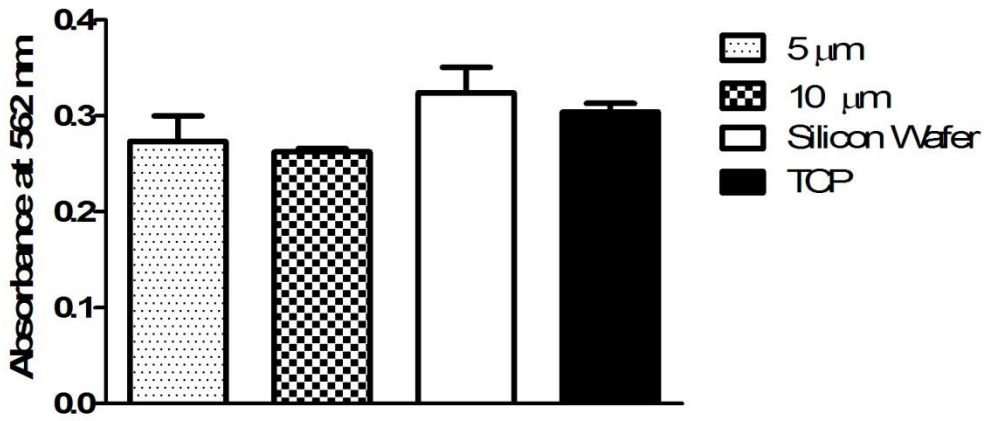

Figure 5.9 Alizarin red staining quantification of rMSCs on black silicon surface and controls. No significant difference was found between groups.

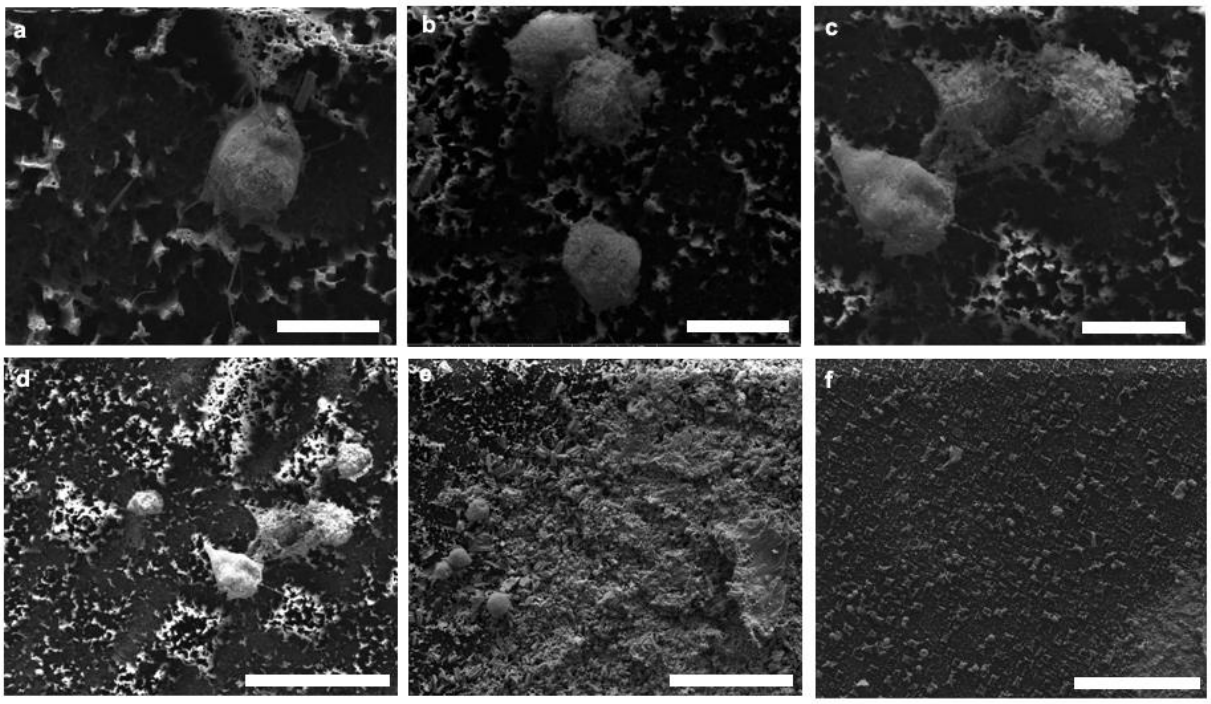

Figure 5.10 SEM imaging of rMSC incubated on black silicon surfaces after 7 days. Cellular attachment was confirmed with SEM imaging. Scale bars are 10 µm (a,b,c), 30 µm (d), 50 µm (e), 200 µm (f).

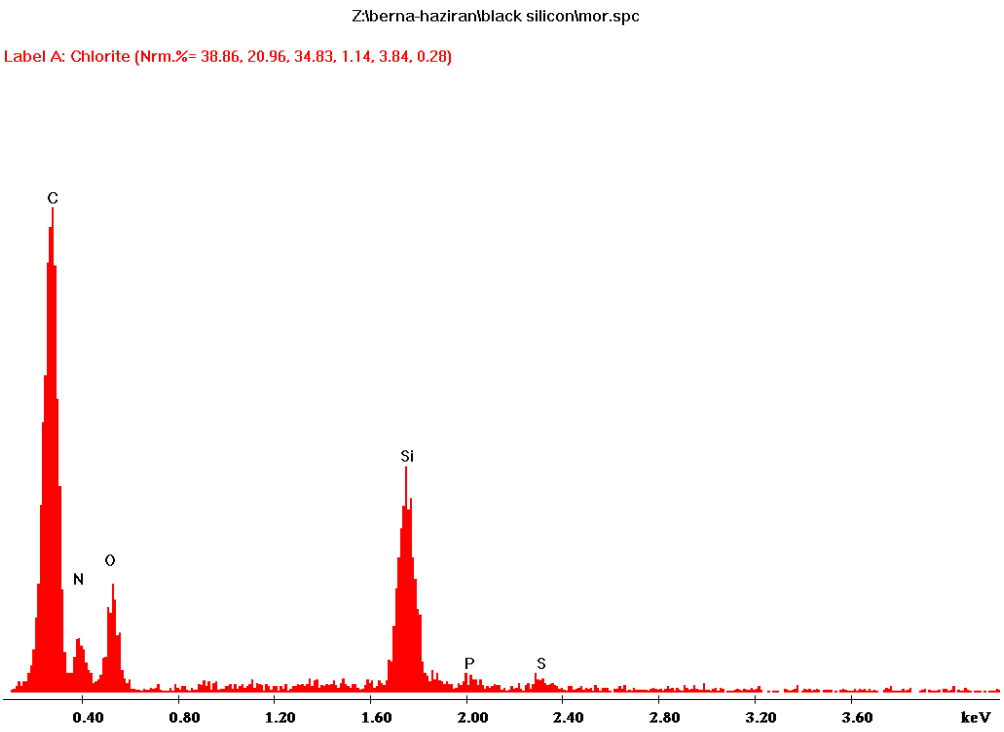

Figure 5.11 EDX analysis of mineral content of on rMSC incubated black silicon surface.

Calcium mineral did not detect on surface.

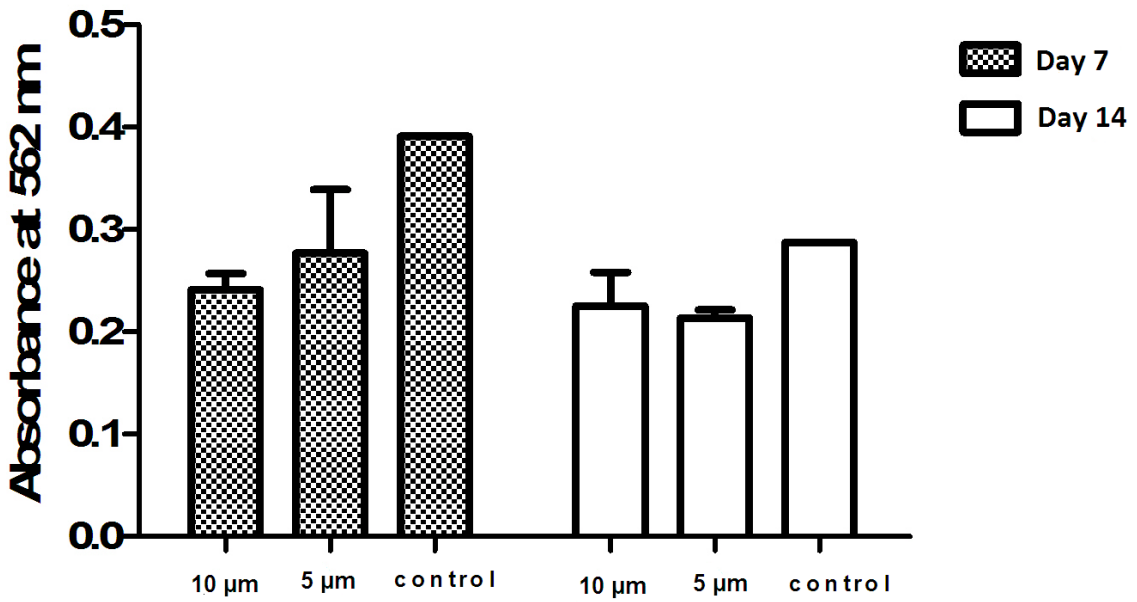

Figure 5.12 Alizarin red staining measurement of rMSCs on day and 14 in normal medium.

5.4. Discussion

The hydrophobic surface generally refers to a surface with a water contact angle larger than 90°. When a surface has a water contact angle larger than 150°, it is called a superhydrophobic surface. In this study, black silicon surfaces are superhydrophobic, therefore at the beginning of bacterial incubation none of the bacteria bind to surface. However, after a few minute of incubation bacteria formed fibers to attach to surface. The observable difference between bacterial toxicity of pillars with 5 µm and 10 µm diameter, indicated that pillar size might affect the anti-bacterial activity of surfaces. In order to confirm that, cell viability experiment should be performed with higher pillars as well. The killing rate of bacteria should be also calculated for each bacterial strain.

Cell morphology of black silicon surfaces did not show any effect on early osteogenic induction on rMSCs. However, homogeneity of the distribution of pillars is critical for detection of cell behavior. Defects on black silicon surfaces should be eliminated in production step. Furthermore, for late osteogenic induction, Alizarin red staining and alkaline phosphotase activity should be perfomed on day 28.

5.5. Conclusion

In this study, potential anti-bacterial activity of black silicon surfaces produced with different etching techniques was investigated. Cellular toxicity results showed that black silicon surfaces are able to kill both gram negative and positive bacteria. The length of pillars is critical for anti-bacterial activity of black silicon surfaces. These results indicate that black silicon has a high potential for use in coating to create an anti-bacterial surfaces. The effect of topographical pattern of surfaces on cell behavior and differentiation must be further analyzed.

5.6. Experimental Section

5.6.1. Colony forming unit (cfu) calculation

Gram negative and positive bacteria were cultured for 24 h before plated onto agar. The colony forming unit was calculated with following formula.

CFU = (number of colony x dilution factor) / volume plated in mL

5.6.2. Bacterial growth conditions and cultivation

LB agar was prepared by mixing of 5 g NaCl, 5g Tryptone, 2.5 g yeast extract, 7.5 g agar in 500 mL of distilled water. LB medium was autoclaved and cool to 55 °C near Bunsen burner. Four bacteria strains were used in experiments, *P. Aeruginosa, S. Aureus, B. subtilis* and *E.coli*. Bacterial suspensions were grown overnight at 37 °C with agitation.

Name of Bacteria	Gram Positive	Gram Negative	OD600 Value
P. Aeruginosa		*	0.3
S. Aureus	*		0.3
B. subtilis	*		0.3
E.coli		*	0.3

Table 5.1 Gram positive and negative bacteria with OD600 values.

5.6.3. Live/Dead assay for bacteria

LIVE/DEAD BacLight Bacterial Viability Kit, L-7012 was purchased from Life Technologies. Kit contains SYTO 9 for live cells and propidium iodide for dead cell staining. 6 µM of SYTO9 and 30 µM of propidium iodide were prepared in 1X PBS. Samples were stained for 15 min at room temperature. Stained bacterial suspension (5 µL) was traped between slide and coverslip, and visualized with confocal microscope. The excitation/emission maxima for these dyes are around 480/500 nm for SYTO stain (green) and 490/635 nm for propidium iodide (red).

5.6.4. SEM imaging and EDX analysis of cells on black silicon surfaces

The morphology and spreading of HUVECs were examined by SEM imaging by using an ETD detector at high vacuum mode at 5 keV beam energy. For this purpose, cells were seeded on top of black silicon surfaces at a density of 2×10^3 cells/cm^2. After 24 h of incubation, cells were rinsed with PBS and fixed with 2% gluteraldehyde/PBS and 1 wt% OsO_4 for 1 h each, respectively. Fixed cells were washed with water and then dehydrated sequentially in 20%, 40%, 60%, 80%, and 100% ethanol. Samples were critical point dried with Autosamdri-815B

Tousimis and coated with 6 nm Au−Pd before imaging. EDX analysis was performed to show mineral content of surfaces.

5.6.5. Alizarin red staining

Calcium deposition on the black silicon surface was measured on day 7, using Alizarin Red staining. Briefly, rMSCs were seeded on black silicon surfaces and bare silicon surfaces of 1 mm square size at a density of 3 x 10^3 cells/cm^2 in DMEM medium containing 10% FBS and 1% penicilin-streptomycin. Cells were kept growing in this medium until they reached confluency, and the medium was then replaced with fresh osteogenic medium containing 10 mM β-glycerophosphate, 0.2 mM ascorbic acid and 100 nM dexamethasone in DMEM. This medium was replenished every 2 days over the course of experiments. At predetermined time intervals, cells were fixed with ice-cold ethanol for 1 h and stained with 40 mM Alizarin-Red S for 30 min on a shaker. Samples were then washed 4-5 times with double distilled water to get rid of non-specific Alizarin red binding and calcium nodules were imaged in PBS with light microscopy. For the quantification of calcium deposition, PBS was discarded and the samples were incubated in 10% cetylpyridinium chloride for 30 min at room temperature. At the end of the incubation period, the solution was transferred to 96-well plates and absorbance measurements were performed at 562 nm. Statistical analyses were performed using one-way analysis of variance (ANOVA). p-value of less than 0.05 was considered statistically significant.

Chapter 6

Conclusion and Future Prospects

The number of studies on biomaterial-based systems enhance efficacy of revascularization therapies is increasing. In this thesis, we used peptide-based strategy depends on mimicking of natural glycosaminoglycan for induction of angiogenesis. Angiogenesis, the formation of new blood vessels from existing ones, is a complex process that is associated to many diseases including wound healing. GAG-mimetic peptide hydrogel treatment gave promising result at full thickness skin wound model of diabetic animals, but clinical studies are missing.

Future studies are needed to explore other important factors and pathways regulating angiogenesis in order to understand how it occurs during physiological wound healing. Exploration into which steps of this process fail in pathological wounds will lead to better, more directed therapies to correct affected angiogenic phenotypes. Engineering of more versatile fusion proteins that can participate in multiple aspects of wound repair while maximizing retention in the constantly changing wound microenvironment promises to be a worthwhile effort for future development. Another exciting area is the further development of biomaterial-based systems such as scaffolds that can release important factors in a time- and spatially-controlled fashion depending on the specific needs of the clinical wound. To this end, slow release from scaffold need to be integrated so that therapy can be more directed and case-specific.

Control of angiogenesis is an important process during pathologic conditions such as abnormal vessel growth in the eye and corneal neovascularization. Excessive angiogenesis is not only associated with eye diseases, but also plays critical role in the growth and spread of cancer. The growth of blood vessels is necessary for tumors to grow beyond a few millimeters in size.

Tumors can induce formation of blood vessels by releasing chemical signals that stimulate angiogenesis. The resulting new blood vessels provide oxygen and nutrients for growing tumors, allowing the cancer cells to invade nearby tissue and metastases. Since tumors cannot grow beyond a certain size or spread without a blood supply, new drugs blocking tumor angiogenesis are under investigation [104]. So far natural and synthetic angiogenesis inhibitors, also called anti-angiogenic agents, are studied with the idea that these molecules will prevent metastases of cancer. Efficacy of LPPR-PA nanofiber inhibition of corneal neovascularization enlightens possible usage of those materials as anticancer treatment. Bevacizumab is the first angiogenesis inhibitor approved by the U.S Food and Drug Administration (FDA) and is currently used for treatment of glioblastoma. It is also used in combination with other drugs to treat renal carcinoma, colorectal cancer and lung cancer. Sorafenib, sunitinib, pazopanib and everolimus are other drugs that have anti-angiogenic properties and are approved by FDA. Sorafenib, brand name Nexavar® is actively used in hepatocellular carcinoma and kidney cancer [105]. Angiogenesis inhibitors differ from cancer drugs since they inhibit formation of blood vessels rather than killing tumor cells. In invasive cancers, drugs are combined with additional therapeutic approaches such as chemotherapy. Therefore, the efficiency of anti-angiogenic agents can also be increased with additional therapies. Although, anti-angiogenic drugs are efficient on cancer therapy, they have some limitations. Besides mild side effects, inhibition of angiogenesis negatively affects normal body process such as wound healing, renal dysfunction and problems in arteries. The possible side effects of anti-angiogenic agents are still under investigation, but so far they are effective for angiogenesis related diseases.

Modern orthopaedic surgery and implants provide treatments for muscoskeletal system related injuries both in children and adults. Orthopaedic implants are mostly composed of titanium and

stainless steel because of their strength, biocompatibility and ability to line with plastic to act as artificial cartilage. Orthopaedic implants is not only a medical need but also important for reducing pain of patients. One of the complications of orthopaedic implants is infections. Microorganisms such as bacteria attach the implant surface, colonize and form biofilms [106]. Biofilm formation is mostly seen in joint prostheses, orthopedic fixation devices, pacemakers, breast implants, stents, and urinary and venous catheters [107]. When infection causes severe complications, implants have to be removed from patients. Although, usage of biosurfactants and biomolecules coatings (i.e. antimicrobial peptides) reduce adhesion of microorganisms, they are not always effective because of ability of bacteria to damage protective layer. Therefore, new approaches capable of eliminating implant infections are urgently needed. Bioinspired strategies gain more importance for next generation biomaterials that combine functional moieties from multiple sources. Black silicon surfaces inspired from nature, procure antibacterial properties via mechanical characteristic rather than usage of any chemicals. Antibacterial characteristic of black silicon produced by ion etching technique has previously been identified by Ivanova and colleagues [101]. We investigated antibacterial properties of a new black silicon surface produced with wet etching techniques which enables production of long and regular pillars. We showed that physical characteristic of pillar play important role at bacterial properties of black silicon, whereas detailed experiments are required. Black silicon surfaces have high potential as a coating material in implants.

Furthermore, mechanical effects of spike-like surface architectures on mesencymal stem cell differentiation were investigated. Implants able to promote osteogenic differentiation are crucial for rapid healing in patients with bone defect. Although, it is widely accepted that stem cell behavior is affected by adhesion and the degree of cytoskeletal tension, the role of surface

topography on the adhesion, morphology and differentiation of cells has not been well established. Studies with effects of surface morphology of widely used implant materials; titanium on differentiation of human MSC (hMSC) shows that nanoporous surface may promote early osteoblastic differentiation [108]. Roughness of biomaterials is important as surface wettability for mesenchymal cell response [109]. Nanotopographic effect of black silicon surface on motility, morphology, viability and proliferation were studied on mouse fibroblasts NIH3T3 cells [110]. They showed that the motility and morphology of cells depends on surface pattern while viability and proliferation were not affected. In our study, we found a contradictory result that cell viability is closely related to surface pattern since longer pillar caused death of cells. Studies on rMSC did not show early osteogenic differentiation on black silicon surfaces but further experiments are required for late differentiation. This study is important for understanding the mechanism of surface -stem cell interactions and moreover development of 'bio-smart' coatings that can be used on implants. Developing biomaterials with antibacterial properties and ability to induce osteogenic differentiation is crucial for designing novel implant materials and surface modifications for improved osteogenesis.

Bibliography

[1] E.A. Logsdon, S.D. Finley, A.S. Popel, F. Mac Gabhann, A systems biology view of blood vessel growth and remodelling, J Cell Mol Med 18(8) (2014) 1491-508.

[2] P. Carmeliet, E. Storkebaum, Vascular and neuronal effects of VEGF in the nervous system: implications for neurological disorders, Semin Cell Dev Biol 13(1) (2002) 39-53.

[3] F.L. Celletti, J.M. Waugh, P.G. Amabile, A. Brendolan, P.R. Hilfiker, M.D. Dake, Vascular endothelial growth factor enhances atherosclerotic plaque progression, Nat Med 7(4) (2001) 425-9.

[4] R. Khurana, M. Simons, J.F. Martin, I.C. Zachary, Role of angiogenesis in cardiovascular disease: a critical appraisal, Circulation 112(12) (2005) 1813-24.

[5] Z. Tahergorabi, M. Khazaei, Imbalance of angiogenesis in diabetic complications: the mechanisms, Int J Prev Med 3(12) (2012) 827-38.

[6] T.N. Crawford, D.V. Alfaro, J.B. Kerrison, E.P. Jablon, Diabetic retinopathy and angiogenesis, Curr Diabetes Rev 5(1) (2009) 8-13.

[7] G.E. Lang, Diabetic macular edema, Ophthalmologica 227 Suppl 1 (2012) 21-9.

[8] R. Osterby, G. Nyberg, New vessel formation in the renal corpuscles in advanced diabetic glomerulopathy, J Diabet Complications 1(4) (1987) 122-7.

[9] S.K. Kota, L.K. Meher, S. Jammula, S.V. Krishna, K.D. Modi, Aberrant angiogenesis: The gateway to diabetic complications, Indian J Endocrinol Metab 16(6) (2012) 918-30.

[10] D.C. Hancock, N.J. O'Reilly, Synthetic peptides as antigens for antibody production, Methods Mol Biol 295 (2005) 13-26.

[11] P. Chames, M. Van Regenmortel, E. Weiss, D. Baty, Therapeutic antibodies: successes, limitations and hopes for the future, Br J Pharmacol 157(2) (2009) 220-33.

[12] J. Li, M. Post, R. Volk, Y. Gao, M. Li, C. Metais, K. Sato, J. Tsai, W. Aird, R.D. Rosenberg, T.G. Hampton, F. Sellke, P. Carmeliet, M. Simons, PR39, a peptide regulator of angiogenesis, Nat Med 6(1) (2000) 49-55.

[13] Y. Hamada, H. Egusa, Y. Kaneda, I. Hirata, N. Kawaguchi, T. Hirao, T. Matsumoto, M. Yao, K. Daito, M. Suzuki, H. Yatani, M. Daito, M. Okazaki, N. Matsuura, Synthetic osteopontin-derived peptide SVVYGLR can induce neovascularization in artificial bone marrow scaffold biomaterials, Dent Mater J 26(4) (2007) 487-92.

[14] W. Arap, R. Pasqualini, E. Ruoslahti, Cancer treatment by targeted drug delivery to tumor vasculature in a mouse model, Science 279(5349) (1998) 377-80.

[15] S. Hariharan, D. Gustafson, S. Holden, D. McConkey, D. Davis, M. Morrow, M. Basche, L. Gore, C. Zang, C.L. O'Bryant, A. Baron, D. Gallemann, D. Colevas, S.G. Eckhardt, Assessment of the biological and pharmacological effects of the alpha nu beta3 and alpha nu beta5 integrin receptor antagonist, cilengitide (EMD 121974), in patients with advanced solid tumors, Ann Oncol 18(8) (2007) 1400-7.

[16] P. Khalili, A. Arakelian, G. Chen, M.L. Plunkett, I. Beck, G.C. Parry, F. Doñate, D.E. Shaw, A.P. Mazar, S.A. Rabbani, A non-RGD-based integrin binding peptide (ATN-161) blocks breast cancer growth and metastasis in vivo, Mol Cancer Ther 5(9) (2006) 2271-80.

[17] H.P. Eikesdal, H. Sugimoto, G. Birrane, Y. Maeshima, V.G. Cooke, M. Kieran, R. Kalluri, Identification of amino acids essential for the antiangiogenic activity of tumstatin and its use in combination antitumor activity, Proc Natl Acad Sci U S A 105(39) (2008) 15040-5.

[18] J. Thevenard, L. Ramont, J. Devy, B. Brassart, A. Dupont-Deshorgue, N. Floquet, L. Schneider, F. Ouchani, C. Terryn, F.X. Maquart, J.C. Monboisse, S. Brassart-Pasco, The

YSNSG cyclopeptide derived from tumstatin inhibits tumor angiogenesis by down-regulating endothelial cell migration, Int J Cancer 126(5) (2010) 1055-66.

[19] A. Starzec, P. Ladam, R. Vassy, S. Badache, N. Bouchemal, A. Navaza, C.H. du Penhoat, G.Y. Perret, Structure-function analysis of the antiangiogenic ATWLPPR peptide inhibiting VEGF(165) binding to neuropilin-1 and molecular dynamics simulations of the ATWLPPR/neuropilin-1 complex, Peptides 28(12) (2007) 2397-402.

[20] R.J. Giordano, C.D. Anobom, M. Cardó-Vila, J. Kalil, A.P. Valente, R. Pasqualini, F.C. Almeida, W. Arap, Structural basis for the interaction of a vascular endothelial growth factor mimic peptide motif and its corresponding receptors, Chem Biol 12(10) (2005) 1075-83.

[21] R. Binétruy-Tournaire, C. Demangel, B. Malavaud, R. Vassy, S. Rouyre, M. Kraemer, J. Plouët, C. Derbin, G. Perret, J.C. Mazié, Identification of a peptide blocking vascular endothelial growth factor (VEGF)-mediated angiogenesis, EMBO J 19(7) (2000) 1525-33.

[22] R.J. Giordano, M. Cardó-Vila, A. Salameh, C.D. Anobom, B.D. Zeitlin, D.H. Hawke, A.P. Valente, F.C. Almeida, J.E. Nör, R.L. Sidman, R. Pasqualini, W. Arap, From combinatorial peptide selection to drug prototype (I): targeting the vascular endothelial growth factor receptor pathway, Proc Natl Acad Sci U S A 107(11) (2010) 5112-7.

[23] P. Alessi, D. Leali, M. Camozzi, A. Cantelmo, A. Albini, M. Presta, Anti-FGF2 approaches as a strategy to compensate resistance to anti-VEGF therapy: long-pentraxin 3 as a novel antiangiogenic FGF2-antagonist, Eur Cytokine Netw 20(4) (2009) 225-34.

[24] S. Serratì, F. Margheri, M. Pucci, A.R. Cantelmo, R. Cammarota, J. Dotor, F. Borràs-Cuesta, G. Fibbi, A. Albini, M. Del Rosso, TGFbeta1 antagonistic peptides inhibit TGFbeta1-dependent angiogenesis, Biochem Pharmacol 77(5) (2009) 813-25.

[25] E.V. Rosca, J.E. Koskimaki, C.G. Rivera, N.B. Pandey, A.P. Tamiz, A.S. Popel, Anti-angiogenic peptides for cancer therapeutics, Curr Pharm Biotechnol 12(8) (2011) 1101-16.

[26] O. Benny, S.K. Kim, K. Gvili, I.S. Radzishevsky, A. Mor, L. Verduzco, L.G. Menon, P.M. Black, M. Machluf, R.S. Carroll, In vivo fate and therapeutic efficacy of PF-4/CTF microspheres in an orthotopic human glioblastoma model, FASEB J 22(2) (2008) 488-99.

[27] A.W. Griffioen, D.W. van der Schaft, A.F. Barendsz-Janson, A. Cox, H.A. Struijker Boudier, H.F. Hillen, K.H. Mayo, Anginex, a designed peptide that inhibits angiogenesis, Biochem J 354(Pt 2) (2001) 233-42.

[28] R.Q. Miao, J. Agata, L. Chao, J. Chao, Kallistatin is a new inhibitor of angiogenesis and tumor growth, Blood 100(9) (2002) 3245-52.

[29] R.H. Zha, S. Sur, J. Boekhoven, H.Y. Shi, M. Zhang, S.I. Stupp, Supramolecular assembly of multifunctional maspin-mimetic nanostructures as a potent peptide-based angiogenesis inhibitor, Acta Biomater 12 (2015) 1-10.

[30] K.G. Alberti, P.Z. Zimmet, Definition, diagnosis and classification of diabetes mellitus and its complications. Part 1: diagnosis and classification of diabetes mellitus provisional report of a WHO consultation, Diabet Med 15(7) (1998) 539-53.

[31] K. Malmberg, L. Rydén, Myocardial infarction in patients with diabetes mellitus, Eur Heart J 9(3) (1988) 259-64.

[32] P. Bao, A. Kodra, M. Tomic-Canic, M.S. Golinko, H.P. Ehrlich, H. Brem, The role of vascular endothelial growth factor in wound healing, J Surg Res 153(2) (2009) 347-58.

[33] H. Brem, M. Tomic-Canic, Cellular and molecular basis of wound healing in diabetes, J Clin Invest 117(5) (2007) 1219-22.

[34] G. Bergers, S. Song, The role of pericytes in blood-vessel formation and maintenance, Neuro Oncol 7(4) (2005) 452-64.

[35] J.M. Centanni, J.A. Straseski, A. Wicks, J.A. Hank, C.A. Rasmussen, M.A. Lokuta, M.J. Schurr, K.N. Foster, L.D. Faucher, D.M. Caruso, A.R. Comer, B.L. Allen-Hoffmann, StrataGraft skin substitute is well-tolerated and is not acutely immunogenic in patients with traumatic wounds: results from a prospective, randomized, controlled dose escalation trial, Ann Surg 253(4) (2011) 672-83.

[36] A.S. Halim, T.L. Khoo, S.J. Mohd Yussof, Biologic and synthetic skin substitutes: An overview, Indian J Plast Surg 43(Suppl) (2010) S23-8.

[37] B.A. Lodish H, Zipursky SL, Molecular Cell Biology, 2000.

[38] R. Fitzgerald, J. Steinberg, Collagen in Wound Healing: Are We Onto Something New or Just Repeating the Past?, The Foot and Ankle Online Journal 2(9) (2009).

[39] D.M. Supp, S.T. Boyce, Engineered skin substitutes: practices and potentials, Clin Dermatol 23(4) (2005) 403-12.

[40] S.T. Boyce, D.G. Greenhalgh, R.J. Kagan, T. Housinger, J.M. Sorrell, C.P. Childress, M. Rieman, G.D. Warden, Skin anatomy and antigen expression after burn wound closure with composite grafts of cultured skin cells and biopolymers, Plast Reconstr Surg 91(4) (1993) 632-41.

[41] F.T. Bosman, I. Stamenkovic, Functional structure and composition of the extracellular matrix, J Pathol 200(4) (2003) 423-8.

[42] H. Larjava, L. Koivisto, L. Häkkinen, Keratinocyte Interactions with Fibronectin During Wound Healing in: J. Heino, V.-M. Kähäri (Eds.), Cell Invasion2002.

[43] K.M. Malinda, A.B. Wysocki, J.E. Koblinski, H.K. Kleinman, M.L. Ponce, Angiogenic laminin-derived peptides stimulate wound healing, Int J Biochem Cell Biol 40(12) (2008) 2771-80.

[44] T. Hashimoto, Y. Suzuki, M. Tanihara, Y. Kakimaru, K. Suzuki, Development of alginate wound dressings linked with hybrid peptides derived from laminin and elastin, Biomaterials 25(7-8) (2004) 1407-14.

[45] S.K. Min, S.C. Lee, S.D. Hong, C.P. Chung, W.H. Park, B.M. Min, The effect of a laminin-5-derived peptide coated onto chitin microfibers on re-epithelialization in early-stage wound healing, Biomaterials 31(17) (2010) 4725-30.

[46] R. Jayakumar, M. Prabaharan, S.V. Nair, H. Tamura, Novel chitin and chitosan nanofibers in biomedical applications, Biotechnol Adv 28(1) (2010) 142-50.

[47] T. Dai, M. Tanaka, Y.Y. Huang, M.R. Hamblin, Chitosan preparations for wounds and burns: antimicrobial and wound-healing effects, Expert Rev Anti Infect Ther 9(7) (2011) 857-79.

[48] G.D. Mogoşanu, A.M. Grumezescu, Natural and synthetic polymers for wounds and burns dressing, Int J Pharm 463(2) (2014) 127-36.

[49] T. Simmons, R. Linhardt, Application of Carbon Nanotubes to Wound Healing Biotechnology In Nanomaterials for Biomedicine, American Chemical Society2012, pp. 156-174.

[50] Y. Zhang, B. Wang, X. Meng, G. Sun, C. Gao, Influences of acid-treated multiwalled carbon nanotubes on fibroblasts: proliferation, adhesion, migration, and wound healing, Ann Biomed Eng 39(1) (2011) 414-26.

[51] B. Balakrishnan, M. Mohanty, P.R. Umashankar, A. Jayakrishnan, Evaluation of an in situ forming hydrogel wound dressing based on oxidized alginate and gelatin, Biomaterials 26(32) (2005) 6335-6342.

[52] K.R. Kirker, Y. Luo, J.H. Nielson, J. Shelby, G.D. Prestwich, Glycosaminoglycan hydrogel films as bio-interactive dressings for wound healing, Biomaterials 23(17) (2002) 3661-71.

[53] R.K. Chan, P.H. Liu, G. Pietramaggiori, S.I. Ibrahim, H.B. Hechtman, D.P. Orgill, Effect of recombinant platelet-derived growth factor (Regranex) on wound closure in genetically diabetic mice, J Burn Care Res 27(2) (2006) 202-5.

[54] L. Yildirimer, N.T. Thanh, A.M. Seifalian, Skin regeneration scaffolds: a multimodal bottom-up approach, Trends Biotechnol 30(12) (2012) 638-48.

[55] R.D. Galiano, O.M. Tepper, C.R. Pelo, K.A. Bhatt, M. Callaghan, N. Bastidas, S. Bunting, H.G. Steinmetz, G.C. Gurtner, Topical vascular endothelial growth factor accelerates diabetic wound healing through increased angiogenesis and by mobilizing and recruiting bone marrow-derived cells, Am J Pathol 164(6) (2004) 1935-47.

[56] M. Komori, Y. Tomizawa, K. Takada, M. Ozaki, A single local application of recombinant human basic fibroblast growth factor accelerates initial angiogenesis during wound healing in rabbit ear chamber, Anesth Analg 100(3) (2005) 830-4, table of contents.

[57] D.C. Roy, S.J. Wilke-Mounts, D.C. Hocking, Chimeric fibronectin matrix mimetic as a functional growth- and migration-promoting adhesive substrate, Biomaterials 32(8) (2011) 2077-87.

[58] V.A. Kumar, N.L. Taylor, A.A. Jalan, L.K. Hwang, B.K. Wang, J.D. Hartgerink, A nanostructured synthetic collagen mimic for hemostasis, Biomacromolecules 15(4) (2014) 1484-90.

[59] K.C. Rustad, V.W. Wong, M. Sorkin, J.P. Glotzbach, M.R. Major, J. Rajadas, M.T. Longaker, G.C. Gurtner, Enhancement of mesenchymal stem cell angiogenic capacity and stemness by a biomimetic hydrogel scaffold, Biomaterials 33(1) (2012) 80-90.

[60] M. Mishra, H. Kumar, K. Tripathi, Diabetic Delayed Wound Healing and the Role of Silver Nanoparticles, Digest Journal of Nanomaterials and Biostructures 3(2) (2008) 49-54.

[61] S.M. Cohn, P.P. Lopez, M. Brown, N. Namias, J. Jackowski, P. Li, D. Mishkin, J.M. Lopez, U.o.M.W.S. Group, Open surgical wounds: how does Aquacel compare with wet-to-dry gauze?, J Wound Care 13(1) (2004) 10-2.

[62] Y. Barnea, J. Weiss, E. Gur, A review of the applications of the hydrofiber dressing with silver (Aquacel Ag) in wound care, Ther Clin Risk Manag 6 (2010) 21-7.

[63] E.N. Mostow, G.D. Haraway, M. Dalsing, J.P. Hodde, D. King, O.V.U.S. Group, Effectiveness of an extracellular matrix graft (OASIS Wound Matrix) in the treatment of chronic leg ulcers: a randomized clinical trial, J Vasc Surg 41(5) (2005) 837-43.

[64] J.F. Hansbrough, B. Achauer, J. Dawson, H. Himel, A. Luterman, H. Slater, S. Levenson, C.A. Salzberg, W.B. Hansbrough, C. Doré, Wound healing in partial-thickness burn wounds treated with collagenase ointment versus silver sulfadiazine cream, J Burn Care Rehabil 16(3 Pt 1) (1995) 241-7.

[65] J. Bianchi, Iodoflex and Iodosorb in the treatment of venous leg ulcers, Br J Nurs 10(5) (2001) 342-6.

[66] M.W. Tsang, W.K. Wong, C.S. Hung, K.M. Lai, W. Tang, E.Y. Cheung, G. Kam, L. Leung, C.W. Chan, C.M. Chu, E.K. Lam, Human epidermal growth factor enhances healing of diabetic foot ulcers, Diabetes Care 26(6) (2003) 1856-61.

[67] J.S. Choi, K.W. Leong, H.S. Yoo, In vivo wound healing of diabetic ulcers using electrospun nanofibers immobilized with human epidermal growth factor (EGF), Biomaterials 29(5) (2008) 587-96.

[68] S. Garcia-Filipe, V. Barbier-Chassefiere, C. Alexakis, E. Huet, D. Ledoux, M.E. Kerros, E. Petit, D. Barritault, J.P. Caruelle, P. Kern, RGTA OTR4120, a heparan sulfate mimetic, is a possible long-term active agent to heal burned skin, J Biomed Mater Res A 80(1) (2007) 75-84.

[69] G.E. Reiber, L. Vileikyte, E.J. Boyko, M. del Aguila, D.G. Smith, L.A. Lavery, A.J. Boulton, Causal pathways for incident lower-extremity ulcers in patients with diabetes from two settings, Diabetes Care 22(1) (1999) 157-62.

[70] B.A. Lipsky, A.R. Berendt, P.B. Cornia, J.C. Pile, E.J. Peters, D.G. Armstrong, H.G. Deery, J.M. Embil, W.S. Joseph, A.W. Karchmer, M.S. Pinzur, E. Senneville, Infectious Diseases Society of America, 2012 Infectious Diseases Society of America clinical practice guideline for the diagnosis and treatment of diabetic foot infections, Clin Infect Dis 54(12) (2012) e132-73.

[71] L. Prompers, N. Schaper, J. Apelqvist, M. Edmonds, E. Jude, D. Mauricio, L. Uccioli, V. Urbancic, K. Bakker, P. Holstein, A. Jirkovska, A. Piaggesi, G. Ragnarson-Tennvall, H. Reike, M. Spraul, K. Van Acker, J. Van Baal, F. Van Merode, I. Ferreira, M. Huijberts, Prediction of outcome in individuals with diabetic foot ulcers: focus on the differences between individuals with and without peripheral arterial disease. The EURODIALE Study, Diabetologia 51(5) (2008) 747-55.

[72] M. Tong, B. Tuk, P. Shang, I.M. Hekking, E.M. Fijneman, M. Guijt, S.E. Hovius, J.W. van Neck, Diabetes-impaired wound healing is improved by matrix therapy with heparan sulfate glycosaminoglycan mimetic OTR4120 in rats, Diabetes 61(10) (2012) 2633-41.

[73] K. Rajangam, H.A. Behanna, M.J. Hui, X. Han, J.F. Hulvat, J.W. Lomasney, S.I. Stupp, Heparin binding nanostructures to promote growth of blood vessels, Nano Lett 6(9) (2006) 2086-90.

[74] L.I. Moura, A.M. Dias, E.C. Leal, L. Carvalho, H.C. de Sousa, E. Carvalho, Chitosan-based dressings loaded with neurotensin--an efficient strategy to improve early diabetic wound healing, Acta Biomater 10(2) (2014) 843-57.

[75] H.S. Kim, H.S. Yoo, In vitro and in vivo epidermal growth factor gene therapy for diabetic ulcers with electrospun fibrous meshes, Acta Biomater 9(7) (2013) 7371-80.

[76] K. Bloch, A. Vanichkin, L.G. Damshkaln, V.I. Lozinsky, P. Vardi, Vascularization of wide pore agarose-gelatin cryogel scaffolds implanted subcutaneously in diabetic and non-diabetic mice, Acta Biomater 6(3) (2010) 1200-5.

[77] P. Chiodelli, S. Mitola, C. Ravelli, P. Oreste, M. Rusnati, M. Presta, Heparan sulfate proteoglycans mediate the angiogenic activity of the vascular endothelial growth factor receptor-2 agonist gremlin, Arterioscler Thromb Vasc Biol 31(12) (2011) e116-27.

[78] T. Miralem, R. Steinberg, D. Price, H. Avraham, VEGF(165) requires extracellular matrix components to induce mitogenic effects and migratory response in breast cancer cells, Oncogene 20(39) (2001) 5511-24.

[79] R. Mammadov, B. Mammadov, S. Toksoz, B. Aydin, R. Yagci, A.B. Tekinay, M.O. Guler, Heparin mimetic peptide nanofibers promote angiogenesis, Biomacromolecules 12(10) (2011) 3508-19.

[80] R. Mammadov, B. Mammadov, M.O. Guler, A.B. Tekinay, Growth factor binding on heparin mimetic peptide nanofibers, Biomacromolecules 13(10) (2012) 3311-9.

[81] B. Mammadov, R. Mammadov, M.O. Guler, A.B. Tekinay, Cooperative effect of heparan sulfate and laminin mimetic peptide nanofibers on the promotion of neurite outgrowth, Acta Biomater 8(6) (2012) 2077-86.

[82] V. Falanga, Wound healing and its impairment in the diabetic foot, Lancet 366(9498) (2005) 1736-43.

[83] S.K. Brancato, J.E. Albina, Wound macrophages as key regulators of repair: origin, phenotype, and function, Am J Pathol 178(1) (2011) 19-25.

[84] S.A. Eming, T. Krieg, J.M. Davidson, Inflammation in wound repair: molecular and cellular mechanisms, J Invest Dermatol 127(3) (2007) 514-25.

[85] R. Mirza, L.A. DiPietro, T.J. Koh, Selective and specific macrophage ablation is detrimental to wound healing in mice, Am J Pathol 175(6) (2009) 2454-62.

[86] I. Goren, N. Allmann, N. Yogev, C. Schürmann, A. Linke, M. Holdener, A. Waisman, J. Pfeilschifter, S. Frank, A transgenic mouse model of inducible macrophage depletion: effects of diphtheria toxin-driven lysozyme M-specific cell lineage ablation on wound inflammatory, angiogenic, and contractive processes, Am J Pathol 175(1) (2009) 132-47.

[87] M.L. Usui, J.N. Mansbridge, W.G. Carter, M. Fujita, J.E. Olerud, Keratinocyte migration, proliferation, and differentiation in chronic ulcers from patients with diabetes and normal wounds, J Histochem Cytochem 56(7) (2008) 687-96.

[88] S.N. Menon, J.A. Flegg, S.W. McCue, R.C. Schugart, R.A. Dawson, D.L. McElwain, Modelling the interaction of keratinocytes and fibroblasts during normal and abnormal wound healing processes, Proc Biol Sci 279(1741) (2012) 3329-38.

[89] F. Xu, C. Zhang, D.T. Graves, Abnormal cell responses and role of TNF-α in impaired diabetic wound healing, Biomed Res Int 2013 (2013) 754802.

[90] B. Hinz, Formation and function of the myofibroblast during tissue repair, J Invest Dermatol 127(3) (2007) 526-37.

[91] A. Shukla, M.P. Dubey, R. Srivastava, B.S. Srivastava, Differential expression of proteins during healing of cutaneous wounds in experimental normal and chronic models, Biochem Biophys Res Commun 244(2) (1998) 434-9.

[92] Y. Anis, O. Leshem, H. Reuveni, I. Wexler, R. Ben Sasson, B. Yahalom, M. Laster, I. Raz, S. Ben Sasson, E. Shafrir, E. Ziv, Antidiabetic effect of novel modulating peptides of G-protein-coupled kinase in experimental models of diabetes, Diabetologia 47(7) (2004) 1232-44.

[93] Y.W. Wang, G.D. Sun, J. Sun, S.J. Liu, J. Wang, X.H. Xu, L.N. Miao, Spontaneous type 2 diabetic rodent models, J Diabetes Res 2013 (2013) 401723.

[94] Y.S. Kim, E. Sohn, D.H. Jung, Y.M. Lee, C.S. Kim, J. Kim, J.S. Kim, Expression of heat shock protein 90 in the kidneys of diabetic db/db mice, Eur Rev Med Pharmacol Sci 18(15) (2014) 2198-204.

[95] M.L. Henry, L.B. Davidson, J.E. Wilson, B.K. McKenna, S.A. Scott, P.F. McDonagh, L.S. Ritter, Whole blood aggregation and coagulation in db/db and ob/ob mouse models of type 2 diabetes, Blood Coagul Fibrinolysis 19(2) (2008) 124-34.

[96] R. Mori, T. Kondo, T. Nishie, T. Ohshima, M. Asano, Impairment of skin wound healing in beta-1,4-galactosyltransferase-deficient mice with reduced leukocyte recruitment, Am J Pathol 164(4) (2004) 1303-14.

[97] Maryna S. Shkumat, Pavlo P. Klymenko, Yuri I. Leonov, Iryna N. Pishel, P. V.Glukhovskiy, Prolonged inflammatory cytokine expression during the late phase of wound healing in the

diabetic K14/mIGF1 transgenic mice., Journal of Medical and Biological Sciences 6(1) (2013).

[98] M.M. McFarland-Mancini, H.M. Funk, A.M. Paluch, M. Zhou, P.V. Giridhar, C.A. Mercer, S.C. Kozma, A.F. Drew, Differences in wound healing in mice with deficiency of IL-6 versus IL-6 receptor, J Immunol 184(12) (2010) 7219-28.

[99] S. Guo, L.A. Dipietro, Factors affecting wound healing, J Dent Res 89(3) (2010) 219-29.

[100] R.E. Mirza, M.M. Fang, W.J. Ennis, T.J. Koh, Blocking interleukin-1β induces a healing-associated wound macrophage phenotype and improves healing in type 2 diabetes, Diabetes 62(7) (2013) 2579-87.

[101] E.P. Ivanova, J. Hasan, H.K. Webb, G. Gervinskas, S. Juodkazis, V.K. Truong, A.H. Wu, R.N. Lamb, V.A. Baulin, G.S. Watson, J.A. Watson, D.E. Mainwaring, R.J. Crawford, Bactericidal activity of black silicon, Nat Commun 4 (2013) 2838.

[102] R. Kriparamanan, P. Aswath, A. Zhou, L. Tang, K.T. Nguyen, Nanotopography: cellular responses to nanostructured materials, J Nanosci Nanotechnol 6(7) (2006) 1905-19.

[103] A.J. Ridley, M.A. Schwartz, K. Burridge, R.A. Firtel, M.H. Ginsberg, G. Borisy, J.T. Parsons, A.R. Horwitz, Cell migration: integrating signals from front to back, Science 302(5651) (2003) 1704-9.

[104] P. Vaupel, F. Kallinowski, P. Okunieff, Blood flow, oxygen and nutrient supply, and metabolic microenvironment of human tumors: a review, Cancer Res 49(23) (1989) 6449-65.

[105] J.M. Llovet, S. Ricci, V. Mazzaferro, P. Hilgard, E. Gane, J.F. Blanc, A.C. de Oliveira, A. Santoro, J.L. Raoul, A. Forner, M. Schwartz, C. Porta, S. Zeuzem, L. Bolondi, T.F. Greten, P.R. Galle, J.F. Seitz, I. Borbath, D. Häussinger, T. Giannaris, M. Shan, M. Moscovici, D. Voliotis, J. Bruix, S.I.S. Group, Sorafenib in advanced hepatocellular carcinoma, N Engl J Med 359(4) (2008) 378-90.

[106] U. Covani, S. Marconcini, R. Crespi, A. Barone, Bacterial plaque colonization around dental implant surfaces, Implant Dent 15(3) (2006) 298-304.

[107] H. Wu, C. Moser, H.Z. Wang, N. Høiby, Z.J. Song, Strategies for combating bacterial biofilm infections, Int J Oral Sci 7(1) (2015) 1-7.

[108] S. Lavenus, M. Berreur, V. Trichet, P. Pilet, G. Louarn, P. Layrolle, Adhesion and osteogenic differentiation of human mesenchymal stem cells on titanium nanopores, Eur Cell Mater 22 (2011) 84-96; discussion 96.

[109] B.D. Boyan, A. Cheng, R. Olivares-Navarrete, Z. Schwartz, Implant Surface Design Regulates Mesenchymal Stem Cell Differentiation and Maturation, Adv Dent Res 28(1) (2016) 10-7.

[110] J.M. Łopacińska, C. Grădinaru, R. Wierzbicki, C. Købler, M.S. Schmidt, M.T. Madsen, M. Skolimowski, M. Dufva, H. Flyvbjerg, K. Mølhave, Cell motility, morphology, viability and proliferation in response to nanotopography on silicon black, Nanoscale 4(12) (2012) 3739-45.